

**PROMPT ELECTRON PRODUCTION IN  
ELECTRON-POSITRON ANNIHILATIONS AT 29 GEV**

Thesis by

**Dale E. Koop**

In Partial Fulfillment of the Requirements

for the Degree of

Doctor of Philosophy

**California Institute of Technology**

Pasadena, California

1984

(Submitted May 18, 1984)

## ACKNOWLEDGMENT

This thesis was possible because of the successful construction and operation of DELCO by members from Caltech, Stanford and SLAC. For their important contributions to various parts of the experimental program I would like to thank all members of the DELCO group: W. B. Atwood, P. H. Baillon, B. C. Barish, G. Bonneaud, H. DeStaebler, G. J. Donaldson, R. Dubois, M. M. Duro, E. E. Elsen, S. G. Gao, Y. Z. Huang, G. M. Irwin, R. P. Johnson, H. Kichimi, J. Kirkby, D. E. Klem, J. Ludwig, G. B. Mills, A. Ogawa, T. Pal, D. Perret-Gallix, R. Pitthan, D. L. Pollard, C. Y. Prescott, L. Z. Rivkin, L. S. Rochester, W. Ruckstuhl, M. Sakuda, S. S. Sherman, E. J. Siskind, R. Stroynowski, S. Q. Wang, S. G. Wojcicki, H. Yamamoto, W. G. Yan, and C. C. Young; and for invaluable technical contributions I would like to thank: A. Baumgarten, G. B. Bowden, B. M. Bricaud, D. R. Chambers, R. Cooper, R. Dekker, J. Hanson, A. E. Johnston, J. McDonald, D. A. Ouimette, D. I. Porat, C. L. Rasmussen, O. H. N. Saxton, D. Sell, S. J. Sund, and J. Zingheim. In addition I would like to acknowledge the invaluable services of the Experimental Facilities Division, PEP Operations Group and Stanford Linear Accelerator Center.

I would also like to acknowledge Makoto Sakuda, George Irwin, Jasper Kirkby, and Ryszard Stroynowski for their contributions to the success of this analysis. In particular, I am especially grateful to my advisor Professor Barry C. Barish for providing me with the opportunity and advice I needed to complete this work.

Finally, I would like to thank all the members of my family and my friends for their support.

## ABSTRACT

We have studied the production of prompt electrons in high statistics sample ( $118 \text{ pb}^{-1}$ ) of multihadron events produced in electron positron annihilations at 29 Gev. The experiment was performed using the DELCO facility on the PEP storage ring at SLAC. Electron identification was done primarily with a large acceptance threshold Čerenkov counter. Both the momentum and the transverse momentum spectra are measured in terms of a differential cross section for electrons having momenta in the range  $0.5 < P < 5.5 \text{ Gev}/c$ . We measure the inclusive cross section in this momentum range to be  $35.8 \pm 3.1 \text{ pb}$ . The final distribution of candidates in the  $P - P_{\perp}$  plane are fit well using a Monte Carlo having a combination of bottom and charm quark decays with the semielectronic branching ratios of  $(15.0 \pm 2.9)\%$  and  $(8.9 \pm 1.4)\%$ . We observe no evidence of electron production from new sources and determine a cross section upper limit of  $11.6 \text{ pb}$  (90% CL) for this process. We find that the fragmentation functions are hard for both  $b$  and  $c$  quarks, characterized by the values  $\langle z_b \rangle = 0.77 \pm 0.05$  and  $\langle z_c \rangle = 0.68 \pm 0.06$ , where  $z$  is the fraction of the heavy quark's energy that is retained by the primary hadron containing the heavy quark. The fragmentation function is fit well by the form  $D_q(z) = N/[z(1 - \frac{1}{z} - \frac{\epsilon_q}{1-z})^2]$  with  $\epsilon_b = .018_{-.011}^{+.024}$  and  $\epsilon_c = .053_{-.029}^{+.061}$ . Finally, we observe events having two electrons with an inclusive cross section of  $2.8 \pm 1.3 \text{ pb}$  for this process, which is consistent with the rate expected from the measured semielectronic rates.

CONTENTS

<b>Chapter 1</b>	Introduction . . . . .	1
1.1	Prompt Electron Studies . . . . .	1
1.2	Prompt Electron Analysis in DELCO . . . . .	4
<b>Chapter 2</b>	Prompt Electron Physics . . . . .	7
2.1	Heavy Quark Production in $e^+e^-$ Annihilation . . . . .	7
2.2	The Fragmentation of Heavy Quarks . . . . .	11
2.3	Semileptonic Decays of Heavy Hadrons . . . . .	15
<b>Chapter 3</b>	Apparatus . . . . .	26
3.1	The DELCO Detector . . . . .	26
3.2	Drift Chamber Tracking System and Magnet . . . . .	28
3.3	Electromagnetic Shower Counter Systems . . . . .	34
3.4	Čerenkov Counter . . . . .	41
3.5	Luminosity Monitors . . . . .	63
3.6	Data Acquisition System and Online Trigger . . . . .	67
3.7	Monte Carlo Simulation of Detector . . . . .	70
3.8	Monte Carlo Event Generation . . . . .	72
<b>Chapter 4</b>	Procedure . . . . .	79
4.1	Luminosity Measurements . . . . .	81
4.2	Multihadron Event Selection . . . . .	82
4.3	Electron Selection . . . . .	86
4.4	Prompt Electron Efficiency . . . . .	101
4.5	Background Normalization . . . . .	108

4.6	Data Reduction . . . . .	117
<b>Chapter 5</b>	<b>Analysis and Results . . . . .</b>	<b>121</b>
5.1	Prompt Electron Differential Cross Section . . . . .	122
5.2	Fitting the $P - P_t$ Spectrum . . . . .	123
5.3	Results of Fit . . . . .	133
5.4	Multi-Electron Events . . . . .	144
<b>Chapter 6</b>	<b>Summary and Conclusion . . . . .</b>	<b>149</b>
<b>Appendix A</b>	<b>. Electron Probability Tables . . . . .</b>	<b>154</b>
<b>References</b>	<b>. . . . .</b>	<b>161</b>

FIGURE CAPTIONS

2.1.	$e^+e^-$ annihilation into hadrons. . . . .	8
2.2.	Hadron cross section in $e^+e^-$ annihilations. . . . .	10
2.3.	Multihadron production in $e^+e^- \rightarrow \text{hadrons}$ . . . . .	12
2.4.	Spectator diagrams for $c$ and $b$ decay. . . . .	18
2.5.	FCNC decay of $b$ into $e^+e^-$ pairs. . . . .	20
2.6.	Non-spectator diagrams for $D^0$ , $D^+$ , $F^+$ , and $\Lambda_c^+$ decay. . . . .	22
2.7.	Gluons enhanced non-spectator diagrams. . . . .	24
3.1.	The DELCO detector . . . . .	27
3.2.	Drift chamber cell geometries. . . . .	31
3.3.	DELCO magnet field map. . . . .	35
3.4.	Momentum resolution of 14.5 Gev/c Bhabha electrons. . . . .	36
3.5.	Barrel shower counter pulse height response. . . . .	40
3.6.	Scatterplot of shower counter response vs. momentum. . . . .	42
3.7.	Čerenkov counter optics . . . . .	46
3.8.	Mirror reflectivity . . . . .	49
3.9.	Cross section of Čerenkov PMT assembly. . . . .	52
3.10.	PMT response with p-terphenyl wave shifter. . . . .	53
3.11.	Refractive index dispersion for gases . . . . .	56
3.12.	PMT base diagram . . . . .	58
3.13.	$N_0$ distribution of Čerenkov counter . . . . .	60
3.14.	Raw photoelectron yield for isobutane and nitrogen . . . . .	61
3.15.	Photoelectron yield vs. momentum. . . . .	62

3.16.	Čerenkov counter time distribution. . . . .	64
3.17.	Čerenkov counter pulse height timing slew. . . . .	65
3.18.	Čerenkov times in multihadron events. . . . .	66
3.19.	Data acquisition system block diagram. . . . .	68
3.20.	Monte Carlo $e$ spectrum at $\psi$ and $\Upsilon$ . . . . .	75
3.21.	Monte Carlo distributions. . . . .	76
4.1.	Total energy of charged tracks in multihadron events. . . . .	84
4.2.	Čerenkov pion thresholds in isobutane and nitrogen . . . . .	91
4.3.	Multihadron event with asymmetric gamma conversion. . . . .	94
4.4.	Čerenkov noise rate vs. $\cos\theta$ of PDC stubs. . . . .	96
4.5.	Low-level Čerenkov pulse heights . . . . .	99
4.6.	Čerenkov vs. shower counter response for multihadrons. . . . .	100
4.7.	Event with track-flipping. . . . .	111
4.8.	Pion background from track-flipping and Monte Carlo. . . . .	113
4.9.	Momenta of gamma electrons in MC and data . . . . .	116
4.10.	One-event display of a prompt electron candidate . . . . .	119
5.1.	Momentum spectrum of candidates including background. . . . .	124
5.2.	Prompt electron differential cross section vs $P$ . . . . .	125
5.3.	Fragmentation Function for $b$ and $c$ Mesons. . . . .	137
5.4.	Fit to Electron Differential Cross Section vs $P$ . . . . .	140
5.5.	Fit to Electron Differential Cross Section vs $P_{\perp}$ . . . . .	141
5.6.	Dielectron event. . . . .	145

TABLES

2.1.	Quark Masses. . . . .	7
2.2.	Heavy Meson Decay Fractions. . . . .	16
2.3.	Kobayashi-Maskawa Matrix Elements. . . . .	19
2.4.	Lifetimes and Semielectronic Rates for Charmed Hadrons. . . . .	21
3.1.	Summary of Acceptance and Performance of the DELCO Detector. . . . .	29
3.2.	Drift Chamber Characteristics. . . . .	33
3.3.	Material in DELCO, $\chi/\chi_0$ . . . . .	38
3.4.	Properties of Čerenkov Radiators. . . . .	55
3.5.	Particle Thresholds, (Gev/c), in Čerenkov Radiators. . . . .	55
3.6.	Radiative Corrections to $q\bar{q}$ Cross Sections. . . . .	77
4.1.	Particle Rates in Monte Carlo Multihadron Events. . . . .	80
4.2.	Charged Particle Rates in DELCO. . . . .	80
4.3.	Luminosity Measurements. . . . .	82
4.4.	Efficiency of Multihadron Selection Criteria. . . . .	85
4.5.	Integrated Luminosity and Event Rates for Data Sets. . . . .	86
4.6.	Number of Tracks per Čerenkov Cell in Multihadron Events . . . . .	89
4.7.	Track Cluster Distribution in Multihadron Events. . . . .	89
4.8.	Results of Gamma Electron Finding Algorithm. . . . .	92
4.9.	Efficiencies of all Kinematic and Topological Cuts. . . . .	103
4.10.	Efficiency for Kinematic Cuts in Isobutane for MC and Data. . . . .	103
4.11.	Efficiency for Kinematic Cuts in Nitrogen for MC and Data. . . . .	104
4.12.	Efficiency Correction Factors for Kinematic Cuts in MC. . . . .	105
4.13.	Scanning Efficiency from Monte Carlo. . . . .	107

4.14.	Final Efficiencies for Prompt Electrons. . . . .	107
4.15.	Nonelectron Background Rates per Event. . . . .	109
4.16.	Pion Background Rate From Track Flipping. . . . .	114
4.17.	$P - P_{\perp}$ Distribution of Hadron Background. . . . .	114
4.18.	$P - P_{\perp}$ Distribution of Gamma Electron Background . . . . .	115
4.19.	Data Reduction Rates. . . . .	118
5.1.	$P - P_{\perp}$ Distribution of Prompt Electron Candidates. . . . .	122
5.2.	Measured Total Prompt Electron Cross Section. . . . .	126
5.3.	Radiative Corrections to Fragmentation Functions. . . . .	128
5.4.	Sources of Systematic Errors. . . . .	133
5.5.	Results of Fits to the $P - P_{\perp}$ Distribution of Electrons. . . . .	134
5.6.	Correlation Coefficients for Fit Parameters. . . . .	135
5.7.	Low Energy Semileptonic Rates, (%). . . . .	136
5.8.	Fragmentation Functions and Semileptonic Branching Ratios. . . . .	138
5.9.	Charm Fragmentation From $D^*$ Experiments. . . . .	139
5.10.	Cross Section of Prompt Electron Contributions, (pb). . . . .	142
5.11.	Relative Contributions to Electron Signal. . . . .	142
5.12.	Dielectron Event Rates. . . . .	146
5.13.	Dielectron Charge Correlations. . . . .	146
5.14.	Fit Contributions to Electron Signal. . . . .	148

## CHAPTER 1

# Introduction

### § 1.1 PROMPT ELECTRON STUDIES

Electrons that are produced directly in high energy interactions from the decays of new heavy particles are considered to be prompt electrons. During the last ten years experiments that provided information on these electrons have played a major role both in discovering new states of matter and in understanding their properties. Two families of quark-antiquark bound states, a new sequential lepton, and the weak vector bosons were found with prompt lepton searches in high energy reactions.

In 1974, the  $J/\psi$  resonance was first seen as a peak near 3.1 Gev in the reconstructed  $e^+e^-$ -mass spectrum of a dielectron experiment<sup>1</sup> studying the reaction

$$p + Be \rightarrow e^+ + e^- + X \quad .$$

Concurrently, a sharp peak was observed<sup>2</sup> at 3.1 Gev in the  $e^+e^-$  annihilation cross section for the reactions

$$e^+e^- \rightarrow \text{hadrons}, \quad e^+e^-, \quad \mu^+\mu^- \quad .$$

The  $J/\psi$  was interpreted as the lowest  $c\bar{c}$  bound state, and indicated the discovery of *charm*. Subsequent experiments at energies near the  $\psi''(3770)$  resonance and higher led to the observation of anomalous prompt electron production<sup>3</sup> in the reaction

$$e^+e^- \rightarrow e^\pm + X \quad ,$$

along with the observation<sup>4</sup> of new hadronic decay states from at least one new quantum state, which was inhibited from decaying electromagnetically or strongly. One of the states was the charmed  $D$  meson which decayed weakly following the Glashow-Illiopoulos-Maiani (GIM) model.<sup>5</sup> Earlier observations<sup>6</sup> of anomalous  $e\mu$  production in the reaction

$$e^+e^- \rightarrow e^\pm + \mu^\mp + \text{missing energy}$$

at the same energy range led to the discovery of the  $\tau$  lepton as the other new quantum state.

In 1977 the  $\Upsilon$  was discovered<sup>7</sup> as a resonance at 9.5 Gev in the invariant mass spectrum of prompt dimuons produced in the reaction

$$p + (Cu, Pt) \rightarrow \mu^+ + \mu^- + X \quad .$$

The  $\Upsilon$  was interpreted as the lowest  $b\bar{b}$  bound state, and indicated the existence of *bottom* and another generation of quark flavors. The  $b$  quark fits nicely into a six-quark model<sup>8</sup> which preserves the symmetry between quarks and leptons, including the  $\tau$  lepton, and suppresses flavor changing neutral currents as in the GIM model.

Several narrow resonances were then seen in  $e^+e^-$  annihilations<sup>9</sup> between 9.4 and 10.3 Gev. A fourth resonance, the  $\Upsilon(4s)$ , was seen<sup>10</sup> with a width that was visibly broader than the first three resonances, suggesting it was above the production threshold for weakly decaying  $B$  mesons. Proof that  $B$  mesons were being produced finally came from the observation of the enhanced production of prompt electrons,<sup>11-12</sup> which are produced in the weak decays of  $b$  quarks.

Following the discovery of a third-generation sequential lepton and a fifth quark, major emphasis at the PEP and PETRA storage rings was placed on searching for the partner of the  $b$ . Measurements have since pushed the threshold for the production of a possible  $t\bar{t}$  pair above 45 Gev and out of range of PEP or PETRA.

Recent results at CERN<sup>13</sup> during the past year further demonstrate the importance of prompt lepton searches. The observation of energetic prompt electrons produced in  $p\bar{p}$  collisions at 540 Gev has led to the discovery of the  $Z^0$  and  $W^\pm$  vector bosons.

Apart from discovering new states of matter, prompt lepton searches have been used to measure important characteristics of known particles. In the low energy region, prompt lepton counting experiments<sup>14-16</sup> have measured  $D$  meson semileptonic rates and decay spectra which differ from the expectations of simple spectator models, and suggest different lifetimes<sup>17-18</sup> for  $D^\pm$  and  $D^0$  mesons. In these models, the heavy quark decays with the light quark acting as a spectator having little influence, resulting in similar decay rates and lifetimes for the  $D^\pm$  and  $D^0$ . The models have been modified to agree with experiment by accounting for non-spectator effects; however, these effects are expected to be weaker for decays of the more massive  $b$  quarks. Experiments at CESR, PEP, and PETRA are

presently studying the semileptonic decays of mesons containing  $b$  quarks, and are using the prompt leptons from  $B$  mesons to determine directly the  $b$  lifetime by measuring the impact parameter of the lepton trajectory with the event production vertex.<sup>19</sup> At PEP and PETRA, the selection of multihadron events containing prompt leptons is a useful and reliable method of enhancing  $c\bar{c}$  and  $b\bar{b}$  signals.

Prompt lepton experiments also provide information on the hadronization of quarks after their initial production. The momentum spectrum of leptons from  $c$  and  $b$  decays contains information on the fraction of energy the heavy quarks retain during fragmentation into hadrons. It has been suggested<sup>20</sup> that the inertia of the heavy quark is retained by the meson containing the heavy quark causing hard fragmentation functions. The only information on  $b$  quark fragmentation has come from prompt lepton experiments.

In this study we concentrate on measuring prompt electron production  $e^+e^-$  annihilations at 29 Gev and use the electron momentum spectrum to extract information on the fragmentation of heavy quarks. As a result of this study, we obtain the inclusive cross section for prompt electrons and set limits on the copious production of electrons from new sources. The production of electrons from anomalous sources at PEP or PETRA would indicate new particle production or exotic decay mechanisms. The absence of such anomalous electrons can be used to set upper limits on the probability of various new prompt lepton sources.

## § 1.2 PROMPT ELECTRON ANALYSIS IN DELCO

One feature that makes this experiment unique among those presently running at PEP and PETRA is the electron identification capability of the DELCO detec-

tor, which allows measurement of electrons over 90% of the allowed kinematic range. This is accomplished with a unique large-solid-angle gas-filled Čerenkov counter in conjunction with a low-mass central detector. Other experiments studying prompt lepton production are limited to the upper end of the kinematic range.

Prompt electrons from weak decays of heavy hadrons produced at 29 GeV in  $e^+e^-$  annihilations at PEP are measured. The electrons are detected using two different Čerenkov radiators, nitrogen and isobutane. The upper momentum limits for these radiators are determined by the onset of Čerenkov radiation from charged pions and the lower limits are determined by charged particle tracking efficiency. The ranges are 0.5 - 2.5 GeV/c for isobutane and 0.5 - 5.5 GeV/c for nitrogen. Other experiments at PEP and PETRA study the region above 2 GeV/c. The use of two gases makes the analysis equivalent to two experiments with different efficiencies and backgrounds and provides a useful cross check for the results.

Measurements of  $b$  and  $c$  fragmentation functions and semielectronic rates are done simultaneously on the final electron signal including backgrounds from non-prompt electrons and misidentified non-electrons. The spectrum of the electron momentum transverse to the hadron jet axis is determined by the mass of the decaying particle, and is used to separate electrons with  $b$ -parents from those with  $c$ -parents. The fragmentation of the  $c$  and  $b$  quarks is determined by studying the momentum spectra of the electrons as a function of the transverse momentum. A Monte Carlo electron signal is calculated in the  $P - P_{\perp}$  plane, and is fit to the signal measured in the data by adjusting the Monte Carlo fragmentation functions and semielectronic rates. Results are compared to other experiments, which use different techniques or are limited to different kinematic regions.

The final measurements are used to put limits on copious sources of prompt electrons by comparing the measured prompt electron cross section with the expected value obtained using semielectronic rates of previous experiments. Also, the first observation of dielectron events at PEP and PETRA is presented with a comparison of their expected rates based on the rates for single prompt electrons, of  $b$  and  $c$  flavored hadrons, measured in this experiment.

In the next chapter, we describe the present understanding of heavy quark production and fragmentation in  $e^+e^-$  annihilations and the models of heavy quark decay. Finally, we will describe prompt electron production in the reaction

$$e^+e^- \rightarrow \gamma \rightarrow q\bar{q} \quad ,$$

and discuss the measurements to be made in this study. A description of the DELCO detector is given in Chapter 3, with emphasis on the Čerenkov counter, along with a description of the Monte Carlo generator and simulation programs. Chapter 4 is a description of the procedure used to select prompt electron candidates and determine the background rates and efficiencies. The analysis and results obtained from the electron signal are given in Chapter 5 and, finally, a summary and conclusion are given in Chapter 6.

CHAPTER 2

# Prompt Electron Physics

## § 2.1 HEAVY QUARK PRODUCTION IN $e^+e^-$ ANNIHILATION

Table 2.1 Quark Masses.

Quark	Mass, (Gev/c <sup>2</sup> )	Charge
u <i>up</i>	0.3	+2/3
d <i>down</i>	0.3	-1/3
s <i>strange</i>	0.5	-1/3
c <i>charm</i>	1.7	+2/3
b <i>bottom</i>	5.0	-1/3
t <i>top</i>	>22.5	+2/3

Hadrons are produced in the annihilation of  $e^+$  and  $e^-$  into  $q\bar{q}$  states via single virtual photons and through the exchange of two virtual photons. These processes are shown in figure 2.1 . The differential cross section for producing point-like spin- $\frac{1}{2}$  particles via a single photon is given from QED as

$$\frac{d\sigma}{d\Omega} = \frac{\alpha^2 \beta q^2}{4s} (2 - \beta^2 + \beta^2 \cos^2 \theta) \tag{2.1}$$

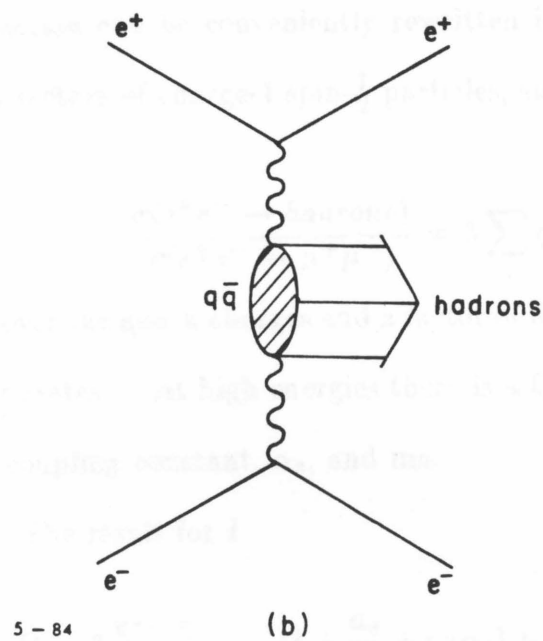
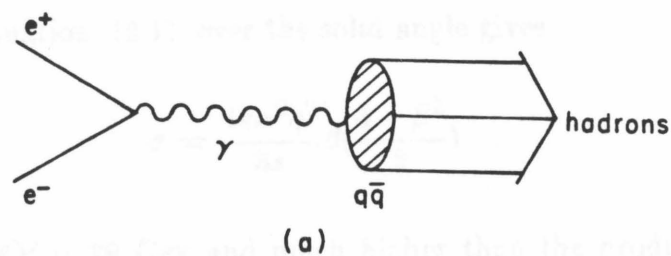


Fig. 2.1  $e^+e^-$  annihilation into hadrons. (a) Single photon annihilation. (b) Two photon exchange.

5 - 84

(b)

4769A4

where  $\alpha$  is the fine structure constant,  $1/137$ ,  $\beta$  is the velocity of the quark,  $q$  is the particle charge, and  $s$  is the square of the annihilation energy. Measurements of the hadronic cross section at PEP and PETRA are consistent with the quarks listed in table 2.1 including an unobserved  $t$  quark of mass  $> 22.5 \text{ Gev}/c^2$ .

Integrating equation (2.1) over the solid angle gives

$$\sigma = \frac{4\pi\alpha^2 q^2}{3s} \beta \left( \frac{3 - \beta^2}{2} \right) .$$

The energy at PEP is 29 Gev and much higher than the production threshold for the first 5 quarks listed in table 2.1, so we make the approximation of  $\beta = 1$ . The  $q\bar{q}$  cross section can be conveniently rewritten in terms of the point-like annihilation cross section of charge-1 spin- $\frac{1}{2}$  particles, such as the  $e^+e^- \rightarrow \mu^+\mu^-$ , as

$$R = \frac{\sigma(e^+e^- \rightarrow \text{hadrons})}{\sigma(e^+e^- \rightarrow \mu^+\mu^-)} = 3 \sum_i q_i^2 ,$$

where the sum is over the quark charges and a factor of 3 is included to account for the different color states. At high energies there is a QCD correction characterized by a strong coupling constant,  $\alpha_s$ , and manifested by gluon bremsstrahlung in the final state. The result for  $R$  is

$$R = 3 \sum_i q_i^2 \cdot \left( 1 + \frac{\alpha_s}{\pi} + Q(\alpha_s) + \dots \right) .$$

The QCD corrections increase  $R$  by approximately 5% at PEP.

Figure 2.2 shows  $R$  plotted over the explored energy range<sup>21</sup>. There are noticeable steps at the thresholds for  $c\bar{c}$  ( $J/\psi$ ) and  $b\bar{b}$  ( $\Upsilon$ ) production, and the plot is inconsistent with  $t\bar{t}$  production below 45 Gev. The heavy quark pairs ( $c\bar{c}$  and  $b\bar{b}$ ) contribute 4/11 to the calculated value for  $R$ .

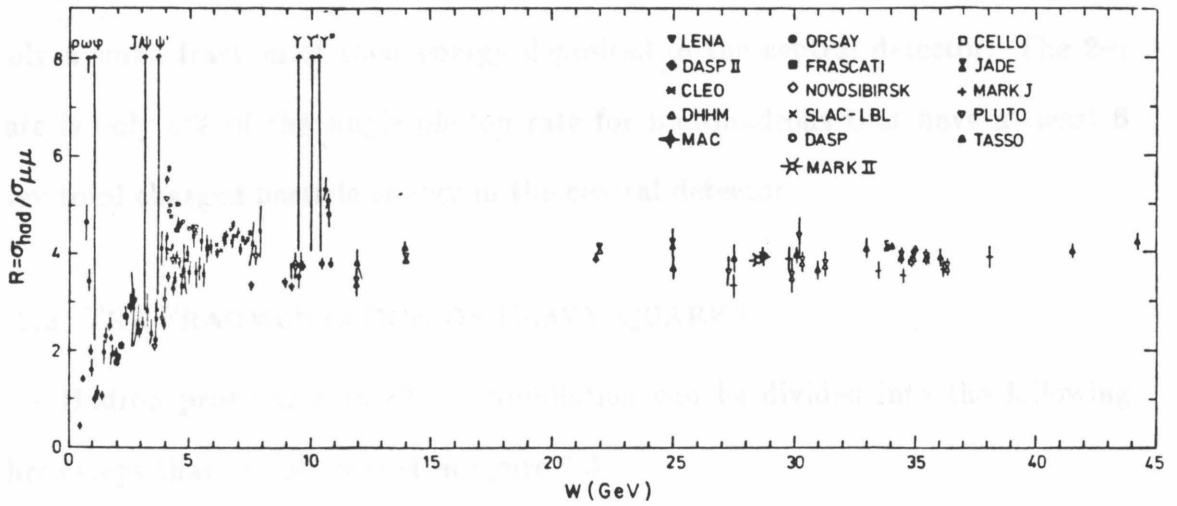


Fig. 2.2 Hadron cross section in  $e^+e^-$  annihilations. Ratio  $R$  of the multi-hadron cross section to the  $\mu$  pair cross section.

Equation (2.1) shows that  $q\bar{q}$  pairs are produced with an angular distribution of

$$\frac{d\sigma}{d\Omega} \sim 1 + \cos^2 \theta \quad ,$$

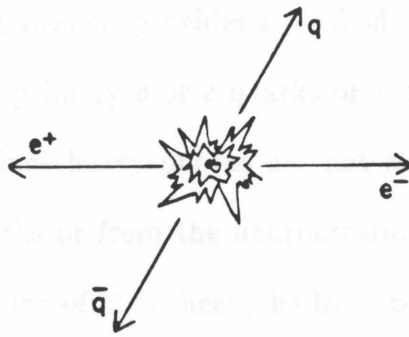
so many of the events are contained in the central region of the solid angle covered by detectors like DELCO. Events produced in the two photon exchange ( $2\text{-}\gamma$  events) are typically at small angles with respect to the annihilation electrons and have only a small fraction of their energy deposited in the central detector. The  $2\text{-}\gamma$  rate is only 5% of the single photon rate for multihadrons that have at least 6 Gev total charged particle energy in the central detector.

## § 2.2 THE FRAGMENTATION OF HEAVY QUARKS

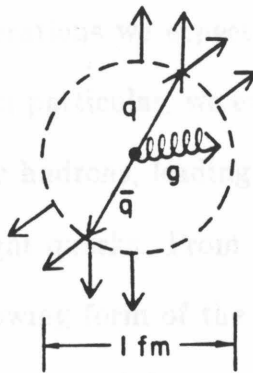
Hadron production in  $e^+e^-$  annihilation can be divided into the following three steps that are illustrated in figure 2.3

1. The  $q\bar{q}$  pairs are produced, sometimes accompanied by a gluon bremsstrahlung, but are not observed as free particles at distances greater than about 1 fm.
2. Primary hadrons are formed out of the primary quarks and secondary  $q\bar{q}$  pairs that are pulled out of the vacuum. The primary hadrons,  $H$ , have a fraction,  $z$ , of the primary quark energy, determined by a fragmentation function  $D_q^H(z)$ .
3. The primary hadrons decay via intermediate resonances and weak interactions to final state particles.

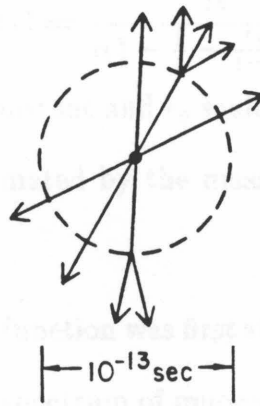
The distinction between the first and second steps is arbitrary and model-dependent<sup>22</sup>. At present, the fragmentation function can not be reliably calculated using QCD. Instead, it is constructed from kinematical considerations.



(a)



(b)



(c)

5 - 84

4769A6

Fig. 2.3 Multihadron production in  $e^+e^- \rightarrow \text{hadrons}$ . (a)  $e^+e^-$  annihilation into a  $q\bar{q}$  pair. (b) Fragmentation of  $q\bar{q}$  pair into primary hadrons. (c) Decay into final state particles.

Any information on the fragmentation of the initial quark pairs is useful, and the production of heavy mesons provides a method of achieving this information. Heavy hadrons contain primary  $b$  or  $c$  quarks or  $c$  quarks from the weak decays of primary  $b$  quarks, since heavy quarks are not expected to be produced from the decays of light quarks or from the hadronization of the vacuum. Measuring the fragmentation function of these heavy hadrons provides information on quark fragmentation.

From kinematical considerations we expect heavy quarks to fragment differently than lighter quarks.<sup>20</sup> In particular, we expect them to retain most of their inertia when they form heavy hadrons, leading to stiffer fragmentation functions for heavy quarks than for light quarks. From kinematic arguments, Peterson et al.<sup>23</sup> have suggested the following form of the fragmentation function for heavy quarks

$$D_q(z) = \frac{N}{z(1 - \frac{1}{z} - \frac{\epsilon_q}{1-z})^2}, \quad (2.2)$$

where  $N$  is a normalization constant and  $\epsilon_q$  scales inversely with the square of the quark mass, which is approximated by the mass of the hadron containing quark  $q$ .

The charm fragmentation function was first studied by the CDHS collaboration<sup>24</sup> by measuring the momentum spectrum of muons from charm decay. They studied dimuon events in high energy neutrino interactions. These events were presumed to originate from the reaction

$$\nu_\mu + Fe \rightarrow \mu^- + X + (c \rightarrow X + \mu^+) .$$

They do not measure the detailed structure of the fragmentation function since

charmed hadrons are not reconstructed, but by unfolding the muon spectrum they are able to arrive at a function with an average  $z$  of  $\langle z_c \rangle = .69 \pm .05$ . In another experiment<sup>25</sup>,  $D$  mesons originating from neutrino interactions in an emulsion were fully reconstructed using a downstream spectrometer. The results indicate a stiff function with  $\langle z \rangle \approx .59$ .

In  $e^+e^-$  experiments<sup>26-30</sup>  $D$  mesons have been reconstructed from decays of  $D^*$  mesons produced in the reaction

$$e^+e^- \rightarrow \bar{D}^* + (D^* \rightarrow D\pi \rightarrow K\pi, K\pi\pi\pi) .$$

Results of these experiments show fragmentation functions with  $\langle z \rangle \approx 0.6$ . They use  $z$  as the fraction of beam energy and are sensitive to initial state radiation, which should lower  $\langle z \rangle$  by about 2-4 %.

This experiment is the first to measure the charm fragmentation by unfolding the momentum spectrum of prompt leptons from the decays of charmed mesons produced in  $e^+e^-$  annihilations.<sup>31</sup> The fragmentation is averaged over all charmed hadrons produced in the reaction

$$e^+e^- \rightarrow c\bar{c} \rightarrow e^\pm + X .$$

The electrons from  $c$  decays are statistically separated from the electrons of  $b$  decays in the analysis described in this thesis.

The fragmentation function of the  $b$  quark has been measured only in experiments at PEP<sup>31,32-33</sup> and PETRA<sup>34-36</sup> by studying the spectra of prompt leptons produced in  $e^+e^-$  annihilations. The leptons of  $c$  decays are statistically separated

from those of  $b$  decays by using the transverse momentum spectrum. The mean transverse momentum of decay products depends on the mass of their parents, so leptons from  $b$  quarks typically have larger transverse momentum than those from  $c$  quarks. Due to limited kinematical acceptance, these experiments must use the fragmentation form for the  $c$  quarks obtained in the  $D^*$  reconstruction experiments and then determine the  $b$  quark function from the lepton data. The experiment reported here is the first to measure simultaneously the charm and bottom fragmentation functions by analyzing prompt leptons. The results give a hard  $c$  fragmentation function and an even harder  $b$  fragmentation function.

### § 2.3 SEMILEPTONIC DECAYS OF HEAVY HADRONS

For this thesis we will use the standard model for weak decays of heavy mesons. In this model there are three generations of left-handed leptons and quarks in SU(2) doublets, listed as

$$\begin{pmatrix} \bar{\nu}_e \\ e^- \end{pmatrix} \quad \begin{pmatrix} \bar{\nu}_\mu \\ \mu^- \end{pmatrix} \quad \begin{pmatrix} \bar{\nu}_\tau \\ \tau^- \end{pmatrix} \quad \begin{pmatrix} u \\ d' \end{pmatrix} \quad \begin{pmatrix} c \\ s' \end{pmatrix} \quad \begin{pmatrix} t \\ b' \end{pmatrix} .$$

Coupling within each doublet is mediated by charged weak vector (W) bosons. The coupling strength is universal for all generations of leptons and quarks. In the absence of mass there are no transitions between generations; neutrinos only couple to their charged lepton partner. For quarks, the mechanism which causes mass generation also causes the quark eigenstates and the weak eigenstates to be different, allowing mixing between the quark generations for weak transitions. The

mixing between quark states can be written as

$$\begin{pmatrix} d \\ s \\ b \end{pmatrix} = U \begin{pmatrix} d' \\ s' \\ b' \end{pmatrix} .$$

$U$  is the KM mass mixing matrix

$$\begin{pmatrix} c_\beta c_\theta & c_\beta s_\theta & s_\beta \\ -c_\gamma s_\theta - s_\gamma s_\beta c_\theta e^{i\delta} & c_\gamma c_\theta - s_\gamma s_\beta s_\gamma e^{i\delta} & s_\gamma c_\beta e^{i\delta} \\ -c_\gamma s_\beta c_\theta + s_\gamma s_\theta e^{i\delta} & -c_\gamma s_\beta s_\gamma - s_\gamma c_\theta e^{-i\delta} & c_\gamma c_\beta \end{pmatrix} ,$$

where  $c_\theta = \cos \theta$ ,  $s_\theta = \sin \theta$ ,  $\theta$  is the normal Cabibbo angle, and  $\delta$  is a CP violating phase.

**Table 2.2 Heavy Meson Decay Fractions.**

Final State	$b \rightarrow cW$	$c \rightarrow eW$
$W \rightarrow q \ e\nu$	.144	.2
$q \ \mu\nu$	.144	.2
$q \ \pi$	.033	-
$q \ ud$	.507	.6
$q \ cs$	.167	-

The charged weak currents for quarks are written

$$J^\mu = (\bar{u} \ \bar{c} \ \bar{t}) \gamma^\mu (1 - \gamma^5) U \begin{pmatrix} d' \\ s' \\ b' \end{pmatrix} .$$

The  $c$  quark is heavier than its partner the  $s$  quark and can decay to either the  $s$  or  $d$ . The  $b$  and  $s$  quarks are lighter than their partners and can only decay

diagonally via quark mixing to the corresponding partner in a lighter generation.

The allowed decays are shown in figure 2.4 for  $c$  and  $b$  flavored mesons, with the light antiquark acting only as a spectator. The final decay fractions are listed in table 2.2 for these decays, taking into account the final states including color factors and phase space.

Mixing between generations is small so the most sensitive method of measuring the mixings angles is with  $s$  and  $b$  decays. The  $b$  quark decays via  $\sin \gamma \cos \beta e^{i\delta}$  to  $c$  and via  $\sin \beta$  to  $u$  so that the recent results from CESR, <sup>37-38</sup> which put limits on

$$\frac{\Gamma(b \rightarrow u)}{\Gamma(b \rightarrow c)} < 0.05 \quad (.90CL)$$

from the shape of the prompt electron spectrum in  $B$  meson decay, also put limits on the mixing angles  $\sin \gamma$  and  $\sin \beta$ .

The semielectronic decay of the  $c$  and  $b$  quarks can be calculated as in muon beta decay and is given for  $c$  by

$$\begin{aligned} \Gamma(c \rightarrow e\nu s) &= \frac{G^2 M_c^5}{192\pi^3} \cdot g \cdot \frac{M_s}{M_c} \cdot \left[ 1 + \frac{2\alpha_s}{3\pi} f(\lambda) \right] \cdot C \\ &= \frac{M_c^5}{M_\mu^5} \cdot g \cdot \left[ 1 + \frac{2\alpha_s}{3\pi} f(\lambda) \right] \cdot C \cdot \Gamma(\mu \rightarrow e\nu \bar{\nu}) \end{aligned} \quad (2.3)$$

and for  $b$  by

$$\begin{aligned} \Gamma(b \rightarrow e\nu c) &= \frac{G^2 M_b^5}{192\pi^3} \cdot g \cdot \frac{M_c}{M_b} \cdot \left[ 1 + \frac{2\alpha_s}{3\pi} f(\lambda) \right] \cdot S \\ &= \frac{M_b^5}{M_\mu^5} \cdot g \cdot \left[ 1 + \frac{2\alpha_s}{3\pi} f(\lambda) \right] \cdot S \cdot \Gamma(\mu \rightarrow e\nu \bar{\nu}) \end{aligned} \quad (2.4)$$

where  $M_s$ ,  $M_c$ , and  $M_b$  are the masses of the  $s$ ,  $c$ , and  $b$  quarks,  $g$  is a phase space factor, and  $f(\lambda)$  is a factor due to first-order QCD corrections and  $\lambda = \frac{M_q}{M_Q}$ . The

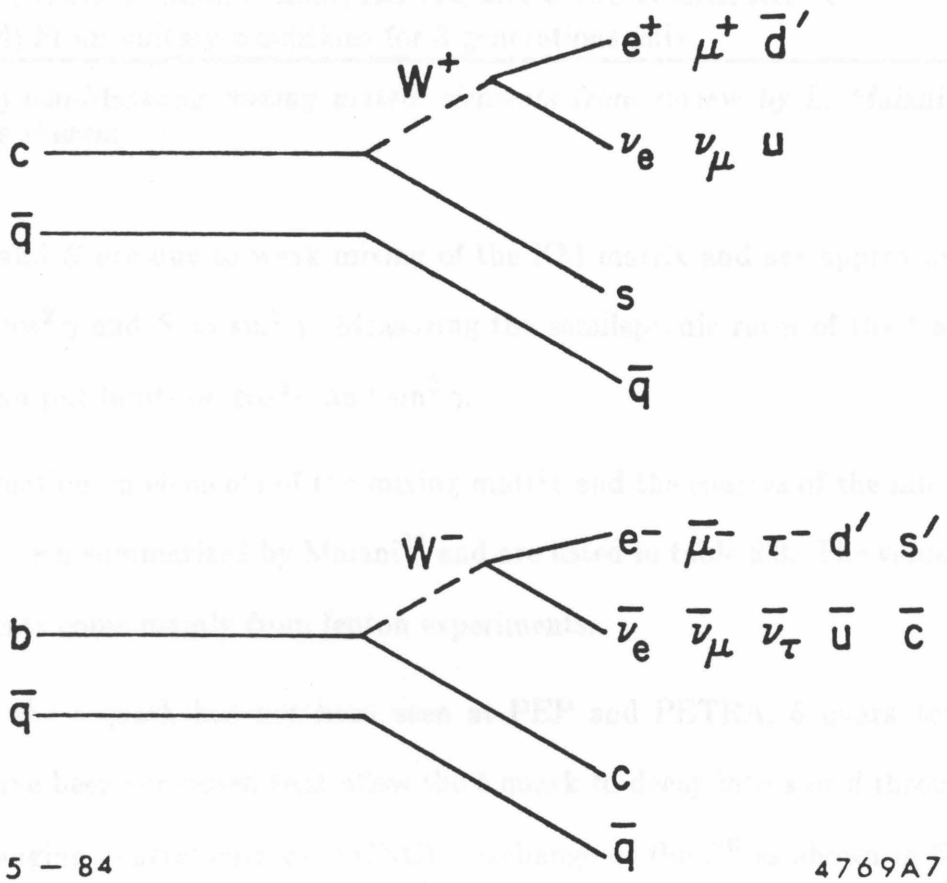


Fig. 2.4 Spectator diagrams for  $c$  and  $b$  decay.

**Table 2.3 Kobayashi-Maskawa Matrix Elements.**

	u	c	t
d	$U_{ud} = 0.9737 \pm 0.0025^a$	$U_{cd} = 0.225 \pm 0.005^b$	$0.0 <  U_{td}  < 0.09^d$
s	$U_{us} = 0.24 \pm 0.03^a$	$0.59^b <  U_{cs}  < 0.97^d$	$0.44^c <  U_{ts}  < 0.78^d$
b	$0.0 <  U_{ub}  < 0.11^d$	$0.0 <  U_{cb}  < 0.78^d$	$0.62^d <  U_{tb}  < 1.0$
(a) From hyperon and kaon $\beta$ decays, Ref. 40. (b) From dimuon, neutrino and antineutrino data, CDHS, Ref. 43. (c) JADE $B$ lifetime limit, Ref. 44, and CUSB results, Ref. 4. (d) From unitary conditions for 3 generations only			

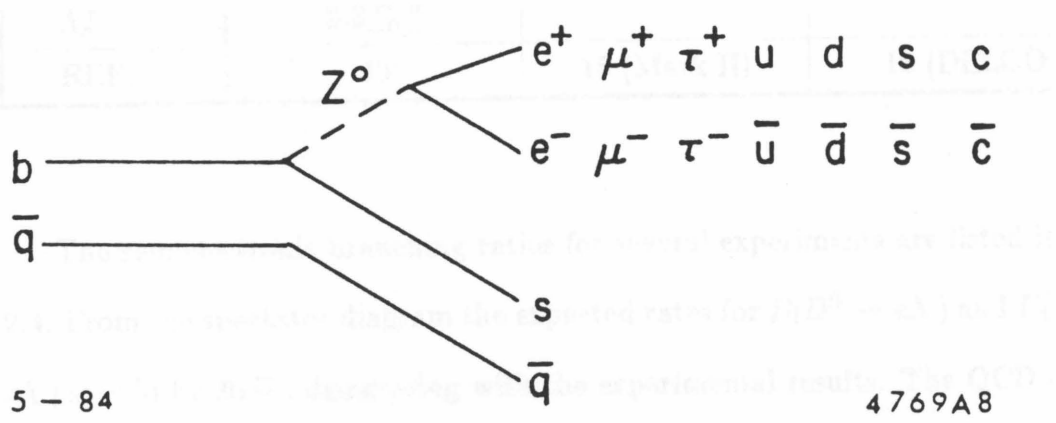
*Kobayashi-Maskawa mixing matrix elements from review by L. Maiani and references therein.*

terms  $C$  and  $S$  are due to weak mixing of the KM matrix and are approximated by  $C = \cos^2 \gamma$  and  $S = \sin^2 \gamma$ . Measuring the semileptonic rates of the  $b$  and  $c$  mesons can put limits on  $\cos^2 \gamma$  and  $\sin^2 \gamma$ .

Information on elements of the mixing matrix and the sources of the information have been summarized by Maiani<sup>39</sup> and are listed in table 2.3. The values for the elements come mainly from lepton experiments.

Since the  $t$  quark has not been seen at PEP and PETRA, 5 quark topless models have been suggested that allow the  $b$  quark to decay into  $s$  or  $d$  through a flavor changing neutral current (FCNC) exchange of the  $Z^0$  as shown in figure 2.5. Results from CESR on dielectron rates show these models to be unlikely.

The diagrams shown in figure 2.4 are examples of spectator decays of heavy quarks. The heavy quark decays by emitting a virtual  $W$  and the light quark acts as a spectator. If this model were correct, it would imply equal lifetimes and semileptonic rates for the heavy hadrons. Experimentally, as discussed in Section 1.1, this is not the case. Results on lifetime measurements<sup>40</sup> for the charmed  $D^0$



5 - 84

4769A8

Fig. 2.5 FCNC decay of  $b$  into  $e^+e^-$  pairs.

and  $D^\pm$  mesons give a world average of

$$\frac{\tau(D^+)}{\tau(D^0)} = 2.2^{+0.9}_{-0.6} .$$

**Table 2.4 Lifetimes and Semielectronic Rates for Charmed Hadrons.**

Particle	$\tau, (10^{-13}s)$	Semielectronic Rate, (%)	
$D^0$	$4.0^{+1.2}_{-0.9}$	$5.5 \pm 3.7$	$< 4 (.90 \text{ CL})$
$D^+$	$9.3^{+2.7}_{-1.8}$	$16.8 \pm 6.4$	$22.0^{+4.4}_{-2.2}$
$F^+$	$2.9^{+1.8}_{-0.9}$		
$\Lambda_c^+$	$2.2^{+0.9}_{-0.5}$		
REF.	40	15 (Mark II)	16 (DELCO)

The semielectronic branching ratios for several experiments are listed in table 2.4. From the spectator diagram the expected rates for  $B(D^0 \rightarrow eX)$  and  $B(D^+ \rightarrow eX)$  should be 20% , disagreeing with the experimental results. The QCD corrections in equations (2.3) and (2.4) decrease these rates slightly, but not enough to explain the experimental results. The current consensus is that there are two predominant sources of corrections to the spectator model: interference effects of identical particles in the final state and non-spectator interactions of the heavy quark with the light spectator quark.

There is negative interference between the  $\bar{d}$  from the decay of the  $c$  and the spectator  $\bar{d}$  in the  $D^+$  diagram. This tends to increase the  $D^+$  lifetime and semielectronic rates.

The interactions of spectator quarks in the decays of  $D^0$ ,  $D^+$ ,  $F^+$ , and  $\Lambda_c^+$  are shown in figure 2.6. The diagram for the  $D^+$  decay is Cabibbo suppressed, so

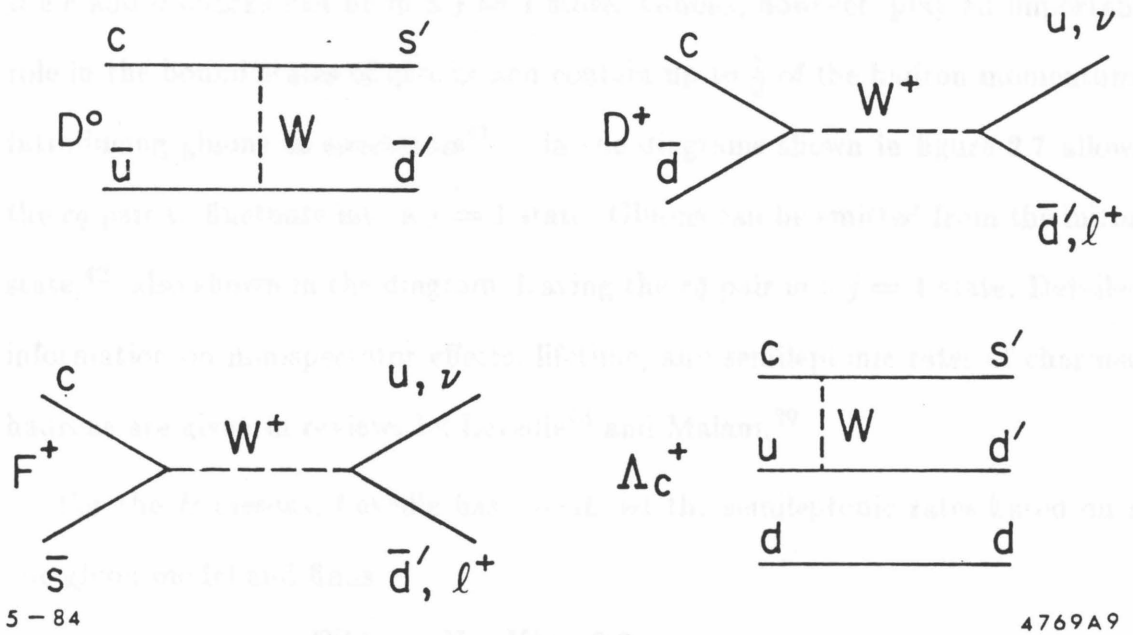


Fig. 2.6 Non-spectator diagrams for  $D^0$ ,  $D^+$ ,  $F^+$ , and  $\Lambda_c^+$  decay.

the addition of these diagrams would decrease the lifetimes and semileptonic rates of the  $D^0$ ,  $F^+$  and  $\Lambda_c^+$  relative to those for  $D^+$ . For the mesons the diagrams are helicity suppressed since they are in  $j = 0$  states and the decay can proceed via left-handed currents only. If the helicity suppression were relieved, the results in table 2.4 could be explained. The  $\Lambda_c^+$  diagram is not helicity suppressed since the  $c$  and  $d$  quarks can be in a  $j = 1$  state. Gluons, however, play an important role in the bound states of quarks and contain up to  $\frac{1}{2}$  of the hadron momentum. Introducing gluons as spectators<sup>41</sup> in the diagrams shown in figure 2.7 allows the  $c\bar{q}$  pair to fluctuate into a  $j = 1$  state. Gluons can be emitted from the initial state,<sup>42</sup> also shown in the diagram, leaving the  $c\bar{q}$  pair in a  $j = 1$  state. Detailed information on non-spectator effects, lifetime, and semileptonic rates of charmed hadrons are given in reviews by Leveille<sup>43</sup> and Maiani.<sup>39</sup>

For the  $B$  mesons, Leveille has calculated the semileptonic rates based on a one gluon model and finds

$$B(b\bar{u} \rightarrow eX, \mu X) \approx 0.3$$

$$B(b\bar{d} \rightarrow eX, \mu X) \approx 0.3 \left( \frac{1}{1 + 1.2f_b^2} \right) ,$$

where  $f_b^2$  is proportional to the probability that the  $b\bar{q}$  pair are at the origin and is less than 0.5 . For  $f_b = 0$  we obtain the spectator diagrams. For  $f_b = 0.5$  and assuming  $B(b \rightarrow c) \approx 1$  we obtain

$$B(B^- \rightarrow eX) \approx 15\%$$

$$B(B^0 \rightarrow eX) \approx 11.5\% .$$

The spectator diagrams are more accurate for the more massive  $b$  quark, giving an expected semielectronic rate of 14.4%.

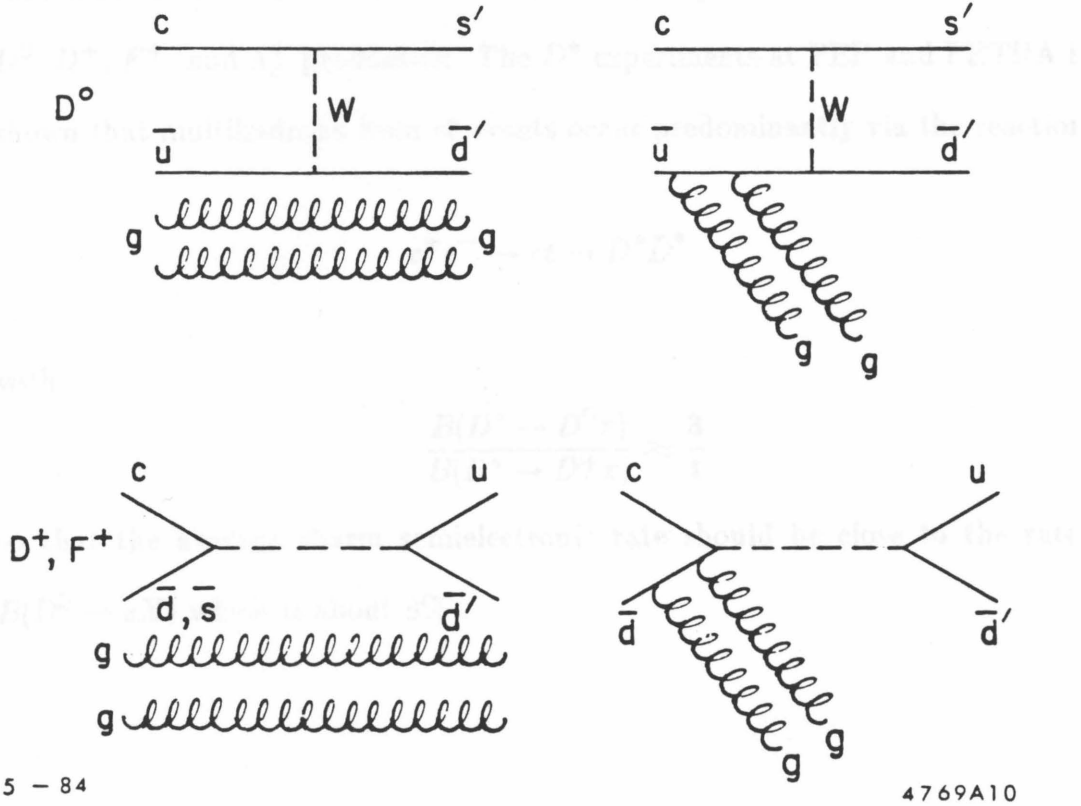


Fig. 2.7 Gluons enhanced non-spectator diagrams.

The semielectronic rates for  $b$  and  $c$  are measured in this analysis, averaged over all heavy hadrons containing  $b$  and  $c$  quarks produced in multihadron events. The rates for the different  $b$  flavored hadrons should be approximately equal and should be about 15%. The rate for  $c$  hadrons is dependent on the relative rates of  $D^0$ ,  $D^+$ ,  $F^+$ , and  $\Lambda_c^+$  production. The  $D^*$  experiments at PEP and PETRA have shown that multihadrons from  $c\bar{c}$  events occur predominantly via the reaction

$$e^+e^- \rightarrow c\bar{c} \rightarrow D^*\bar{D}^*$$

with

$$\frac{B(D^* \rightarrow D^0\pi)}{B(D^* \rightarrow D^+\pi)} \approx \frac{3}{1}$$

so that the average charm semielectronic rate should be close to the rate for  $B(D^0 \rightarrow eX)$  which is about 8% .

## CHAPTER 3

# Apparatus

### § 3.1 THE DELCO DETECTOR

The experiment was carried out at the PEP  $e^+e^-$  storage ring. This machine stores electrons and positrons in two sets of three countercirculating bunches in stable orbits of approximately 1.5 miles in circumference. The electrons and positrons are injected into the ring from the Stanford Linear Accelerator after being accelerated to a momentum of 14.5 GeV/c. The data collection for this experiment began at the time of PEP start-up in November 1982 and continued until spring of 1983. The average luminosity of the machine increased, over the period of this experiment, from  $7.5 \cdot (10^{30} \text{cm}^{-2} \text{s}^{-1})$  at start-up to a steady value of  $16 \cdot (10^{30} \text{cm}^{-2} \text{s}^{-1})$  in January 1983. The total integrated luminosity for the data used in this experiment is  $118.8 \text{ pb}^{-1}$ .

DELCO (Direct Electron Counter), shown in figure 3.1, is a special purpose detector emphasizing particle identification. The heart of the detector is a gas-filled threshold Čerenkov counter which surrounds the interaction point and enables  $e^\pm, \pi^\pm, K^\pm$  separation over certain kinematical regions. The Čerenkov counter is completely captured by drift chambers which provide tracking informa-

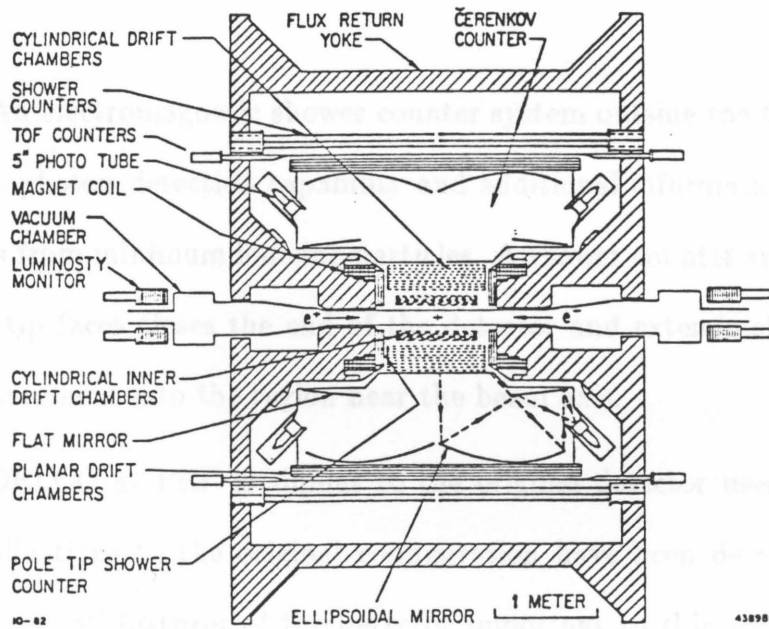
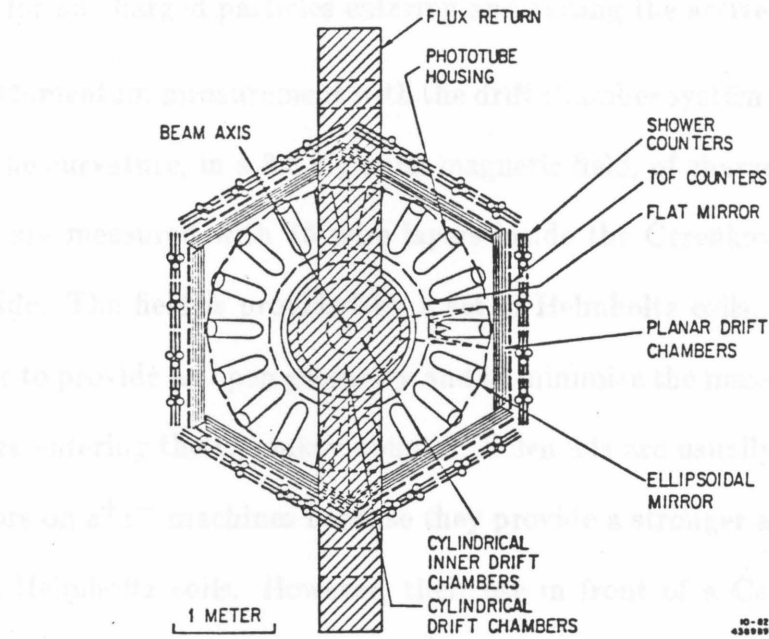


Fig. 3.1 The DELCO detector

tion for all charged particles entering and exiting the active region of the counter.

Momentum measurement with the drift chamber system is achieved by measuring the curvature, in a 3.3 Kg axial magnetic field, of charged particle trajectories that are measured with 16 wire layers inside the Čerenkov counter and 6 layers outside. The field is provided by a set of Helmholtz coils, which was selected in order to provide an open geometry and to minimize the mass traversed by particles before entering the Čerenkov counter. Solenoids are usually used in magnetic detectors on  $e^+e^-$  machines because they provide a stronger and more uniform field than Helmholtz coils. However, their use in front of a Čerenkov counter would cause a significant background due to electrons from photon conversions in the coil.

An electromagnetic shower counter system outside the Čerenkov counter provides photon detection capability and additional information for separating electrons from minimum ionizing particles. A shower counter system on the magnetic pole tip faces closes the end of the detector and extends electromagnetic energy measurement into the region near the beam axis.

DELCO at PEP is similar to the original detector used at SPEAR<sup>44</sup>. The modifications to the original configuration have been described elsewhere<sup>30,45</sup>, however, all features of the detector important to this analysis are described in the following sections. The overall performance characteristics of DELCO are summarized in table 3.1.

### § 3.2 DRIFT CHAMBER TRACKING SYSTEM AND MAGNET

Two systems of tracking chambers are used; a cylindrical chamber of 16 wire

**Table 3.1 Summary of Acceptance and Performance of the DELCO Detector.**

Region	Description
Magnet	Open-geometry (aperture $ \cos \theta  < 0.78$ ) Pole-tip diameter 101 cm, separation 125 cm $B_0 = 3.3\text{kG}$ , $\int Bdl = 1.8\text{kG}\cdot\text{m}$
Tracking	Central(cylindrical) drift chambers: 94 cm maximum wire length, 12-49 cm radius Low mass (2.3% $X_0$ ) Depth ( $z$ ) measurement by narrow angle stereo 16 points on track with $ \cos \theta  < 0.69$  Outer (planar) drift chambers: 285 cm wire length, 160 cm (radius) Depth measurement by wide angle stereo 6 points on track with $ \cos \theta  < 0.65$  Multiple hit digital electronics (4 ns bin width)
Čerenkov Counter	1 atm gas threshold counter 36 cells each with (pTP-coated) 5" RCA Quanticon Radiator length 55-110 cm, acceptance $ \cos \theta  < 0.65$ Isobutane: $\langle pe \rangle = 18$ , $\langle N_0 \rangle = 81\text{ cm}^{-1}$ $\sigma_t = 310\text{ ps}$ , $\gamma_t = 19.2$ Nitrogen: $\langle pe \rangle = 4.8$ , $\langle N_0 \rangle = 97\text{ cm}^{-1}$ $\sigma_t = 390\text{ ps}$ , $\gamma_t = 39.1$
Shower Counters	Barrel ( $ \cos \theta  < 0.58$ ): 48 Pb-scintillator counters, 6 $X_0$  Pole-tip ( $ \cos \theta  < 0.98$ ): 36 Pb-scintillator BBQ counters, 5 $X_0$
Time-of-Flight	52 scintillator counters 324 cm length, 180 cm $\langle \text{radius} \rangle$ $\sigma_t = 350\text{ ps}$ Acceptance $ \cos \theta  < 0.67$
Luminosity Monitor	12 Pb-scintillator BBQ counters, 16 $X_0$ Acceptance 25-68 mrad relative to beam axis

layers arranged in three physical units, in a 3.3 kg field parallel to the beam axis,

and an outer planar system of 6 layers in a hexagonal arrangement adjacent to the exit of the Čerenkov counter.

### 3.2.1 Central Drift Chambers

The inner section (IDC) of the central drift chamber system has 4 narrow angle stereo ( $uv$ ) layers at  $3^\circ$  to the beam axis and two axial ( $z$ ) layers parallel to the beam axis. The  $z$  layers provide radial and phi positions for tracks, and the  $u$  and  $v$  layers provide radial positions and positions along the direction of the beam axis. The IDC is a complete cylinder concentric to the beam pipe and centered on the interaction region (IR). Wire layers range radially 12.0 cm to 20 cm from the IR.

The IDC is captured by a split cylindrical drift chamber (CDC) which is removable in two half-cylinder sections to obtain access to the IDC. The CDC has 4 axial layers and 6 small angle stereo layers. The layers lie between 25 cm and 45 cm radially from the IR. The total central tracking system has 16 layers arranged  $uuzzzvzzuuzzzvzz$  to provide three-dimension track reconstruction.

There are 1216 sensing cells in the central drift chamber. Typical cell geometry is shown in figure 3.2. There is a single sense wire flanked above and below by guard wires, with three field wires on each side. The sense wires are gold-plated tungsten and are  $30\ \mu\text{m}$  in the IDC and  $40\ \mu\text{m}$  in the CDC. The field and guard wires are  $152\ \mu\text{m}$  beryllium-copper wires. Cell widths vary from 11.8 mm in the first layer to 24 mm in the outermost layer.

The cylindrical shells of the chambers are sandwich panels with two aluminum 5052 facings 0.1 mm thick glued to a core of HRH10/0X - 3/16 - 1.8(2) Hexcell

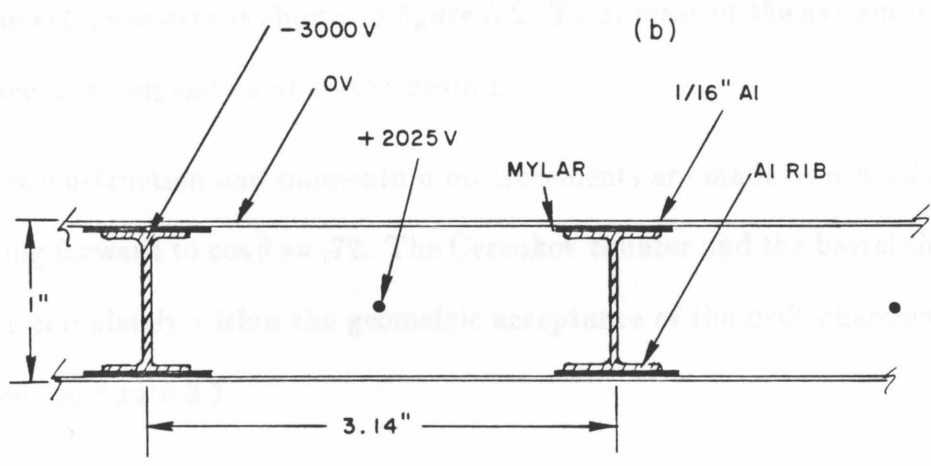
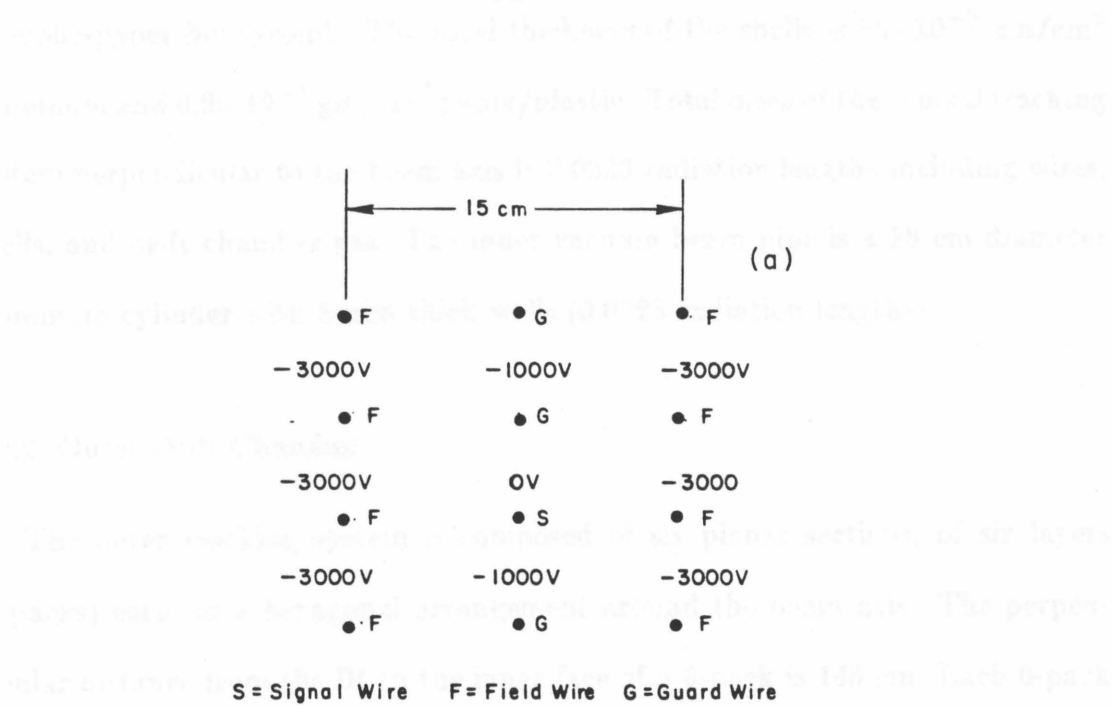


Fig. 3.2 Drift chamber cell geometries. (a) Cylindrical chambers. (b) Planar chambers.

phenolic-paper honeycomb. The total thickness of the shells is  $55 \cdot 10^{-3}$  gm/cm<sup>2</sup> aluminum and  $0.28 \cdot 10^{-3}$  gm/cm<sup>2</sup> paper/plastic. Total mass of the central tracking system perpendicular to the beam axis is 0.0233 radiation lengths including wires, shells, and drift chamber gas. The inner vacuum beam pipe is a 16 cm diameter aluminum cylinder with 2 mm thick walls (0.0225 radiation lengths).

### 3.2.2 Outer Drift Chamber

The outer tracking system is composed of six planar sections, of six layers (6-packs) each, in a hexagonal arrangement around the beam axis. The perpendicular distance from the IR to the inner face of a 6-pack is 145 cm. Each 6-pack has 4 axial ( $z$ ) layers and a pair of stereo ( $uv$ ) layers. There are 792 cells 8 cm wide and 2 cm high with a single 40  $\mu$ m gold-plated tungsten sense wire in the center. The cell geometry is shown in figure 3.2. Total mass of the system is .318 radiation lengths perpendicular to the beam axis.

Track reconstruction and momentum measurements are made over a solid angle extending forward to  $\cos \theta = .72$ . The Čerenkov counter and the barrel shower counter are completely within the geometric acceptance of the drift chamber systems, as seen in figure 3.1.

### 3.2.3 Drift Chamber Characteristics

The distance of closest approach (DCA) of particle trajectories to signal wires is determined from drift times in the cells. The drift time is the time difference from when the particle passes through the cell to the time of the signal. The time is measured with a grey code generator with a 4 nsec clock rate. The start time is

measured by probes that sense the electron bunches just before they pass through the interaction point.

The typical drift velocity for the gas used is  $50 \mu\text{m}/\text{nsec}$ . The gas used during 1982 was a 55/45 mix of  $\text{Ar}/\text{C}_2\text{H}_6$ . About 80% of the data was collected after the gas was replaced by  $\text{Ar}/\text{CO}_2/\text{CH}_4$  in 1983 to prevent the buildup of carbon whiskers on the drift chamber wires. The mechanism of whisker growth is not understood; however, it does not occur in the  $\text{Ar}/\text{CO}_2/\text{CH}_4$  mixture.

**Table 3.2 Drift Chamber Characteristics.**

Chamber	Layers	Radius, (cm)	Resolution	Efficiency
IDC	1 - 6	12 - 20	$150 \mu\text{m}$	$>.99$
CDC	7 - 16	20 - 50	$190 \mu\text{m}$	$>.99$
PDC	17 - 22	140 - 170	$450 \mu\text{m}$	$>.98$

*Drift chamber characteristics found from track reconstruction of Bhabha electrons within the geometric acceptance of the chambers.*

Each of the signal wires has its own zero-pole preamp and line driver, which were made exclusively for the DELCO drift chamber system. The signals are sent over twisted pairs to the counting house. The data acquisition can accept up to eight hits, spaced at least 3 mm apart, from an individual wire allowing multi-hit capability within individual cells. Table 3.2 lists the average resolution for determining the DCA in each of the DC systems along with the average wire efficiency for electrons from Bhabha events.

Track reconstruction is best for isolated tracks, such as those from Bhabha electrons. For these tracks the drift chamber system has the following measurement resolutions:

Dip angle,  $\sigma_\theta = 3$  mrad

Azimuthal angle,  $\sigma_\phi = 2.6$  mrad

Distance of closest approach to beam axis,  $\sigma_R = 380 \mu\text{m}$

Distance of closest approach to  $Z=0$ ,  $\sigma_Z = 2.3$  mm

### 3.2.4 Magnetic Field and Momentum Measurement

The magnetic field is provided by an open geometry magnet with a central field of 3.3 kg and an integrated field strength of 1.8 kg-m radially through the central tracking system. A cross section of the magnet is shown in figure 3.3. Only one quarter of the magnet is shown since it is mirror symmetric about the horizontal and vertical midplanes. The field is not as uniform as the fields in solenoidal coils; however, a precise field map is used for determining the momenta of charged particles.

The coils contain 236 turns of copper rated at 3000 amperes. At the maximum current, the iron return yoke is saturated causing a stable field strength. The field is continuously monitored with a Hall probe during operation.

Momentum determination is accomplished by measuring track curvature in the IDC/CDC and projecting out to the PDC where the long lever arm gives additional precision. The momentum measurement error, for tracks constrained to the origin, is  $\sigma_p/p = \sqrt{(.02p)^2 + .06^2}$  where  $p$  is in Gev/c. The .06 error is due to multiple scattering; the .02 $p$  is due to survey, calibration, and track reconstruction resolution. Figure 3.4 shows momentum resolution for 14.5 Gev/c electrons from Bhabha events.

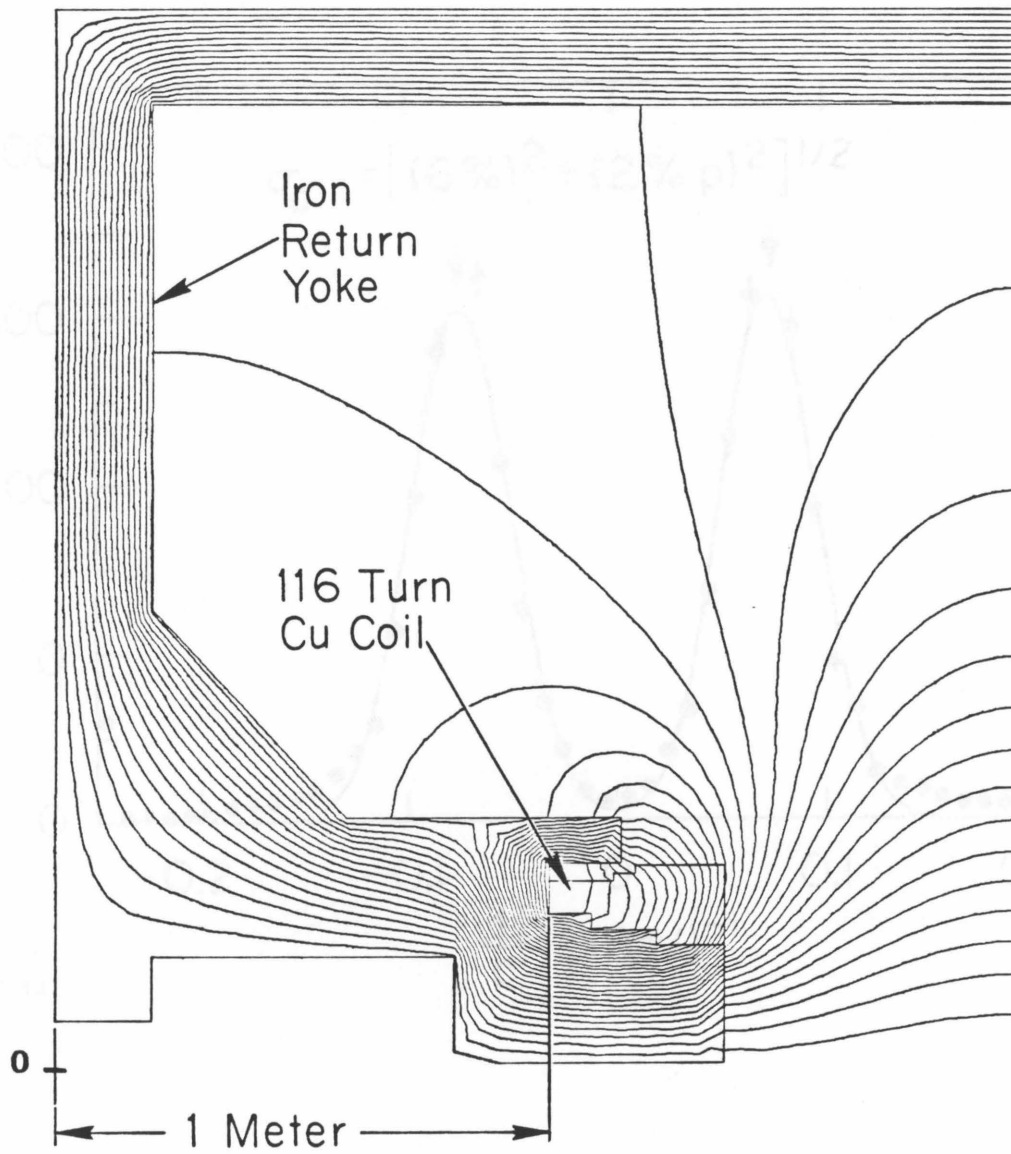


Fig. 3.3 DELCO magnet field map.

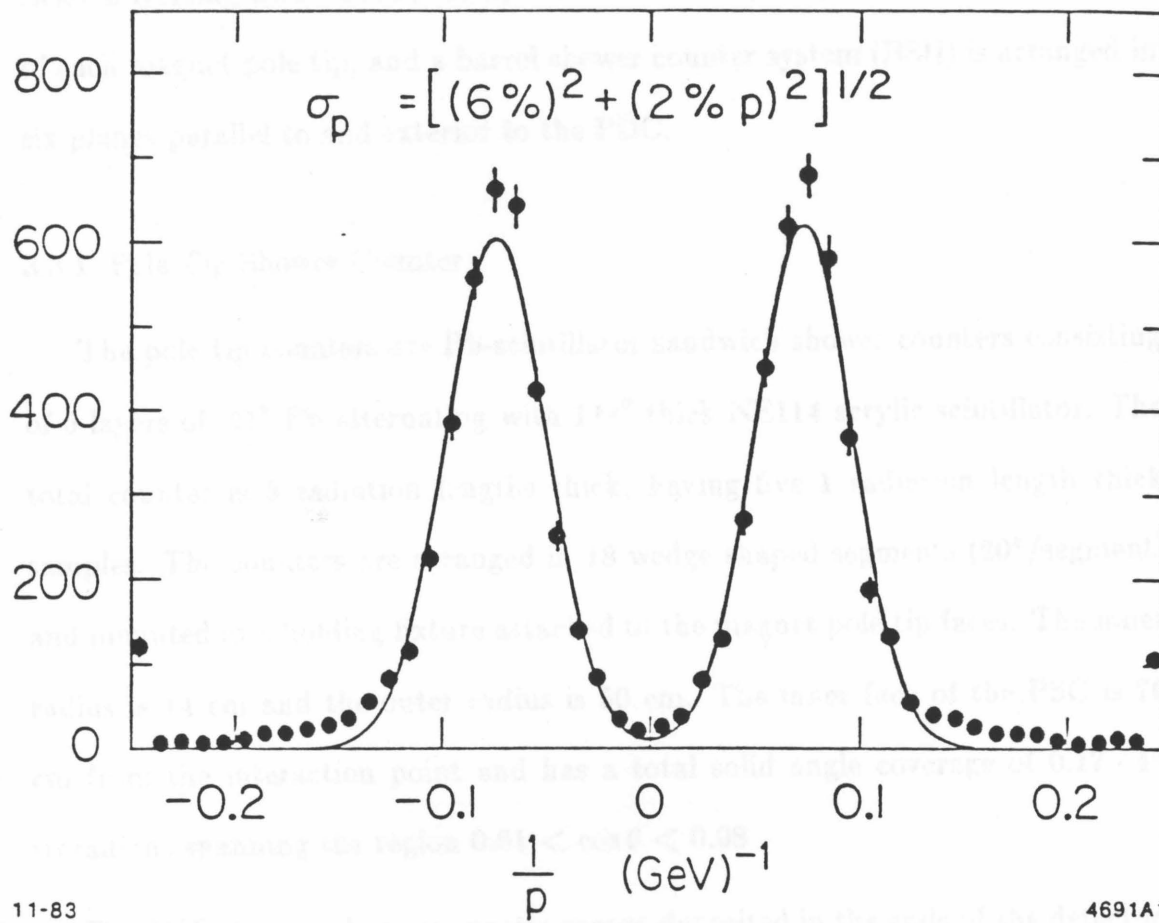


Fig. 3.4 Momentum resolution of 14.5 GeV/c Bhabha electrons.

### § 3.3 ELECTROMAGNETIC SHOWER COUNTER SYSTEMS

Two systems of shower counters provide measurements of energy loss for particles traversing DELCO. A pole tip shower counter (PSC) is mounted on the face of each magnet pole tip, and a barrel shower counter system (BSH) is arranged in six planes parallel to and exterior to the PDC.

#### 3.3.1 Pole Tip Shower Counter

The pole tip counters are Pb-scintillator sandwich shower counters consisting of 5 layers of .21" Pb alternating with 1/4" thick NE114 acrylic scintillator. The total counter is 5 radiation lengths thick, having five 1 radiation length thick samples. The counters are arranged in 18 wedge shaped segments ( $20^\circ$ /segment) and mounted in a holding fixture attached to the magnet pole tip faces. The inner radius is 14 cm and the outer radius is 50 cm. The inner face of the PSC is 70 cm from the interaction point and has a total solid angle coverage of  $0.17 \cdot 4\pi$  steradians spanning the region  $0.81 < \cos \theta < 0.98$ .

The PSC detects electromagnetic energy deposited in the ends of the detector; is calibrated with small angle Bhabha events; and has an energy resolution for electromagnetic showers of  $25\%/E(\text{Gev})$ .

#### 3.3.2 Barrel Shower Counter System

The barrel shower counter is used as a thin shower counter in the off-line analysis and in the on-line trigger. It is composed of 48 paddles of Pb-scintillator shower counters of 3 layers of 0.5" thick Pb alternated with 0.5" of NE110 acrylic

**Table 3.3 Material in DELCO,  $\chi/\chi_0$ .**

Component		Individual	Total
Vacuum Pipe	aluminum	22.5	22.5
	hexcell	5.9	
IDC	entrance	7.0	34.7
	gas, wires	3.3	
	exit	1.9	
CDC	entrance	3.5	45.8
	gas, wires	4.1	
	exit	3.5	
Čerenkov Counter	entrance-old	4.0	49.8
	entrance-new	1.4	
	isobutane	4.7	
	nitrogen	2.6	
	mirror-frame	54.	
	exit	71.	
PDC	6 layers	318.	498.
ToF	ToF,supports	82.	580.
BSH	A layer	2352.	2930.
	B layer	2281.	
	C layer	2281.	

Material in DELCO (in radiation lengths times  $10^{-3}$ ) for trajectories perpendicular to the beam axis.

scintillator. The total thickness is 6.9 radiation lengths thick, with an additional .6 radiation lengths of material in the detector interior to the BSH. Table 3.3 summarizes the materials in the inner detector and the corresponding mass in radiation lengths. The BSH paddles extend 143.5 cm from each side of the midplane of the detector normal to the beam axis and are 45 cm wide. They are arranged in 6 planes of four paddle-sandwiches parallel to and immediately exterior to the PDC. The perpendicular distance from the BSH inner face to the IR is 180 cm, and total geometric acceptance is  $0.52 \cdot 4\pi$  steradians.

The BSH is used in conjunction with the Čerenkov counter to achieve additional separation of electrons from hadrons. In particular, the BSH is used to help distinguish electron tracks from hadron tracks that occupy the same Čerenkov cell by determining which track has associated electromagnetic energy.

Calibration of the BSH system is done using minimum ionizing particles (MIPs), such as pions that are found in  $2\text{-}\gamma$  events, and using the Čerenkov counter to veto electrons. Pulse heights ( $P_h$ ) in the photomultiplier tubes (PMTs), due to MIPs in the individual BSH layers, are given as

$$P_h = G_n \exp(-\lambda_n z) / \cos \theta \quad ,$$

where  $z$  is the distance from the PMT to the point where the particle trajectory intersects the counter,  $\lambda_n$  is the inverse of attenuation length of light in the scintillator, and  $\theta$  is the angle of incidence of the track with the counter.  $G_n$  is a constant for counter  $n$  determined by the gain of the PMT and associated ADC. The gain is set so a MIP at normal incidence will give ten counts in the 2048 channel ADC associated with the counter. This corresponds to about 240 counts for an electromagnetic shower due to a 1 Gev photon. In the off-line analysis the BSH is calibrated so that the average response of all MIPs is 1 gap crossing (gx) in each counter layer, after all corrections, by fitting the following equation

$$\log\left(\frac{A_n}{G_n} P_h \cos \theta\right) = \lambda_n z \quad ,$$

adjusting  $\lambda_n$  and a calibration constant  $A_n$  for each counter,  $n$ . The typical BSH response for MIPs is shown in figure 3.5 along with the Monte Carlo simulated

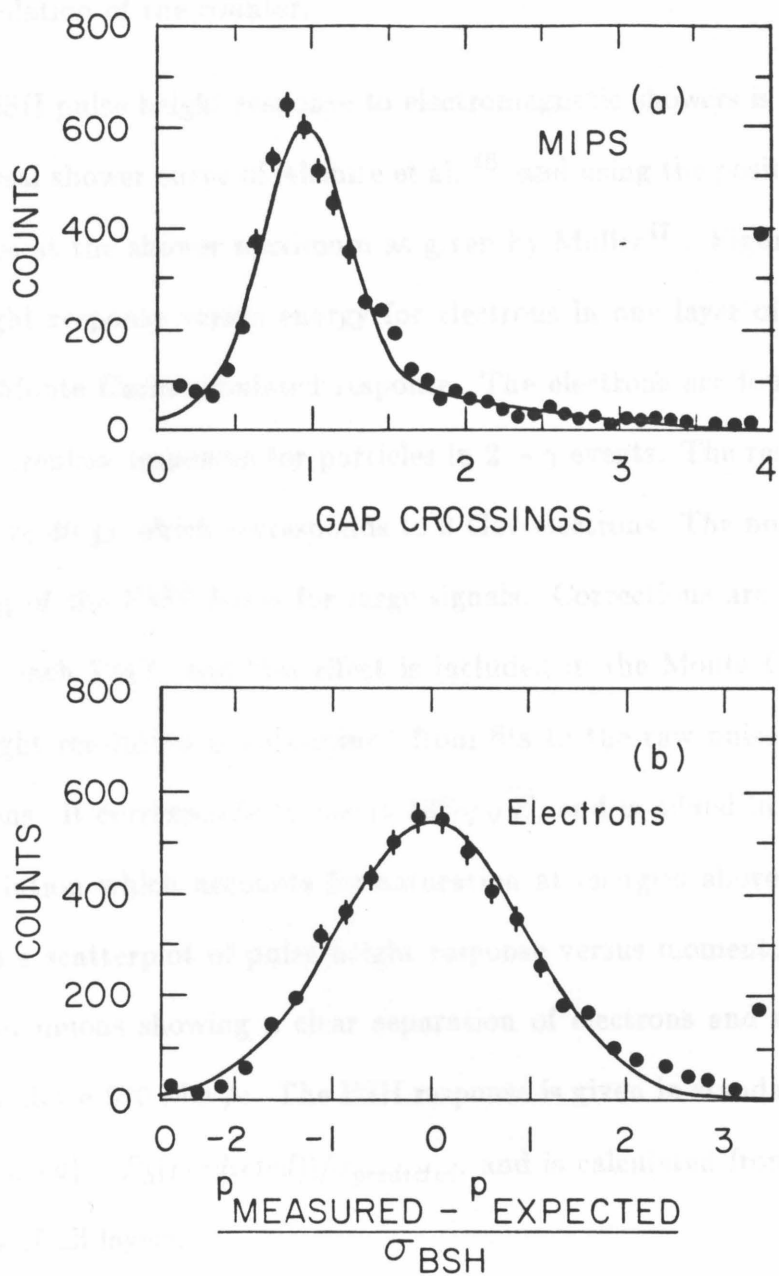


Fig. 3.5 Barrel shower counter pulse height response. (a) Response for MIPS,  $\mu$ 's and  $\pi$ 's in 2- $\gamma$  events. (b) Response for electrons compared to expected response.

response. The shape of the distribution is fitted with two Gaussians for Monte Carlo simulation of the counter.

The BSH pulse height response to electromagnetic showers is evaluated using the universal shower curve of Abshire et al.,<sup>46</sup> and using the position and number of particles at the shower maximum as given by Muller<sup>47</sup>. Figure 3.5 shows the pulse height response versus energy for electrons in one layer of the BSH along with the Monte Carlo simulated response. The electrons are found by requiring positive Čerenkov responses for particles in  $2 - \gamma$  events. The responses are non-linear above 40 gx which corresponds to 3 Gev electrons. The nonlinearity is due to sagging of the PMT bases for large signals. Corrections are made to the response of each PMT, and this effect is included in the Monte Carlo simulation. Pulse height resolution is determined from fits to the raw pulse height response to electrons. It corresponds to about  $33\%/\sqrt{E}$ , and is added in quadrature to a 17% resolution which accounts for saturation at energies above 3 Gev. Figure 3.6 is a scatterplot of pulse height response versus momentum for electrons, pions, and muons showing a clear separation of electrons and non-electrons for momenta above 500 Mev/c. The BSH response is given in standard deviations by  $(P_h(\text{measured}) - P_h(\text{predicted}))/\sigma_{\text{predicted}}$ , and is calculated from the sum of the responses of all layers.

### § 3.4 ČERENKOV COUNTER

The large-solid-angle gas-filled counter is a UV Čerenkov light detector which operates at atmospheric pressure in the threshold mode for separation of electrons, pions, and kaons. The basic design is similar to the Čerenkov counter used in

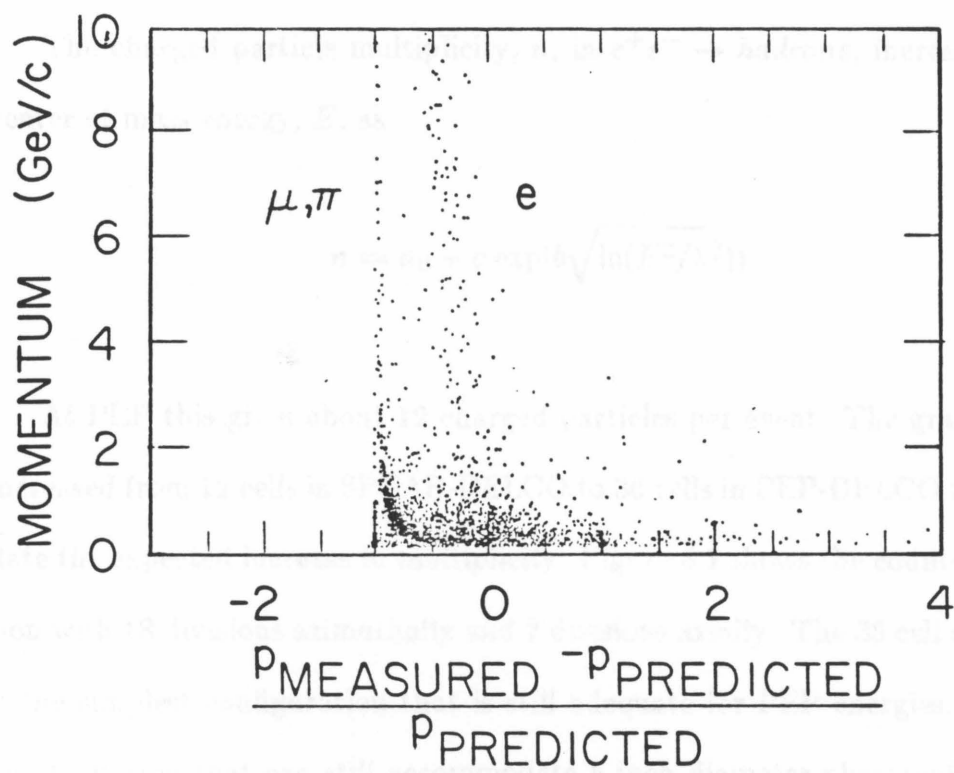


Fig. 3.6 Scatterplot of shower counter response vs. momentum.  $\mu, \pi$ , and electron tracks in  $2\text{-}\gamma$  events.

DELCO at SPEAR<sup>48</sup>. The new counter uses the same outer hexagonal shell, but has new optical components to extend light collection into the UV spectrum, and has finer granularity.

### 3.4.1 Design Considerations

The charged particle multiplicity,  $n$ , in  $e^+e^- \rightarrow \text{hadrons}$ , increases with the center of mass energy,  $E$ , as

$$n = n_0 + a \exp(b\sqrt{\ln(E^2/\lambda^2)}) .$$

At PEP this gives about 12 charged particles per event. The granularity was increased from 12 cells in SPEAR-DELCO to 36 cells in PEP-DELCO to accommodate the expected increase in multiplicity. Figure 3.1 shows the counter configuration with 18 divisions azimuthally and 2 divisions axially. The 36 cell arrangement is the simplest configuration that is still adequate for PEP energies. This is the finest division that can still accommodate 5 inch diameter photomultiplier tubes and their magnetic shields.

For particle identification in threshold counters, a lower limit is usually set on the pulse height required for a positive signal. The response follows Poisson statistics, so large average signals give low inefficiency. Also, tracks in multiply hit cells can be distinguished by pulse height analysis if good pulse height resolution is achieved. Hence, the performance of the Čerenkov counter can be judged by the average number of photoelectrons detected for particles with momentum above threshold.

### 3.4.2 Čerenkov Light Yield

According to the Čerenkov radiation formula the number of photons emitted per frequency interval is

$$dN/d\nu = 2\pi\alpha \cdot L \cdot \sin^2 \theta_c \quad ,$$

where  $L$  is the radiator path length and  $\theta_c$  is the Čerenkov angle determined by the velocity,  $\beta$ , and the index of refraction of the radiating medium,  $n$ , given by

$$\cos \theta_c = \frac{1}{n\beta} \quad .$$

The number of photons emitted between two wavelengths can be written as

$$N = 2\pi\alpha \cdot L \cdot \sin^2 \theta_c \int \frac{d\lambda}{\lambda^2} \quad .$$

The number of photoelectrons detected can be calculated

$$n_e = N_0 \cdot L \cdot \sin^2 \theta_c \quad (3.1) \quad ,$$

where

$$N_0 = 2\pi\alpha \int Q(\lambda) \frac{d\lambda}{\lambda^2} \quad .$$

$Q(\lambda)$  is the product of radiator transmissivity, mirror reflectivity, photocathode quantum efficiency, and collection efficiency of the first dynode of the PMT used.

The photoelectron yield can be rewritten for  $n$  close to one as

$$n_e = N_0 \cdot L \cdot \epsilon \quad ,$$

where  $\epsilon = n - 1$ .

The three quantities  $N_0$ ,  $L$ , and  $\epsilon$  should be as large as possible to achieve high photoelectron yield and good resolution. Since the light yield falls as  $1/\lambda^2$ , the low wavelength limit of the counter must be kept as low as possible to achieve large  $N_0$ . The path length,  $L$ , is constrained in DELCO by the positions of the other counter systems, and averages 80cm. It is desirable to have  $\epsilon$  as large as possible, but, since this determines particle thresholds, the choice of radiator depends on the physics one wishes to do.

### 3.4.3 Construction

The counter uses 36 ellipsoidal mirrors which reflect Čerenkov light, originating near the interaction point, to a PMT. A set of three mirrors is used in each cell as shown in figure 3.7. The positions of the mirrors are constrained by the physical limitations of DELCO. A computer ray-tracing program was used to find the optical solution that had the longest average radiator path length, angular coverage greater than  $\pm 45^\circ$ , and a secondary focus outside of the endwall of the counter. The geometric efficiency for straight tracks coming from the origin and intersecting the ellipsoidal mirror away from the edge is 100%. Some loss occurs for low momentum tracks that bend in the fringe field of the DELCO magnet, and there is some loss and cross talk for trajectories near mirror edges. These problems are discussed in the section on Čerenkov counter performance.

The outer envelope or shell was recycled from the SPEAR-DELCO counter. It consists of a  $3/8''$  aluminum skin, which makes up the six outer planes of the hexagonal box, and  $1''$  aluminum end walls. The inner cylindrical window was

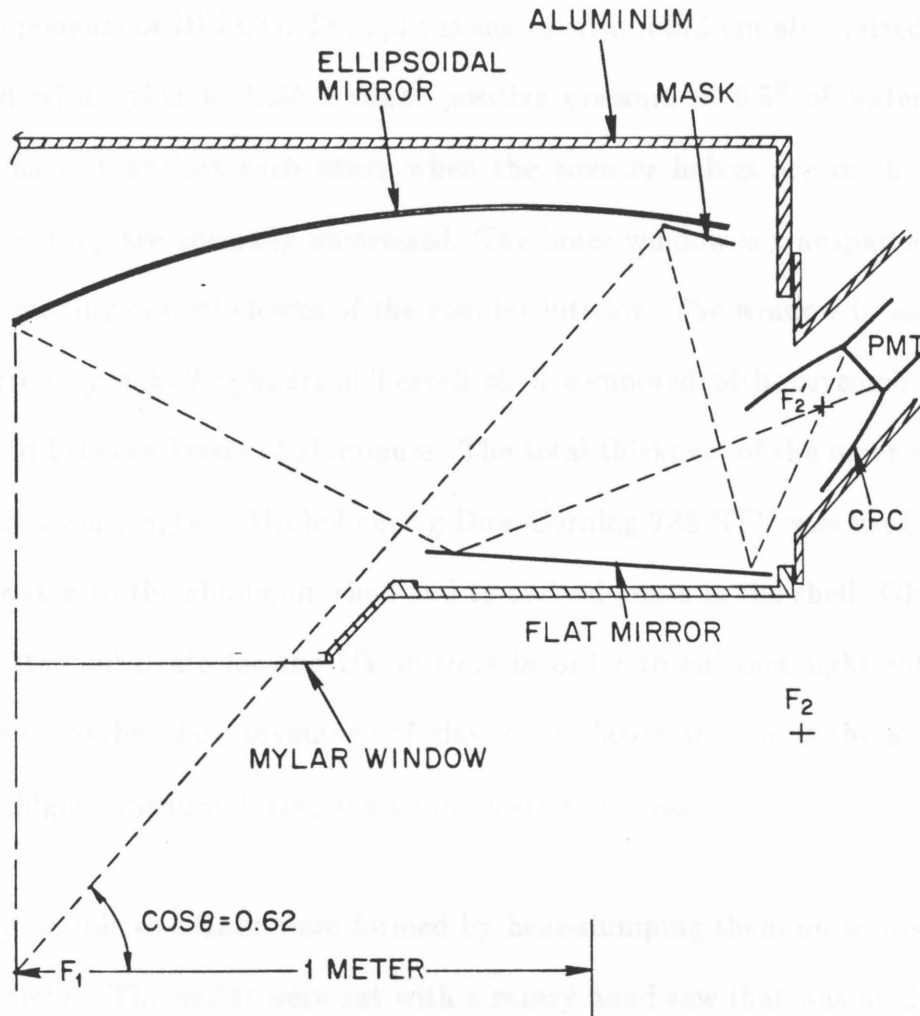


Fig. 3.7 Čerenkov counter optics

enlarged to 60 cm radius to accommodate the new CDC. The counter was split into two halves and mounted in moveable clamshells to permit easy access to the inner components of DELCO. The split is sealed with .0075 cm aluminized mylar reinforced with nylon to hold a slight positive pressure of 0.5" of water. The mylar skins rest against each other when the counter halves are in the closed position, so they are normally unstressed. The inner window is transparent 5 mil mylar permitting optical checks of the counter interior. The window in each half is supported by a half cylindrical hexcell shell composed of honeycomb plastic sandwiched between layers of aluminum. The total thickness of the inner window is .005 radiation lengths. Alcohol curing Dow Corning 738 RTV was used to seal the mylar skin to the aluminum shell and to seal all joints in the shell. Glass was chosen as the substrate for the UV mirrors in order to enhance light collection at low wavelengths. The advantage of glass over plastic or resin is the ability to achieve a higher vacuum during the aluminization process.

The glass mirror blanks were formed by heat-slumping them on to machined graphite molds. The molds were cut with a rotary hand saw that was modified to ride on two aluminum rails which followed the curve of the desired ellipse. The rails were suspended from a pivot at the axis of revolution of the ellipsoid and were swung back and forth across the graphite blocks by a reversing motor and cable system. The saw was pneumatically stepped along the rails by a preset distance after each sweep across the blocks. The blocks were finished by hand sanding. The mirrors were split and made in two sections for ease of handling and to reduce the amount of slumping. Two blocks were machined for each section. Smoked glass was used to eliminate any problem with light produced in the glass itself. The

blanks were 1/4" plate glass and were about 40 cm by 60 cm. Slumping was done in a metal-brazing bell oven at just above the annealing point, 600°C, for eight hours. The slumped glass was optically mapped to find the desired section of the ellipse, and was cut to the desired dimensions.

The mapping was done by placing the blanks in a cradle with an ellipsoidal shape, a point light source at one focus, and a screen at the other focus. Typical spot size on the screen from light covering about 80% of the glass at one time was 2 cm along the axis of rotation and .5 cm along the direction of rotation. Imperfections in the glass could easily be seen by eye, and a laser-mirror assembly was used to map their severity. The laser source was placed at one focus and the spot on the screen was traced as the laser was swept over the distorted area. Blanks were rejected if the spot on the screen deviated more than 5 cm from the focus. The final target was a 12 cm diameter PMT with a 22 cm diameter light collecting cone. When the blanks were correctly positioned, the best image of the point source ( actually a 1/8" diameter point) was obtained on the screen. A wood template was clamped onto the reflecting side to serve as a guide for the scribe used to cut the glass.

The mirrors were coated with 75 nm of aluminum by vacuum deposition. To achieve high reflectivity below 200 nm wavelength, a 25 nm layer of  $MgF_2$  must be applied within 1 second after aluminization to stop oxidation. The process must be done in a vacuum of about  $10^{-7}$  torr which is very difficult with any large area of an outgassing substrate such as acrylic or epoxy. Reflectivity for the finished mirrors is shown in figure 3.8 according to manufacturer's specifications<sup>49</sup>. The actual reflectivity was monitored with small test mirrors which were coated

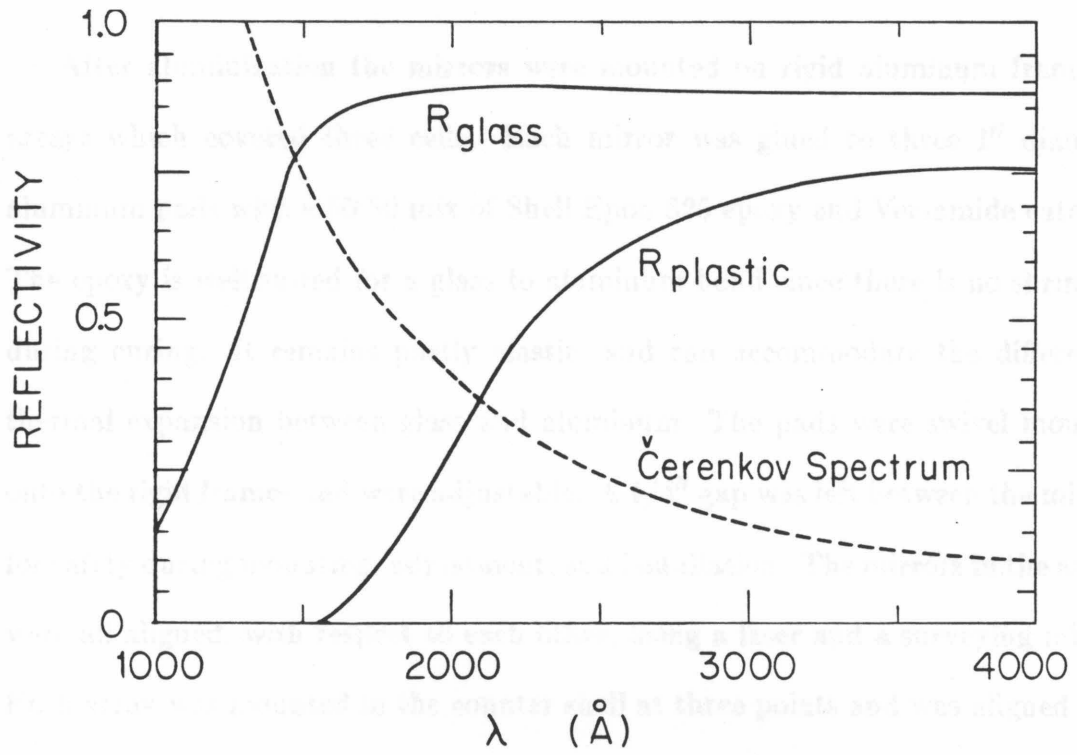


Fig. 3.8 Mirror reflectivity

alongside the large mirrors. Also, one ellipsoidal mirror was cut into test samples and measured, and the reflectivity agreed with specifications.

The SPEAR-DELCO ellipsoidal mirrors were a composite fiberglass epoxy resin with a gelcoat surface. The aluminization was done at  $10^{-5}$  torr. Reflectivity curves of  $2'' \times 2''$  plastic pieces, which were located alongside the ellipsoidal mirrors, are also shown in figure 3.8.

After aluminization the mirrors were mounted on rigid aluminum frames in arrays which covered three cells. Each mirror was glued to three  $1''$  diameter aluminum pads with a 50:50 mix of Shell Epon 825 epoxy and Versamide catalyst. The epoxy is well suited for a glass to aluminum bond since there is no shrinkage during curing. It remains partly elastic, and can accommodate the differential thermal expansion between glass and aluminum. The pads were swivel mounted onto the rigid frames and were adjustable. A  $1/4''$  gap was left between the mirrors for safety during mounting, adjustment, and installation. The mirrors in the arrays were all aligned, with respect to each other, using a laser and a surveying mirror. Each array was mounted in the counter shell at three points and was aligned with the laser and surveying mirror mounted at the primary focus.

The 26 cm by 60 cm plane mirrors reflect light to virtual foci at the center of the PMTs' face. The mirrors are  $1/4''$  plate glass bonded to  $1/4''$  aluminum plates with 738 RTV. They were each mounted at three points in the Čerenkov shell and aligned together with the ellipsoidal mirrors.

The collecting cones are compound parabolic concentrators (CPC) or Winston cones<sup>50</sup> with a 22.2 cm diameter entrance, a 12.1 cm diameter exit, a length of 20.3 cm, and a cutoff angle of  $30^\circ$ . These four parameters completely determine

the geometry of the CPC. The CPC is a surface of revolution generated by a section of a parabola and is defined by the following parametric equations

$$r = 6 \sin\left(\frac{\phi - \frac{\pi}{6}}{1 - \cos \phi}\right) - 2$$

$$z = 6 \cos\left(\frac{\phi - \frac{\pi}{6}}{1 - \cos \phi}\right) .$$

Figure 3.9 shows the CPC used. The particular size of the cone was determined by the available space, by the requirement that the PMT be at least one shielding diameter into the magnetic shield, and by the size of the PMT. The cones were made of epoxy by spin casting on an aluminum mandrel with a polished surface. A gelcoat layer was applied to prepare the inner surface for the aluminization process. LEDs were mounted on each of the cones for use in calibration.

The  $MgF_2$  coating will cause destructive interference for light reflecting at glancing angles. This only occurs in the Winston cones so they did not receive a  $MgF_2$  coating.

To enhance collection efficiency in the UV part of the spectrum, a layer of p-terphenyl was applied to the photomultiplier faces. The p-terphenyl absorbs strongly in the UV and re-emits at wavelengths near the peak of the PMT quantum efficiency<sup>51</sup>. Figure 3.10 shows the improvement of the quantum efficiency for a PMT in the UV part of the spectrum.

The final design of the PMT assembly is shown in figure 3.9. It consists of an RCA 8854 5" diameter quanticon surrounded by four concentric magnetic shields: two mu-metal shields, 6.75" diameter by 10" length and 7.63" diameter by 16" length; and a double layer soft iron shield of 8.25" diameter and 23.5" length with

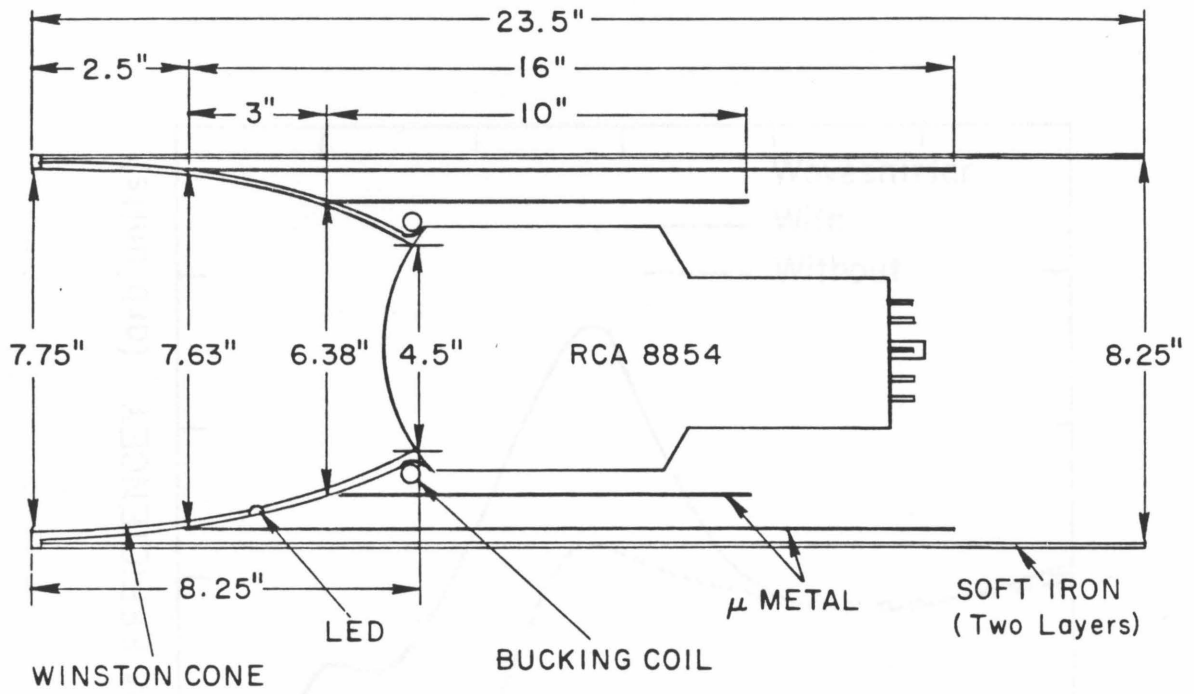


Fig. 3.9 Cross section of Čerenkov PMT assembly.

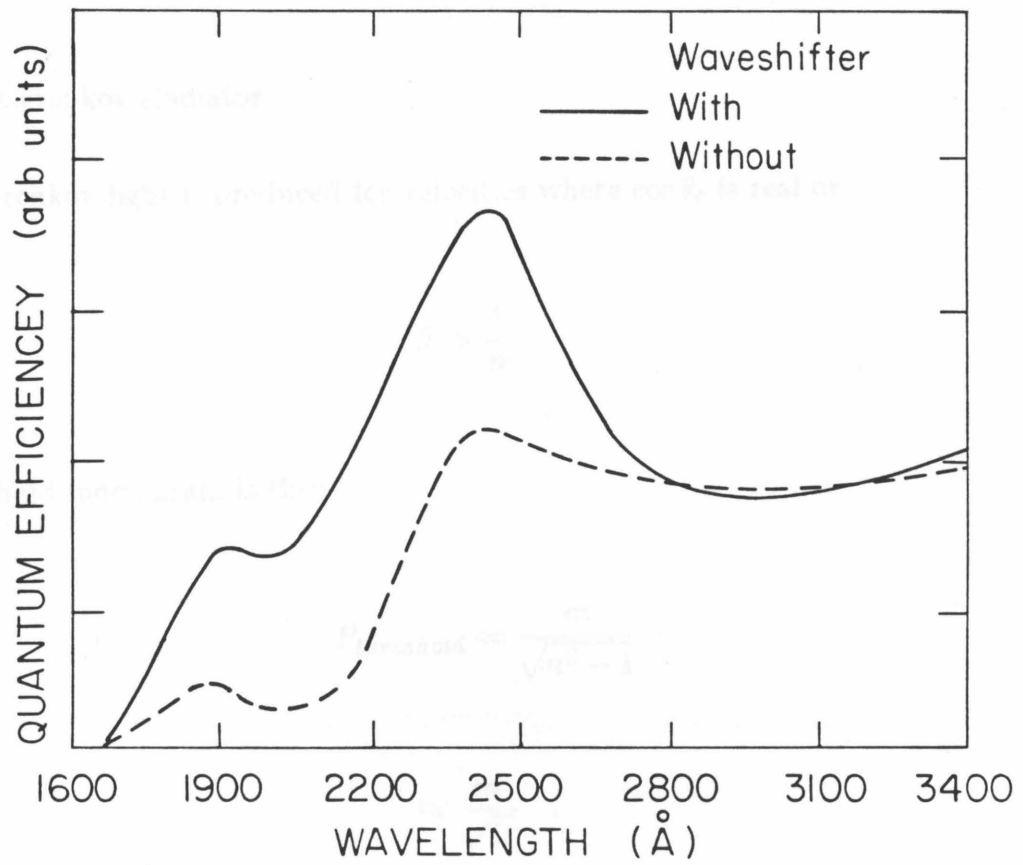


Fig. 3.10 PMT response with p-terphenyl wave shifter. Comparison of RCA 8854 response with and without waveshifter.

a .125" gap. The PMT photocathode is 8.25" from the front of the shield assembly. The fringe field of the DELCO magnet varies from 50 to 150 gauss outside of the PMT shields. At the photocathode the radial component of the magnetic field is about 0.2 gauss, and the axial component is about 1.0 gauss. A 50 turn bucking coil (BC) eliminates the axial component of the field. The BC currents are adjusted to give the maximum response to light signals from LEDs mounted on the CPCs.

### 3.4.4 Čerenkov Radiator

Čerenkov light is produced for velocities where  $\cos \theta_c$  is real or

$$\beta > \frac{1}{n} .$$

Threshold momentum is then

$$P_{threshold} = \frac{m}{\sqrt{n^2 - 1}}$$

$$\approx \frac{m}{\sqrt{2\epsilon}} .$$

The maximum value of  $\epsilon$  is determined by the momentum range over which electrons are to be tagged. In DELCO this is about 2.5 Gev/c since the outer shower counters are designed to separate electrons from minimum ionizing particles above this value. This corresponds to  $\epsilon$  of  $1.5 \cdot 10^{-3}$ , which is close to the value for isobutane ( $1.44 \cdot 10^{-3}$ ). For  $\pi - K$  separation it is desirable to have  $\pi$  threshold as low as possible since the hadron momentum spectrum peaks below 1 Gev/c.

**Table 3.4 Properties of Čerenkov Radiators.**

gas	$\epsilon \cdot 10^3$	$\chi_0, (10^{-3})$	$\lambda_{cutoff}, (\text{Å})$
$N_2$	.295	2.6	1400
$CO_2$	.450	3.9	1920
$CH_4$	.441	1.2	1640
$C_2H_6$	.720	2.4	1850
<i>iso</i> - $C_4H_{10}$	1.44	4.6	1960

Refractive index,  $\chi_0$  in the Čerenkov counter, and lower wavelength cut-off for Čerenkov radiators.

**Table 3.5 Particle Thresholds, (Gev/c), in Čerenkov Radiators.**

gas	$e^\pm$	$\mu^\pm$	$\pi^\pm$	$K^\pm$	$p^\pm$
$N_2$	.020	4.2	5.6	20.0	38.0
$CO_2$	.016	3.4	4.5	16.0	30.0
$CH_4$	.017	3.5	4.6	16.0	31.0
$C_2H_6$	.0132	2.7	3.6	12.8	24.2
<i>iso</i> - $C_4H_{10}$	.0098	2.0	2.7	9.4	17.9

The refractive index<sup>52</sup>, lower wavelength cut-off<sup>53</sup>, and density for several Čerenkov radiators are shown in table 3.4. Momentum thresholds for various particles are shown for these radiators in table 3.5. The refractive index dispersion<sup>54</sup> is shown in figure 3.11 for several gases and is relatively constant over the transmitted part of the Čerenkov spectrum. The lower wavelength cutoff determines  $N_0$  and is sensitive to contaminants such as water and oxygen which absorb strongly in the UV part of the spectrum. A recirculating system is used to purify the 500 cubic feet of isobutane required to fill the counter. Purification is accomplished with a DEOXO catalyst, which forms water with residual  $O_2$  and a

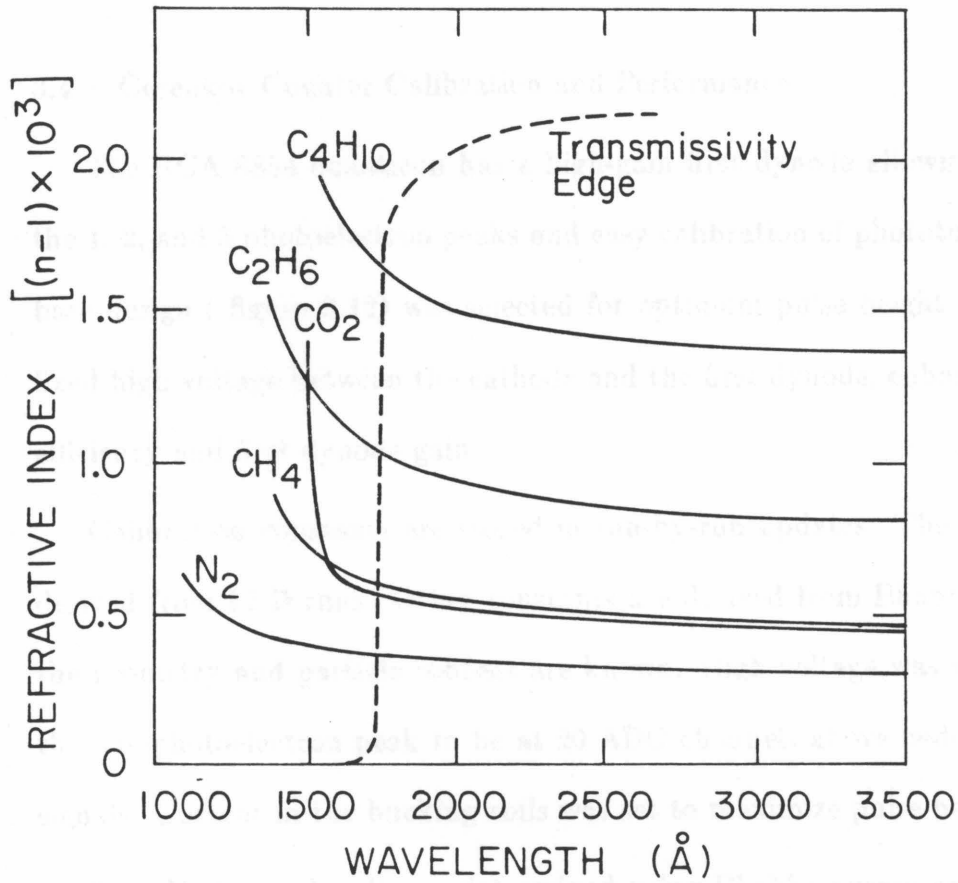


Fig. 3.11 Refractive index dispersion for gases

small amount of  $H_2$  ( $< 1\%$ ) that is injected into the system. The  $H_2O$  is removed by filtering through a molecular sieve. The recirculation is  $100 \text{ ft}^3/\text{hr}$  at a positive pressure of  $.25''$  of  $H_2O$  which is maintained by injection of  $1 \text{ ft}^3/\text{hr}$  of isobutane. Average  $H_2O$  and  $O_2$  levels are 20 ppm and are continuously monitored with a hygrometer and an oxygen analyzer.

### 3.4.5 Čerenkov Counter Calibration and Performance

The RCA 8854 quanticon has a high-gain first dynode allowing resolution of the 1, 2, and 3 photoelectron peaks and easy calibration of phototube gain. The base design ( figure 3.12) was selected for optimum pulse height resolution with fixed high voltage between the cathode and the first dynode, enhancing collection efficiency and first dynode gain.

Calibration constants are stored in run-by-run updates. The PMT gains are derived from LED runs. Other constants are derived from Bhabha events where the geometry and particle content are known. High voltage was set by requiring the one-photoelectron peak to be at 20 ADC channels above pedestal using LED signals. Current in the bucking coils was set to maximize pulse height.

The  $N_0$  for each cell was determined using Bhabha events and the following conditions:

1. Hit well within mirror boundaries.
2. Hit away from vertical plane.
3.  $\beta = 1$  and no curvature.
4. Index of refraction for isobutane is 1.00144 .
5. Index of refraction for nitrogen is 1.000295 .

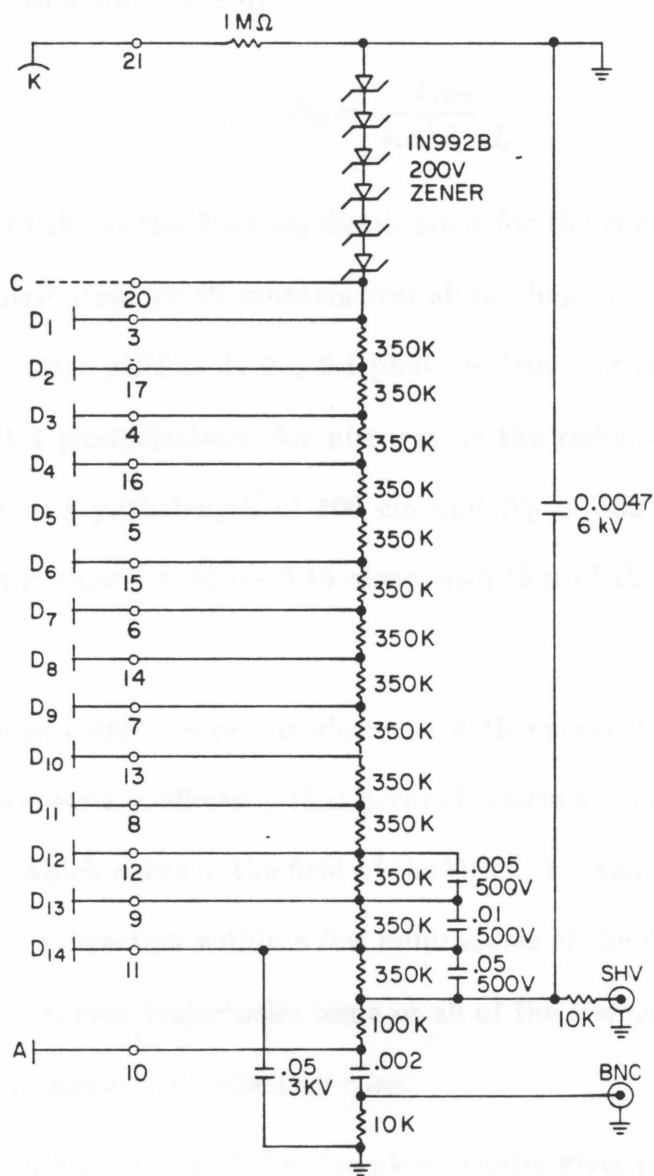


Fig. 3.12 PMT base diagram

The  $N_0$  for each cell was determined from the raw photoelectron yield of electrons in Bhabha events by

$$N_0 = \frac{P_{raw}}{\sin^2 \theta_c \cdot L} .$$

Figure 3.13 shows the final  $N_0$  distribution for the counter. The raw photoelectron distribution for all counters over all run blocks is shown in figure 3.14 and gives the average yield of  $17.9 \pm 0.1$  photoelectrons for isobutane as the radiator and  $4.8 \pm 1.4$  photoelectrons for nitrogen as the radiator. The distribution, normalized to a path length of 100 cm and  $N_0$  of  $100 \text{ cm}^{-1}$ , as a function of momentum is shown in figure 3.15 along with that of the simulated Monte Carlo response.

The pulse height drops for electrons with energy below 500 Mev. This is due to a geometric inefficiency that occurs because low momentum particles have trajectories which curve in the field of the DELCO magnet. Čerenkov radiation is generated in a direction within a few milliradians of the direction of the radiating particle. For curved trajectories some or all of the Čerenkov light will not fall on a PMT or an associated collecting cone.

The elliptic geometry of the Čerenkov counter gives isochronous signals for all trajectories that follow the optics since all Čerenkoving particles have beta equal to one. The method of timing is such that the mean time for beam-beam events will be zero. The time is derived as

$$T = T_{raw} - T_{offset} - \frac{C}{\sqrt{P_{raw}}} .$$

$T_{raw}$  is the raw signal time,  $T_{offset}$  is the time pedestal,  $C$  is a slew parameter

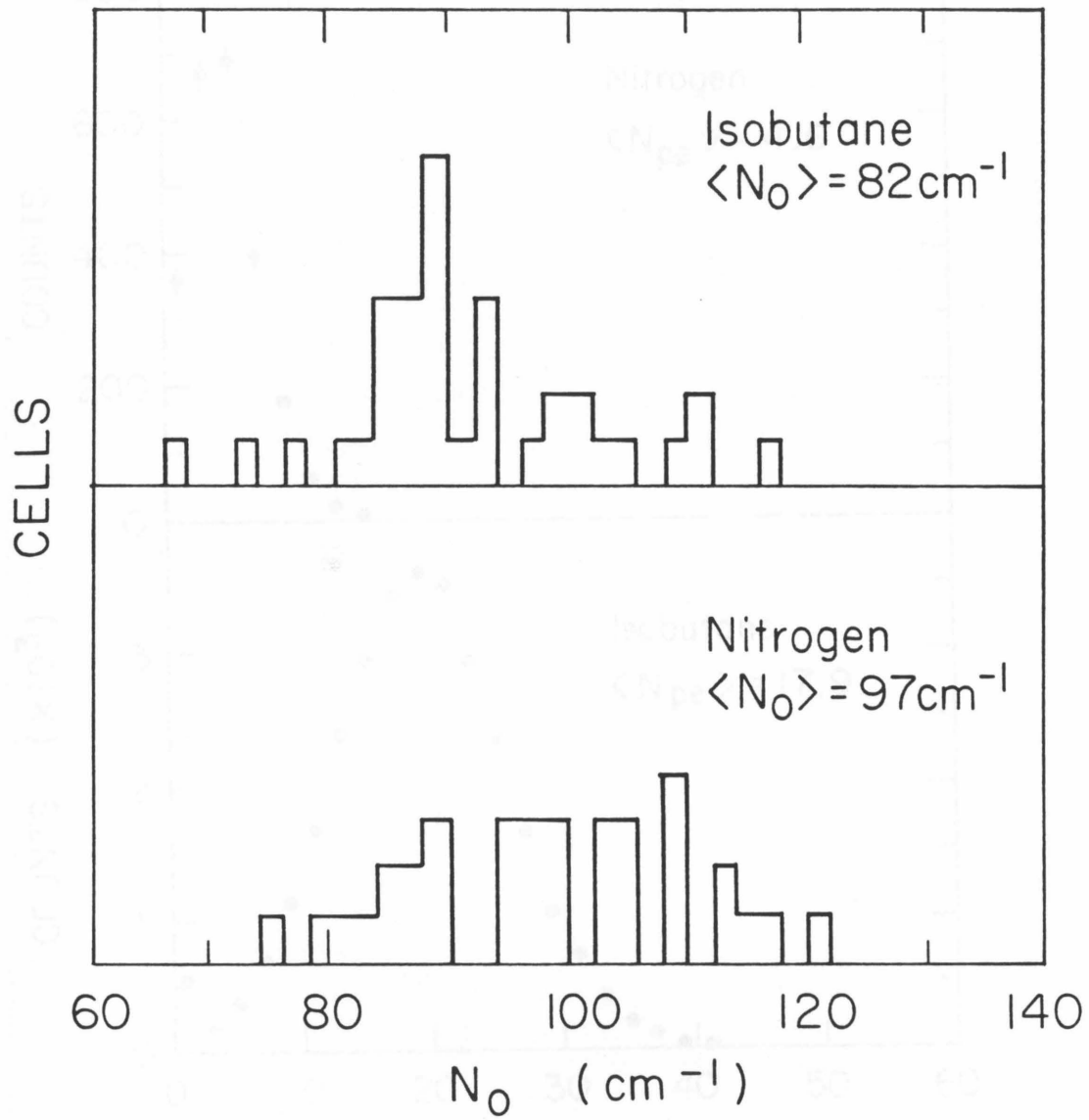


Fig. 3.13  $N_0$  distribution of Čerenkov counter

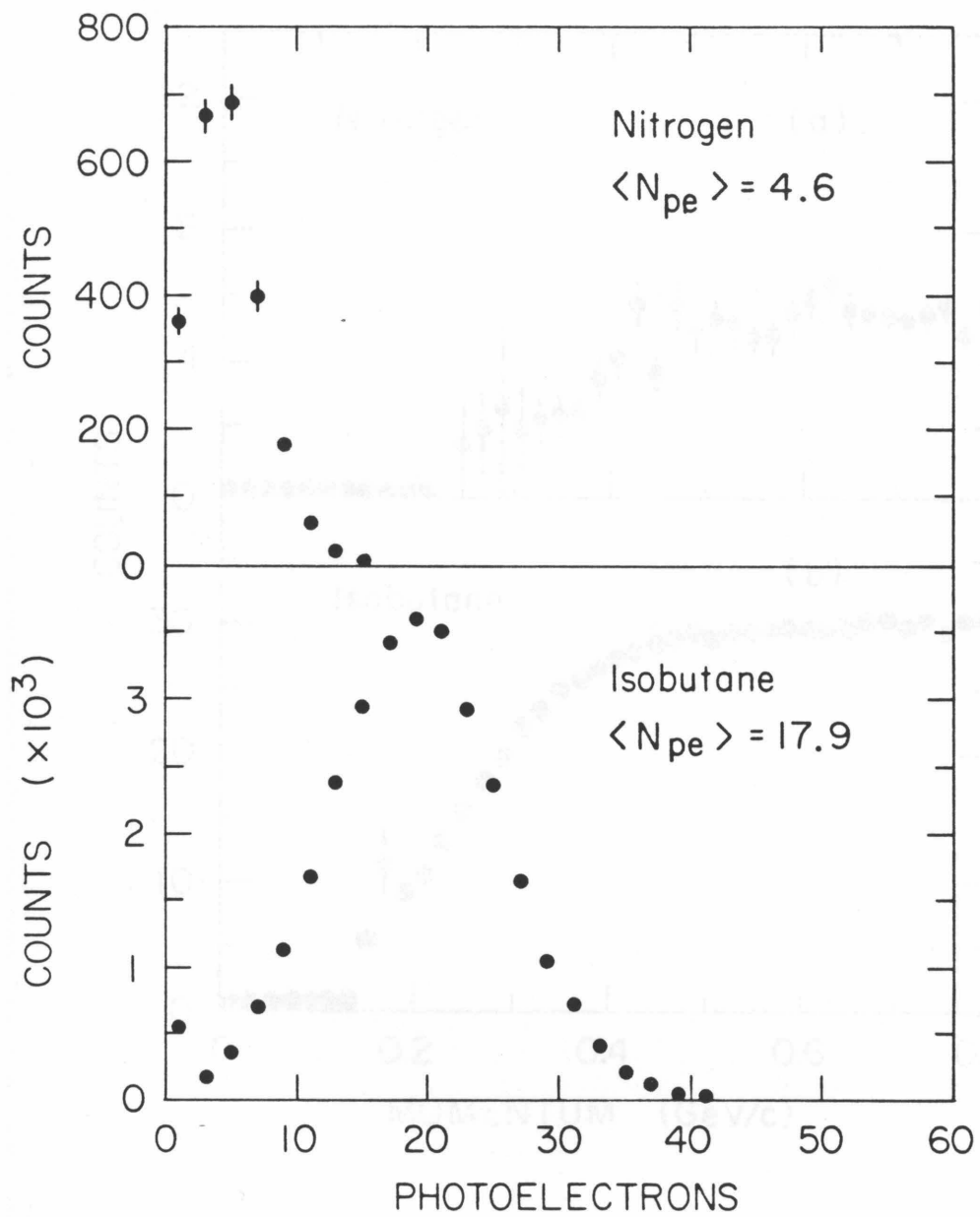


Fig. 3.14 Raw photoelectron yield for isobutane and nitrogen

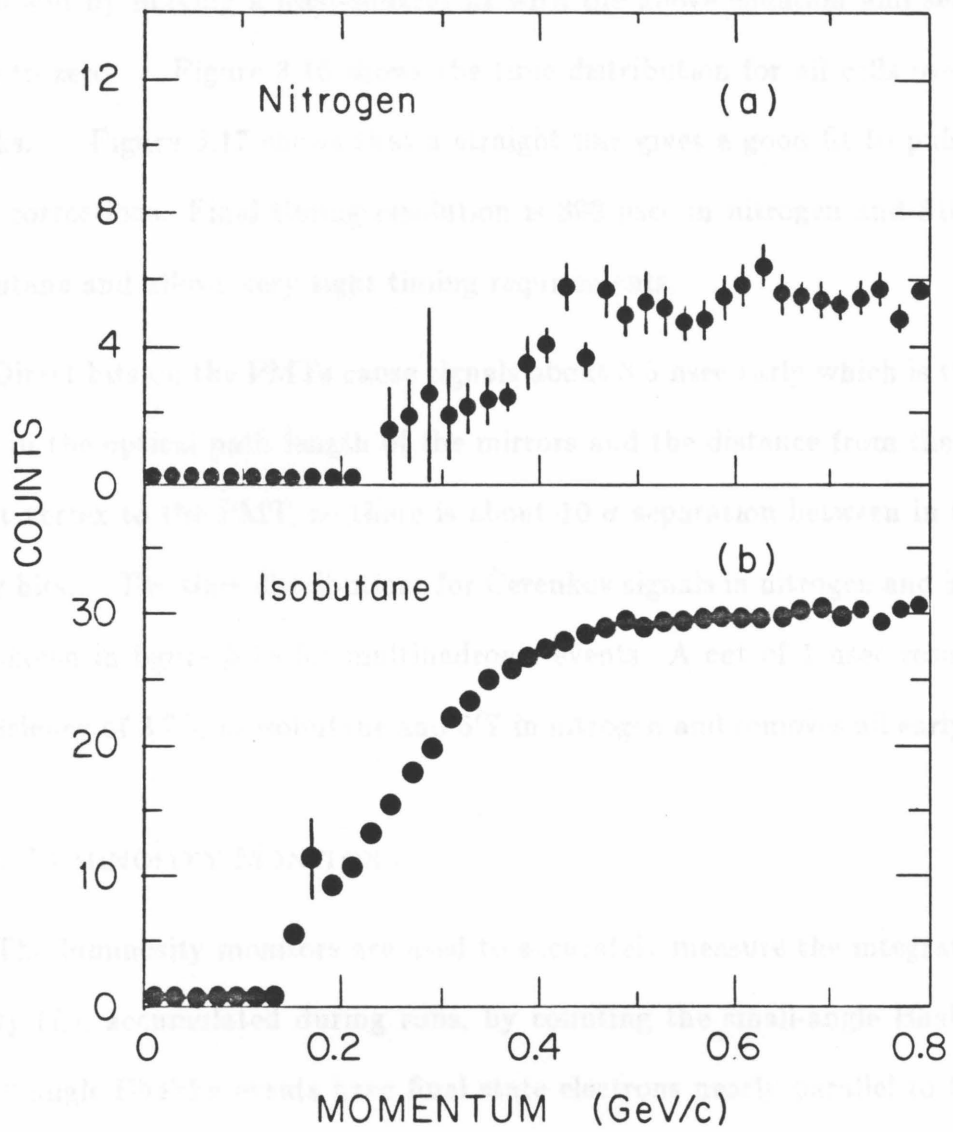


Fig. 3.15 Photoelectron yield vs. momentum. Response is  $\langle N_{pe} \rangle$  normalized to 1 meter path length.

constant, and  $P_{raw}$  is the pulse height in ADC channels. The offset and slew are found by making a least-squares fit with the above equation and setting the time to zero. Figure 3.16 shows the time distribution for all cells over all run blocks. Figure 3.17 shows that a straight line gives a good fit to pulse height slew corrections. Final timing resolution is 390 psec in nitrogen and 310 psec in isobutane and allows very tight timing requirements.

Direct hits on the PMTs cause signals about 3.5 nsec early which is the difference in the optical path length of the mirrors and the distance from the primary event vertex to the PMT, so there is about  $10 \sigma$  separation between in time and early hits. The time distributions for Čerenkov signals in nitrogen and isobutane are shown in figure 3.18 for multihadronic events. A cut of 1 nsec results in an inefficiency of 3.7% in isobutane and 5% in nitrogen and removes all early signals.

### § 3.5 LUMINOSITY MONITORS

The luminosity monitors are used to accurately measure the integrated luminosity ( $\mathcal{L}$ ), accumulated during runs, by counting the small-angle Bhabha rate. Small-angle Bhabha events have final state electrons nearly parallel to the beam axis. The electrons are back-to-back, energetic, and produced at a high rate. They are an ideal means of monitoring event rates for determining cross sections.

The monitor covers the solid angle from 26.7 to 80.8 mrad from the beam axis. There are six counters, arranged hexagonally around the beam pipe, on each side of the interaction point. Each counter is composed of a set of Pb-scintillator counters (L counters), which measure electromagnetic energy deposited by Bhabha electrons, and a scintillator face counter (F counter) which tags those electrons that

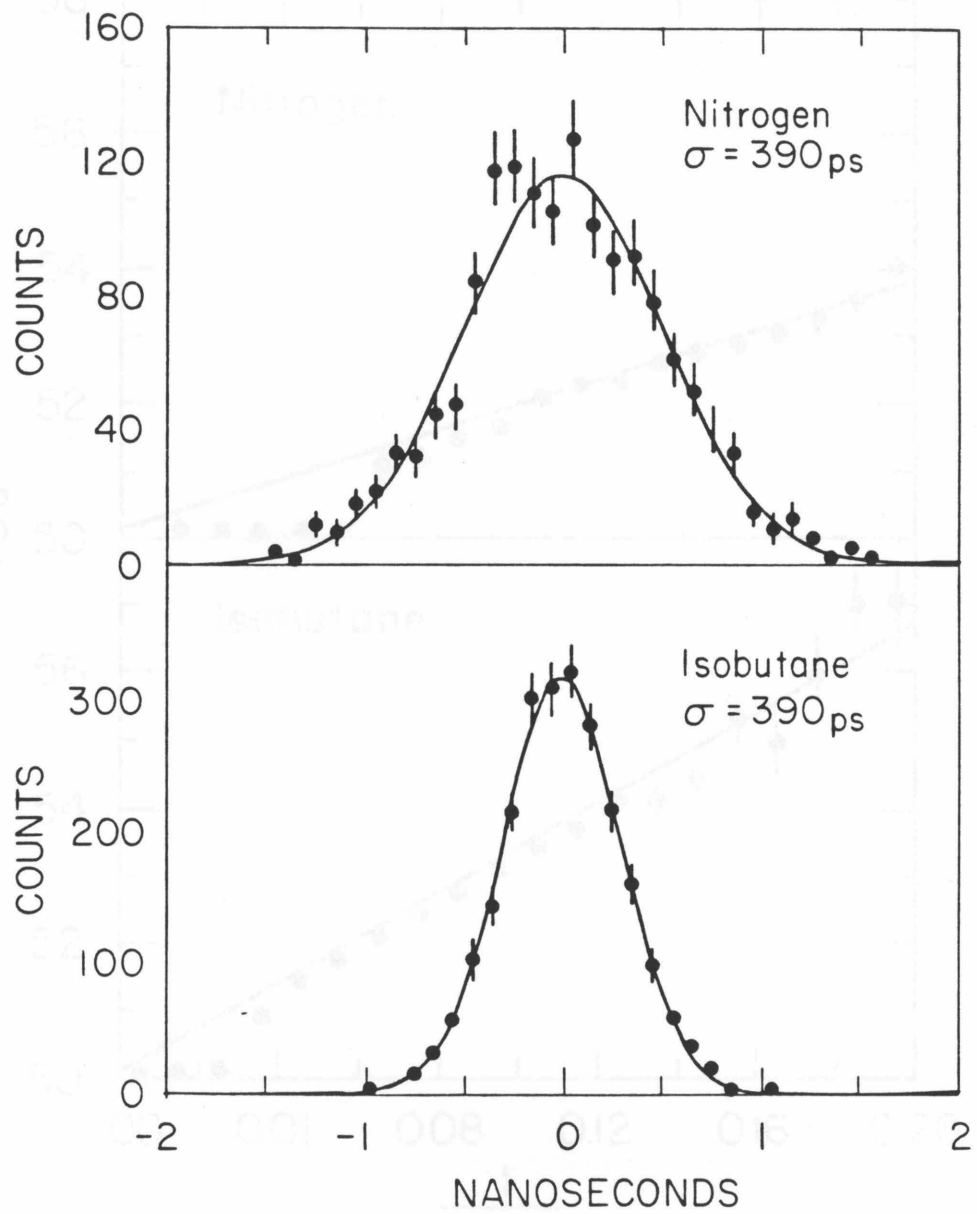


Fig. 3.16 Čerenkov counter time distribution.

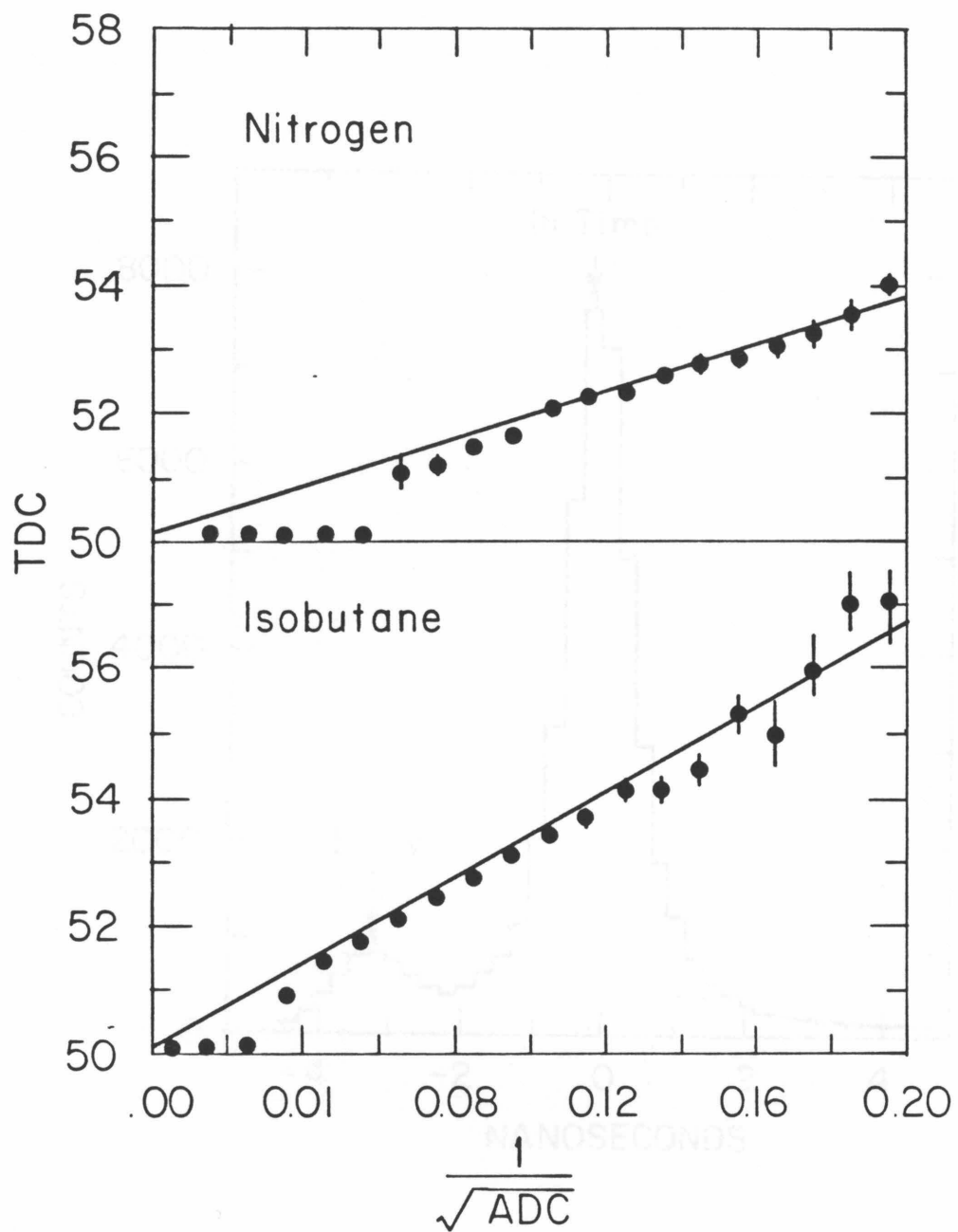


Fig. 3.17 Čerenkov counter pulse height timing slew.

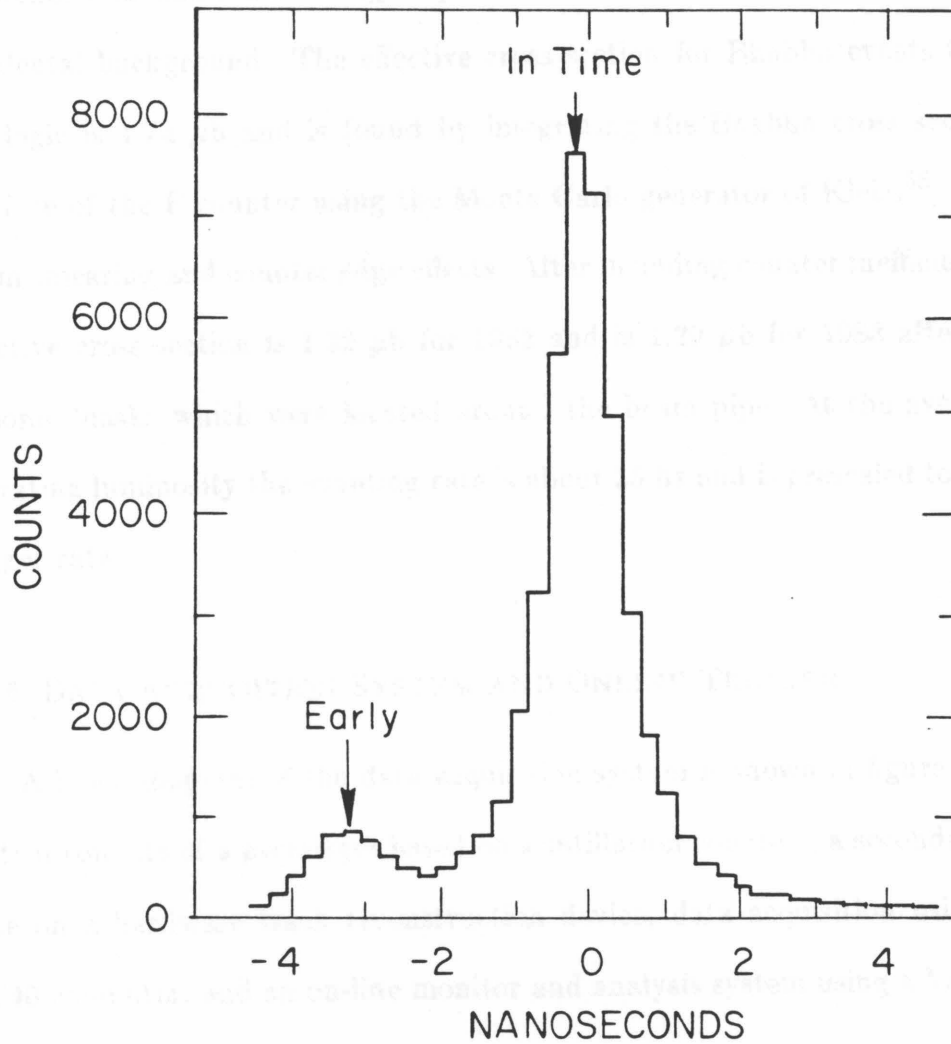


Fig. 3.18 Čerenkov times in multihadron events. *Early signals are due to direct PMT hits.*

enter the monitor over a definite solid angle.

To find small-angle Bhabhas, the trigger logic requires back-to-back F and L latches and minimum energy deposited in each counter. There is very little accidental background. The effective cross section for Bhabha events to trigger the logic is  $1.74 \mu\text{b}$  and is found by integrating the Bhabha cross section over the face of the F counter using the Monte Carlo generator of Kleiss<sup>55</sup> including beam smearing and counter edge effects. After including counter inefficiencies, the effective cross section is  $1.22 \mu\text{b}$  for 1982 and is  $1.29 \mu\text{b}$  for 1983 after removal of some masks which were located around the beam pipe. At the average PEP operating luminosity the counting rate is about 25 hz and is prescaled to lower the trigger rate.

### § 3.6 DATA ACQUISITION SYSTEM AND ONLINE TRIGGER

A block diagram of the data acquisition system is shown in figure 3.19. The system consists of a pretrigger based on scintillation counters, a secondary trigger base on a hardware track reconstruction device, data acquisition using a PDP 11/40 computer, and an on-line monitor and analysis system using a VAX 11/780 computer, which also logs data to tape.

The detector is divided into four systems defined by the type of readout electronics they employ. There is a separate system for each of the drift chamber (IDC, CDC, and PDC) using CAMAC modules characterized by an unknown number of words per event, and one system that includes the Čerenkov and shower counters using standard CAMAC ADCs, TDCs, and latches. The detector systems can be read separately by LSI-11 computers for diagnostic checks. For each detector sys-

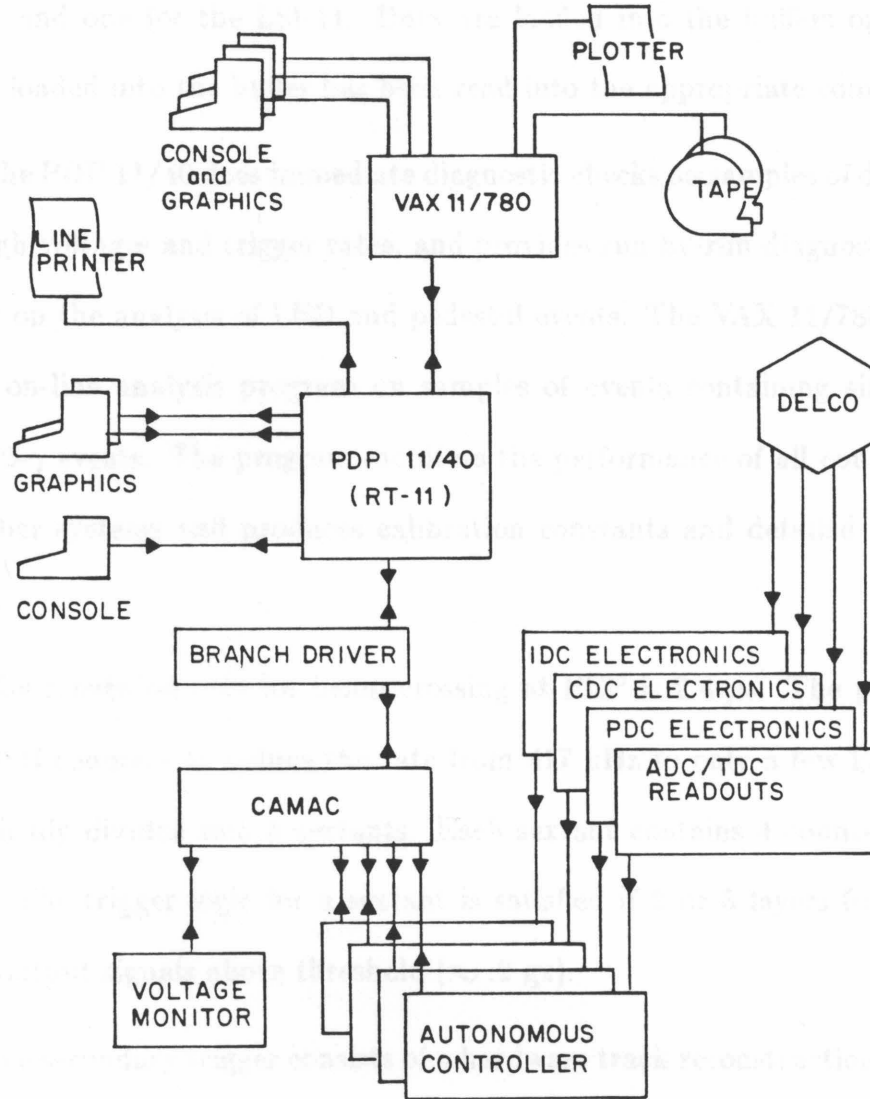


Fig. 3.19 Data acquisition system block diagram.

tem, an autonomous controller reads data out of the interface modules and packs them into two CAMAC buffer memories, one for the CAMAC system of the PDP 11/40 and one for the LSI-11. Data are loaded into the buffers only if the last event loaded into the buffer has been read into the appropriate computer.

The PDP 11/40 does immediate diagnostic checks on samples of data, monitors all high voltages and trigger rates, and provides run-by-run diagnostic summaries based on the analysis of LED and pedestal events. The VAX 11/780 runs a complete on-line analysis program on samples of events containing single electrons from 2- $\gamma$  events. The program monitors the performance of all counter and drift chamber systems and produces calibration constants and detailed diagnostic reports.

The repetition rate for beam crossing at PEP is 2.4  $\mu$ s. The pretrigger uses the BSH counters to reduce the rate from 417 kHz to only a few kHz. The BSH is logically divided into 6 sextants. Each sextant contains 4 counters of 3 layers each. The trigger logic for a sextant is satisfied if 2 or 3 layers for any counter have output signals above threshold ( $\approx .2$  gx).

The secondary trigger consists of a hardware track reconstruction device which forms coincidences of BSH counter signals with particle trajectories. The device has been described in detail elsewhere<sup>56</sup> and will be described only briefly here. Tracks are reconstructed based on signals from adjacent wires in separate layers of the central drift chambers. The BSH counters are included as a logical layer in the device, and a counter is on if 2 or 3 layers have signals above threshold. The trigger logic can be adjusted for the number of tracks and the number of hits on tracks. There are four different trigger types for events with tracks; these are

called charged triggers. Other triggers depend only on counter latches and pulse heights and are called neutral triggers. The charged triggers are:

1. X2S - at least 2 BSH sextants and a track including an s counter (S-track).
2. XKS - at least one Čerenkov counter and an S-track.
3. XPS - at least one PSC hit and an S-track.
4. XLS - at least one L counter and an S-track.

The neutral triggers are:

1. X - beam crossing (prescaled rate).
2. X2SG - at least 2 BSH counters and minimum energy deposited.
3. XPBB - hits in PSC counters on opposite sides of beam crossing point (prescaled).
4. XLBB - hits in L counters on opposite sides of beam crossing point (prescaled).

For typical luminosities of  $1.6 \times 10^{31} \text{cm}^{-2} \text{sec}^{-1}$  the charged trigger rate is about 1 Hz, the neutral trigger rate is about 0.7 Hz, and the experimental dead-time is about 1%. Multihadron and Bhabha events almost always satisfy more than one trigger requirement (X2S, XKS, and X2SG) so that cross checks of efficiency can be done. Efficiencies for these events are  $>99\%$  if they are within the geometric acceptance of the detector.

### § 3.7 MONTE CARLO SIMULATION OF DETECTOR

Proper simulation of the detector response to Monte Carlo events is necessary in order to understand the effect of cuts on the data and in order to interpret the results. Simulation of the detector begins by entering initial state particles from

a Monte Carlo generated event into a software routine. The routine contains the origin, momentum cosines, particle type, and charge of each particle. Decaying particles, such as  $\pi^0$ 's and  $K^0$ 's, decay according to their decay time constants. Interacting particles, such as  $\gamma$ 's, decay according to their interaction probability and the total mass they traverse.

Final state neutral particles are projected through the detector, losing energy in the massive regions according to standard methods of determining energy loss. The response is simulated for neutral particles only in the shower counters. The response for electromagnetic showers is calculated from a universal shower curve and is described in section 2.4.2 along with the description of the response for minimum ionizing particles.

The final state charged particles are swum through the detector along trajectories that depend on the magnetic field traversed and on multiple scattering and energy loss in the massive regions. The magnetic field map, all region geometries, and the appropriate materials are included in the simulation. The drift chamber wire hits are determined for the cells that are traversed by charged particles with hit times smeared by a resolution determined from the data. The resolution includes effects of the clock (4 nsec bin width  $\approx 50 \mu\text{m}$ ) and uncertainties in drift velocity, field shape in the cells, and drift chamber positions.

There is a simulated Čerenkov counter response if the particle has momentum above Čerenkov threshold. Čerenkov light is generated according to equation (3.1).  $N_0$  is determined as described in section 2.5.5, and the path length in the counter and  $\sin \theta_c$  are determined from the trajectory, momentum, and mass of the particle. Geometric effects of track curvature and mirror edges are included

by empirically measuring them with single electrons found in  $2\text{-}\gamma$  events. Cross talk for light that falls on mirror edges is included by sharing the light between cells by the proportion of light falling on the mirror in each cell.

Extreme care has been taken to include all known characteristics of the detector. All survey numbers and component dimensions have been measured to well within the detector resolution corresponding to them. To accurately mimic the real data, all counter responses are determined individually according to the calibration constants found for each. The calibration constants are run-dependent to reflect changes from run to run such as timing shifts and changes in the Čerenkov counter and drift chamber gases.

## § 3.8 MONTE CARLO EVENT GENERATION

### 3.8.1 The Lund Monte Carlo

A Monte Carlo program based on the Lund model for jet fragmentation<sup>57</sup> is used for simulating multihadron events produced in  $e^+e^-$  annihilation. Fragmentation of quarks into jets is described as the breakup of a color flux tube extending between the quark-antiquark pair. Gluon fragmentation is implemented by a kink in the flux tube. This scheme has been described extensively by Sjöstrand<sup>58</sup>. The Lund model was selected because it agrees well with the data for properties of multihadron events such as flavor production and jet configurations. Annihilation events are of the type,

$$\begin{aligned} e^+e^- \rightarrow \gamma/Z^0 \rightarrow q\bar{q} \\ \rightarrow q\bar{q}g \end{aligned}$$

using QED with weak interactions included according to the standard theory<sup>59</sup>

Radiative corrections, due to initial state photon bremsstrahlung, are significant and are described in a later section. Quark flavors are produced, during fragmentation, in the ratio of  $u : d : s : c : b = 3 : 3 : 1 : 0 : 0$ , and the ratio of pseudoscalar to vector mesons produced in hadronization is set to 1 : 1 to agree with experimental results<sup>60</sup>.

### 3.8.2 Jet Fragmentation and Particle Decays

The fragmentation for light quarks follows the standard Lund fragmentation form given as

$$D(z) = (1 + a_q)(1 - z)^{a_q} \quad ,$$

where  $z$  is the fractional longitudinal energy of the hadron in the jet. This function is almost flat for  $c$  and  $b$  mesons which should have harder fragmentation forms<sup>20</sup> as described in Chapter 1. For these quarks the following form, suggested by Peterson et al.<sup>23</sup> and based on kinematical considerations is used

$$D(z) = \frac{1}{z(1 - \frac{1}{z} - \frac{\epsilon}{1-z})^2} \quad .$$

The Lund fragmentation scheme uses

$$z = \frac{(E + p_{||})_{hadron}}{(E + p_{||})_{quark}} \quad ,$$

and the experimentally observed quantity is usually  $E_{hadron}/E_{beam}$ , so photon and gluon bremsstrahlung must be taken into account. To do this,  $D(z)$  is defined to include the effects of gluon bremsstrahlung and is taken before initial state photon bremsstrahlung occurs.

The semileptonic decays of heavy,  $c$  and  $b$  flavored mesons occur via a  $V - A$  decay matrix in order to reproduce the proper energy spectrum of the leptons. The distributions from these decays are checked by comparing the results from SPEAR for  $c$ -meson decays<sup>16,18</sup> and CESR for  $b$ -meson decays<sup>12,37,38</sup> with Monte Carlo events generated at the appropriate energy. The results of this check are shown in figure 3.20 where the momentum spectra of prompt electrons produced in the Monte Carlo are compared with the spectra of electrons produced at the  $\psi$  resonance at SPEAR and at the  $\Upsilon$  resonance at CESR.

Finally, the branching ratios of all decaying particles produced in the fragmentation are the currently most acceptable values.

To check the Monte Carlo, comparisons with the data are made for distributions that are important for the analysis of the prompt electrons. Figure 3.21 shows the distributions for  $x = p/E_{beam}$  and  $p_{\perp}^2$  as measured in the data and including the Monte Carlo results.

### 3.8.3 Radiative Corrections

Initial state photon bremsstrahlung radiation is introduced into the Lund Monte Carlo following the prescription of Berends and Kleiss<sup>61</sup>. The efficiency of the hadron selection algorithm is a function of the maximum photon energy cutoff,  $k_{max}$ . Corrections due to the photon energy cutoff at  $k_{max}$  are computed according to

$$\sigma(k < k_{max}) = \sigma_0(s) \left[ 1 + \delta - \frac{\beta}{2} \log\left(1 - \frac{k_{max}}{E}\right) - \frac{\beta k_{max}}{2E} \right] \left(\frac{k_{max}}{E}\right)^\beta \dots \quad (3.2)$$

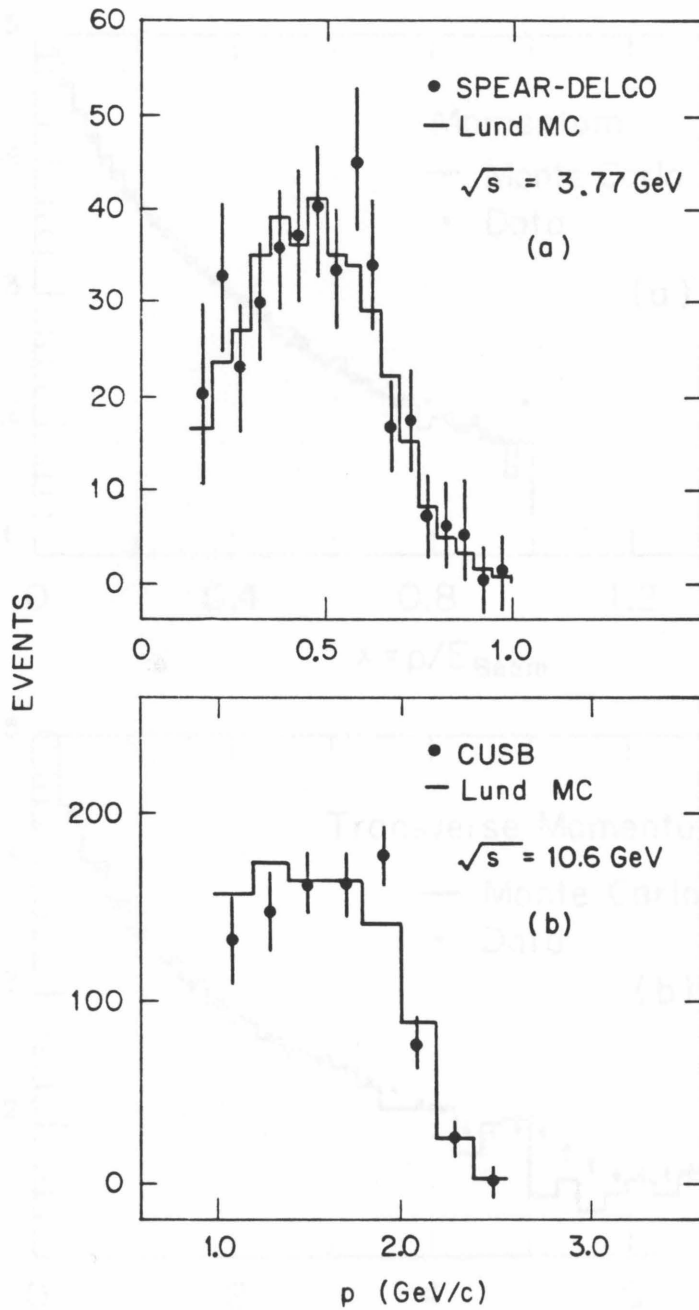


Fig. 3.20 Monte Carlo  $e$  spectrum at  $\psi$  and  $\Upsilon$ . (a) SPEAR-DELCO measurement at 3.77 GeV. (b) CUSB measurement at 10.6 GeV at CESR.

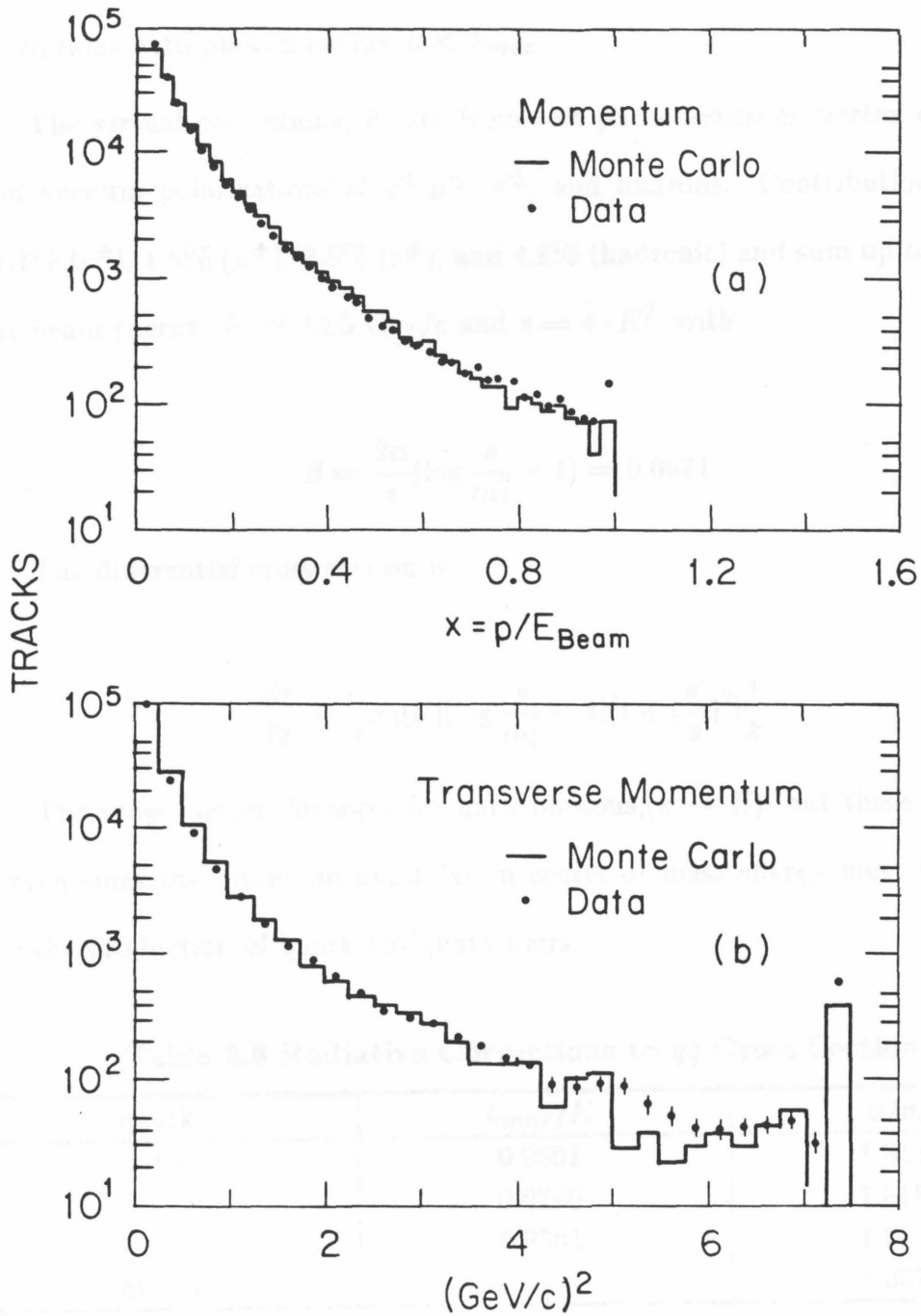


Fig. 3.21 Monte Carlo distributions. (a)  $x = p/E_{\text{beam}}$ . (b)  $p_{\perp}^2$ .

This is the  $0^{th}$  order cross section without initial photon plus higher order QED corrections with photon energy  $k < k_{max}$ .

The virtual corrections,  $\delta$ , are from soft photo-emission, vertex corrections, and vacuum polarizations of  $e^\pm, \mu^\pm, \tau^\pm$ , and hadrons. Contributions to  $\delta$  are 11.1% ( $e^\pm$ ), 1.5% ( $\mu^\pm$ ), 0.5% ( $\tau^\pm$ ), and 4.8% (hadronic) and sum up to 17.9% for the beam energy,  $E$ , of 14.5 Gev/c and  $s = 4 \cdot E^2$ , with

$$\beta = \frac{2\alpha}{\pi} \left( \log \frac{s}{m_e^2} - 1 \right) = 0.0971 \quad .$$

The differential cross section is

$$\frac{d\sigma}{dk} = \frac{\alpha}{\pi} \sigma_0(s') \left( \log \frac{s}{m_e^2} - 1 \right) \left[ 1 + \left( \frac{s'}{s} \right)^2 \right] \frac{1}{k} \quad .$$

The cross section diverges for hard photons, ( $k \rightarrow E$ ), but these are not observed since the minimum annihilation center of mass energy must be sufficient for the production of quark-antiquark pairs.

**Table 3.6 Radiative Corrections to  $q\bar{q}$  Cross Sections.**

quark	$k_{max}/E$	$\sigma/\sigma_0$
u,d,s	0.9801	1.3185
c	0.9790	1.3159
b	0.8561	1.2127
average		1.3079

For light quarks the cutoff is chosen to be .9801 . For  $c\bar{c}$  and  $b\bar{b}$  production the cutoff is .9790 and .8561. The cutoff values were chosen to leave sufficient phase space for meson production. The resultant corrections to the total cross section are

1.3185, 1.3159, and 1.2127 for light quark-antiquark,  $c\bar{c}$ , and  $b\bar{b}$  pair production. These are found by event rate production of the Lund Monte Carlo generator with the given values of the cutoffs. The overall correction to the hadronic cross section is found by taking the average of the individual cross sections weighted by the square of the corresponding quark charges and is 1.3079 . The results of the  $q\bar{q}$  radiative corrections are summarized in table 3.6 .

## CHAPTER 4

# Procedure

Only multihadron events produced in the annihilation of  $e^+$  and  $e^-$  to a single virtual photon are of interest for the inclusive electron analysis. Events classified as hadrons are selected and processed through an electron finding algorithm and scanned by eye to remove backgrounds that could not be found by the software filter. The selection procedure is optimized to enhance direct electrons in the final data sample and minimize backgrounds. Very few event backgrounds, such as two photon events and  $\tau^+\tau^-$  events, are expected to contribute to the final  $e^\pm$  candidates. Most event backgrounds that are misclassified as multihadron events are easily removed in the final scan by eye.

Electron candidate tracks must have Čerenkov signals and energy deposited in the BSH counter consistent with those tracks being electrons with the same kinematical properties. The geometric acceptance is  $0.67 \cdot 4\pi$  steradians for the Čerenkov counter and  $0.61 \cdot 4\pi$  steradians for the BSH counter, giving an overall acceptance of  $0.58 \cdot 4\pi$  steradians.

**Table 4.1 Particle Rates in Monte Carlo Multihadron Events.**

particle	$\nu$	$\gamma$	$e^\pm$	$\mu^\pm$	$\pi^\pm$	$e_{\pi^0}^\pm$	$K^\pm$	$K^0$	$p^\pm$
rate	0.24	12.2	0.11	0.11	9.34	0.15	1.27	0.67	1.03

*Generated particle rates from Monte Carlo multihadrons produced over  $4\pi$  steradians in  $e^+e^-$  annihilations at 14.5 Gev/c in the center of mass.*

**Table 4.2 Charged Particle Rates in DELCO.**

particle	$e(\gamma)$	$e(Dalitz)$	$e(prompt)$	non- $e$
rate	9.22	0.12	.088	8.99

*Event rate for charged particles within the geometric acceptance of DELCO for multihadron events.*

Table 4.1 shows relative rates for particles produced in multihadron events. Only charged particles entering the acceptance of the counters are of interest. The relative rates for these particles are shown in table 4.2 . The ratio of signal to noise in multihadron events is less than 1% so the filter must have at least a 100 to 1 background rejection rate to electron rejection rate.

A description of the method used to determine the integrated luminosity for the data set used is given since the luminosity is required for calculating cross sections. This chapter also includes a description of the program used to select the multihadron events and the prompt electron candidates; the procedure used to determine event rates and efficiencies; and the techniques used for determining background normalizations. Finally, a description of the data flow and the final

number of candidates is given for the analysis of the following chapter.

#### § 4.1 LUMINOSITY MEASUREMENTS

The integrated luminosity ( $\mathcal{L}$ ) is monitored by counting the small-angle Bhabha events that trigger the L counters as described in section 3.6 . The result is checked by counting the wide-angle Bhabha and  $\mu^+\mu^-$  event rate into the BSH-Čerenkov systems and the medium-angle Bhabha event rate into the PSC system.

Wide-angle Bhabha events are found by selecting events with two tracks that are back-to-back ( $\delta\phi < 0.1$  rad) and within the acceptance of the BSH counters. The total energy deposited in the counters must be greater than 30 gx to eliminate  $\mu^+\mu^-$  events, and total track energy must be greater than 5 Gev to eliminate 2- $\gamma$  events. The main background contribution is from  $\tau^+\tau^-$  events and is calculated using a  $\tau^+\tau^-$  Monte Carlo generator.

Wide-angle  $\mu^+\mu^-$  events are found with criteria similar to those used to select wide-angle Bhabha events with the exception that the BSH energy must be less than 15 Gx. Two additional cuts are used to eliminate cosmic ray muons. ToF timing cuts are used to insure that the BSH counters on opposite sides of the detector fire at the same time, and Čerenkov counter pulse heights are required since Čerenkov cells will fire in time only for particles going outward from the event vertex. As in the Bhabha events the major background is from  $\tau^+\tau^-$  events, and the contribution is determined with a  $\tau^+\tau^-$  Monte Carlo.

Medium-angle Bhabha events are selected by requiring total energy deposited in the PSC to be greater than 6 Gev with at least 2 Gev in each pole tip. The energy must be deposited in opposite counters and back-to-back within 240 mrad.

The hit position is found by taking a weighted average of the pulse heights in adjacent counters where the energy is deposited. Angular resolution of the PSC is about 100 mrad.

The background contributions are mostly from

$$e^+e^- \rightarrow \gamma\gamma$$

$$e^+e^- \rightarrow e^+e^-e^+e^- ,$$

which have final state particles at small angles. Most of these events are removed with the PSC total energy cut, and the final contribution is determined with a 2- $\gamma$  Monte Carlo.

**Table 4.3 Luminosity Measurements.**

Data	$e^+e^-_L$	$e^+e^-_{BSH}$	$\mu^+\mu^-_{BSH}$	$e^+e^-_{PSC}$	Average	$\sigma_L$
1982	1.0	1.06	1.02	—	$1.04 \pm .05$	$1.168 \mu\text{b}$
1983	1.0	1.08	1.03	1.086	$1.07 \pm .05$	$1.208 \mu\text{b}$

*Comparison of luminosity measurement methods. All methods agree within the measurement resolution. The comparisons are in terms of the L counter rate which is set to 1.0.*

Table 4.3 gives the results of the comparisons between the methods used for determining luminosity. Rates given in the table are in terms of the L counter rate which is set to 1. Contributions to systematic errors are from background normalization uncertainty and survey measurement resolution. The luminosity cross section ( $\sigma_L$ ) is the factor used to convert counting rate to luminosity. The total  $\mathcal{L}$  for the data used in this analysis is  $118 \text{ pb}^{-1}$  as determined from the luminosity counter, with  $92 \text{ pb}^{-1}$  of isobutane data and  $26 \text{ pb}^{-1}$  of nitrogen data.

## § 4.2 MULTIHADRON EVENT SELECTION

Multihadron events are selected with the following criteria:

Total number of reconstructed tracks  $> 4$ .

Total charged energy  $> 6$  Gev.

$\langle Z_{vertex} \rangle$  of all tracks must be within 4.5 cm of the beam crossing point.

At least 3 tracks with 2 or more PDC  $z$  wires hit.

The background contribution is from other multiprong events. These are  $\tau^+\tau^-$  events, 2- $\gamma$  events, and beam-gas interactions. The  $\tau^+\tau^-$  events are eliminated by removing events with less than 5 reconstructed tracks. The remaining  $\tau^+\tau^-$  rate is very small compared to the rate of multihadrons with greater than 5 tracks. The 2- $\gamma$  events are removed by requiring the candidate events to have greater than 6 Gev of charged energy, where charged energy is defined as the sum of the momenta of all reconstructed tracks. Most of the energy in 2- $\gamma$  events is carried out of the ends of the detector by high energy electrons or photons and misses the central detector. The beam-gas interactions are removed by demanding that the vertex of the tracks be constrained to within 4.5 cm of the interaction region of the beams along the beam axis. Requiring PDC hits insures that tracks in the event will be in the central detector, and momentum measurement errors for these tracks will be small.

The major source of residual background is from 2- $\gamma$  events. Figure 4.1 shows the charged energy distribution of multihadron events with the expected Monte Carlo distribution. The excess events at low energies in the data is due to 2- $\gamma$  events and is about a 5% contribution above 6 Gev. These events do not contain

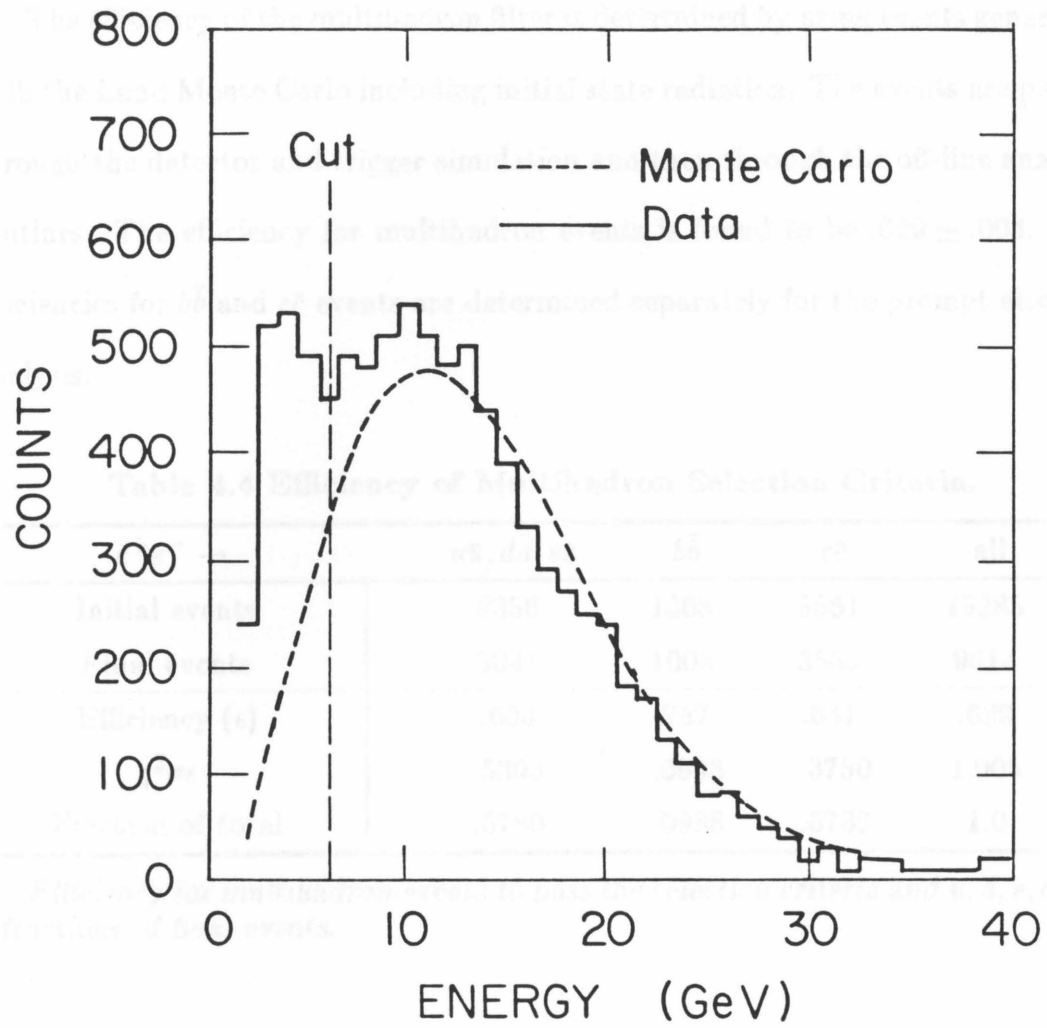


Fig. 4.1 Total energy of charged tracks in multihadron events. Abundance at low energies is due to  $2\text{-}\gamma$  background.

prompt electrons, but they do contribute to the prompt electron background.

The efficiency of the multihadron filter is determined by using events generated with the Lund Monte Carlo including initial state radiation. The events are passed through the detector and trigger simulation and then through the off-line analysis routines. The efficiency for multihadron events is found to be  $.629 \pm .004$ . The efficiencies for  $b\bar{b}$  and  $c\bar{c}$  events are determined separately for the prompt electron analysis.

**Table 4.4 Efficiency of Multihadron Selection Criteria.**

$e^+e^- \rightarrow$	$u\bar{u}, d\bar{d}, s\bar{s}$	$b\bar{b}$	$c\bar{c}$	all
Initial events	8356	1368	5561	15285
Final events	5041	1008	3565	9614
Efficiency ( $\epsilon$ )	.603	.737	.641	.629
$q^2\sigma\epsilon$	.5303	.0993	.3750	1.005
Fraction of total	.5780	.0988	.3732	1.0

*Efficiency for multihadron events to pass the selection criteria and  $u, d, s, c$  and  $b$  fractions of final events.*

The results are listed in table 4.4. The number of events is found from the efficiency ( $\epsilon$ ) and the integrated luminosity ( $\mathcal{L}$ ) as

$$N_{hadrons} = 1.3079 \cdot R \cdot \sigma_{\mu^+\mu^-} \cdot \epsilon \cdot \mathcal{L} ,$$

where 1.3079 is the radiative correction listed in table 3.6 ,  $\sigma_{\mu^+\mu^-}$  is the point cross section for  $e^+e^- \rightarrow \mu^+\mu^-$ , and  $R$  is the ratio of the hadronic cross section to the point cross section. The best value for  $R$  is  $3.91 \pm .08$  at PEP energies.<sup>62</sup>

The results for the data sets listed in table 4.5 show an excess of  $(7 \pm 5)\%$

**Table 4.5 Integrated Luminosity and Event Rates for Data Sets.**

Data set	$\mathcal{L}(\text{pb}^{-1})$	$N_{had}$ (measured)	$N_{had}$ (expected)	excess %	$N_{c\bar{c}}/\epsilon_{c\bar{c}}$	$N_{b\bar{b}}/\epsilon_{b\bar{b}}$
1982 iso	22.4	7996	7443	6.9	4333	999
1983 iso	70.1	25051	23293	7.0	13559	3126
1982 nit	26.3	9525	8739	8.3	5087	1173
Total	118.8	42572	39475	7.3	22979	5298

Number of final events in each data set and the expected final number of events. The excess,  $(1 - N_{expected}/N_{measured})$ , is due to  $2 - \gamma$  contamination.

events in the data. This is consistent with the amount of  $2 - \gamma$  background events expected. The number of expected  $b\bar{b}$  and  $c\bar{c}$  events are needed for the electron analysis and are determined by

$$N_{q\bar{q}}/\epsilon_q = \sigma/\sigma_0 \cdot q^2 \cdot \sigma_{\mu^+\mu^-} \cdot \mathcal{L} \quad ,$$

where  $q^2$  is the square of the quark charge,  $\sigma/\sigma_0$  is given in table 3.6 , and  $\epsilon_q$  is the efficiency for  $q\bar{q}$  events. These results are in table 4.5 and account for the  $2 - \gamma$  background.

### § 4.3 ELECTRON SELECTION

The extended geometry of the individual Čerenkov cells leads to a natural method of grouping tracks in jet events. The counter has limited ability to distinguish between tracks in the same cell, so all such tracks in the active region of one cell are labeled as a cluster. If a background is found in a Čerenkov cell then the associated cluster of tracks is removed from electron candidacy. The backgrounds are divided into three categories.

1. Gamma electron background. The identified track is an electron from a gamma conversion or Dalitz decay that leaves a track in the inner detector.
2. Non-electron background.
  - (a) The identified track is a hadron, such as a pion, and is coincident in the Čerenkov counter with a particle that is above Čerenkov threshold.
  - (b) The track is from a nonelectron that is above Čerenkov threshold but the tracking algorithm has reconstructed it with momentum below pion threshold.
3. Other background. These are very small compared to the other two background types and are from  $2 - \gamma$  and  $\tau^+ \tau^-$  events.

The main electron filter is an algorithm that selects electron candidates and removes identified backgrounds. A positive Čerenkov signal gives complete  $e/\pi$  separation for isolated tracks below pion threshold. However, tracks in jets are not isolated, and hadron rejection below  $\pi$  threshold is limited by the coincidence of an unseen Čerenkov radiating particle in the same counter as a charged hadron.

Momentum resolution softens the rejection near threshold but this can be improved by pulse height analysis in the Čerenkov counter. The hadron background can be further reduced by requiring that energy be deposited in the barrel shower counter consistent with that particle's being an electron. The following procedure is a summary of how  $e^\pm$  candidates are selected with an electron finding algorithm:

1. Clusters of tracks are formed according to Čerenkov counter geometry.
2. Clusters must have an in-time Čerenkov signal and the maximum momentum of all of the tracks within the cluster must be less than pion threshold.

3. Tagged gamma conversions and dalitz decays removed.
  - (a) Dalitz decays and beam pipe conversions are reconstructed and removed.
  - (b) Conversions in the IDC/CDC are tagged by missing IDC hits.
  - (c) Asymmetric conversions tagged by good tracks with RDCA  $> 3$  mm.
  - (d) Late conversions tagged by PDC stubs.
4. Non-electron backgrounds removed. There must be at least one good quality track satisfying counter requirements.
  - (a) DC hits  $> 15$ , PDC  $z$  hits  $> 2$ , RDCA  $< 3$  mm.
  - (b) Čerenkov pulse height  $> 1.75$  pe (nitrogen) , 16 pe (isobutane).
  - (c) BSH response 90% confidence limit for electrons.
5. Electron tracks are selected by maximum likelihood fit to the counter responses allowing only one electron per cluster.

#### 4.3.1 Track Clusters

A track enters the active region of a cell if Čerenkov light from an electron following the same trajectory would hit the cell's PMT within a specific time window defined by the optics. Čerenkov light from a typical electron in isobutane covers an area of about 5 cm across (1.2 cm in nitrogen) on the outer elliptic mirrors, and, since the individual cells are not optically separated, there is a possibility of one track belonging to two clusters. Clusters, as units, will be accepted if they contain a track with counter responses consistent with at least one of the tracks' being an electron.

**Table 4.6 Number of Tracks per Čerenkov Cell in Multihadron Events**

Tracks per cell	0	1	2	3	4	$\geq 5$
Rate per event	26.1	6.9	2.0	.66	.197	.070

*Average occupancy of Čerenkov cells in multihadron events found in the data.*

**Table 4.7 Track Cluster Distribution in Multihadron Events.**

Clusters	0	1	2	3	4	$\geq 5$
Rate	.38	.30	.19	.089	.033	.013

*Probability for n clusters with an in-time Čerenkov signal in a multihadron event.*

The number of tracks per cluster are given in table 4.6 and the number of clusters per event are given in table 4.7 for multihadron events.

### 4.3.2 Čerenkov Counter Timing

The elliptic geometry of the Čerenkov counter gives isochronous signals for all trajectories that follow the optics, since all Čerenkoving particles have beta equal to one. Direct hits on the PMTs cause signals about 3.5 nsec early which is the difference in the optical path length of the mirrors and the distance from the primary event vertex to the PMT. The time resolution of the Čerenkov counter is about 310 psec in isobutane and 390 psec in nitrogen so there is about  $10 \sigma$  separation between in-time and early hits. A good cluster must have an in-time signal so the early hits cause an inefficiency. The time distributions for Čerenkov

signals in nitrogen and isobutane are shown in figure 3.18 for all clusters with a TDC latch. A cut of 1 nsec results in an inefficiency of 3.7% in isobutane and 5% in nitrogen. The inefficiency was found by dividing the clusters associated with early times by the total number of clusters.

#### 4.3.3 Momentum Upper Limit

Pulse height analysis can extend the  $e/\pi$  separation in the Čerenkov counter to only a few hundred Mev/c above  $\pi$  threshold, compensating the momentum resolution error. The Čerenkov counter pion thresholds are shown in figure 4.2 for isobutane and nitrogen. The percent of isolated tracks in multihadron events with Čerenkov counter pulse heights greater than 3 pe is shown versus inverse momentum. Clusters containing any tracks with momentum greater than 2.5 Gev/c in isobutane and 5.5 Gev/c in nitrogen are removed.

#### 4.3.4 Gamma Electron Removal

Several methods are used for removing clusters containing these backgrounds. Gamma conversions and Dalitz decays are found by reconstructing the decay or conversion with an algorithm that fits tracks to a vertex. A pair of tracks is called a conversion if they pass the following requirements:

1. Total charge of both tracks is 0.
2. Opening angle at the beam vertex  $< .6$  radians, to improve search time.
3. At least 1 associated Čerenkov latch.
4. Invariant mass requirement:
  - (a) 2 dimensional  $-30 \text{ Mev} < m_{inv} < 80 \text{ Mev}$  or

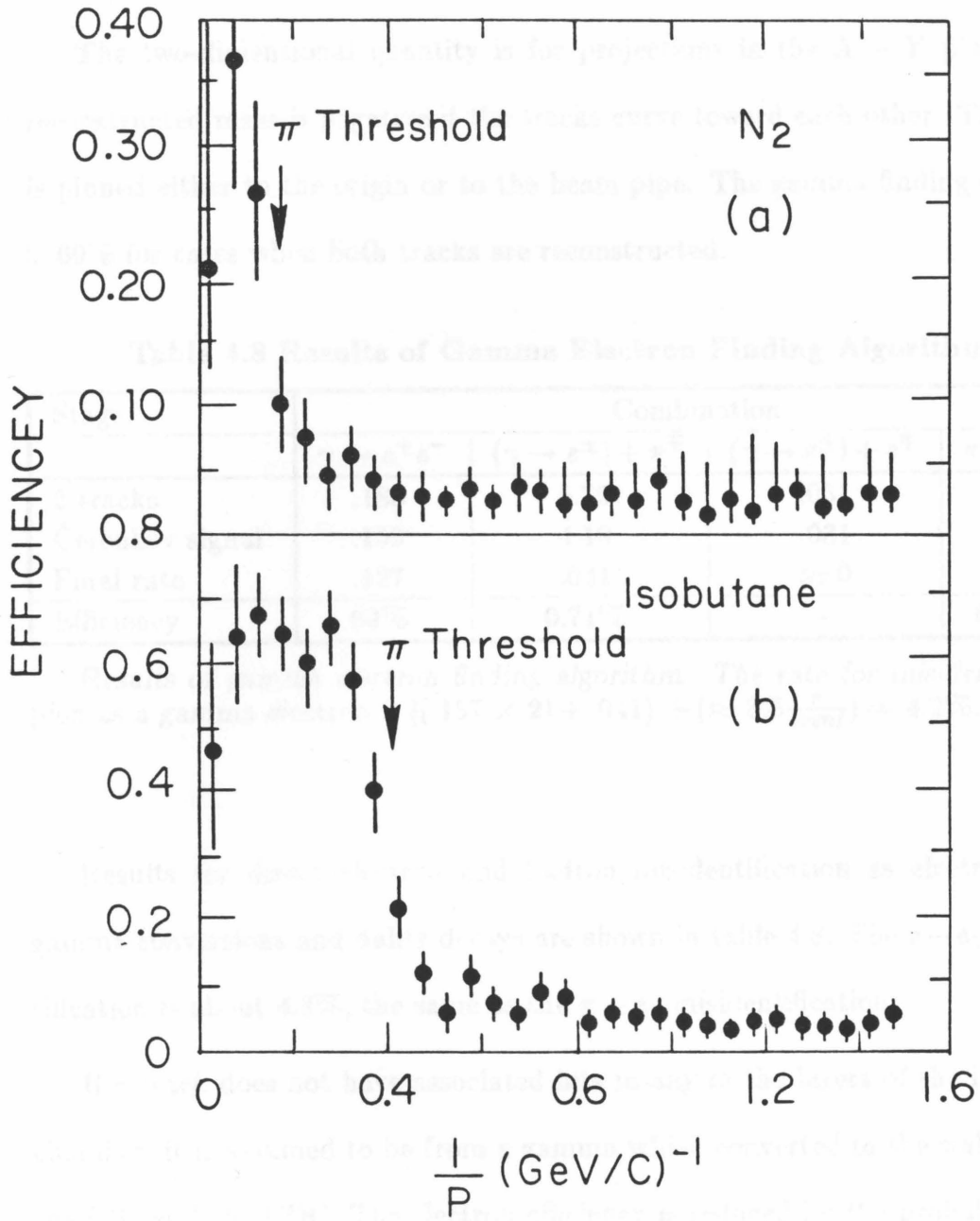


Fig. 4.2 Čerenkov pion thresholds in isobutane and nitrogen Percent of isolated tracks in multihadron events which fire counter.

(b) 3 dimensional  $-200 \text{ Mev} < m_{inv} < 300 \text{ Mev}$

The two-dimensional quantity is for projections in the  $X - Y$  plane. The reconstructed mass is negative if the tracks curve toward each other. The vertex is pinned either to the origin or to the beam pipe. The gamma finding efficiency is 69% for cases when both tracks are reconstructed.

**Table 4.8 Results of Gamma Electron Finding Algorithm.**

Stage	Combination			
	$\gamma \rightarrow e^+e^-$	$(\gamma \rightarrow e^\pm) + \pi^\mp$	$(\gamma \rightarrow e^\pm) + e^\mp$	$\pi^+ + \pi^-$
2 tracks	.183	5.79	.031	56.6
Čerenkov signal	.159	4.19	.031	19.8
Final rate	.127	.041	$\approx 0$	.157
Efficiency	69%	0.71%	-	0.28%

*Results of gamma electron finding algorithm. The rate for misidentifying a pion as a gamma electron is  $((.157 \times 2) + .041) \div (\approx 8.5 \frac{\pi}{event}) = 4.2\%$ .*

Results for direct electron and hadron misidentification as electrons from gamma conversions and dalitz decays are shown in table 4.8. The  $e - e_\gamma$  misidentification is about 4.2%, the same as the  $\pi - e_\gamma$  misidentification.

If a track does not have associated hits in any of the layers of the inner drift chamber, it is assumed to be from a gamma which converted in the wall between the IDC and the CDC. The electron efficiency is reduced by the probability that it shares a cluster with a track missing IDC hits. This cut removes 5% of the clusters in hadronic events.

Gamma conversions and dalitz decays where one or more tracks were not recognized in the pattern recognition routines are easy to identify and remove by a visual scan of the candidates. These are usually asymmetric conversions where

one track has very low momentum in the region where the tracking algorithm is inefficient. Figure 4.3 is a display of a multihadron event with an asymmetric gamma conversion that occurred near the beam pipe.

#### 4.3.5 Non-electron Removal

Late conversions are defined as gammas that convert outside the inner tracking volume of the detector. The resulting electrons leave stubs in the PDC if they are within the Čerenkov counter acceptance. Any cluster is killed if a stub is found behind the associated Čerenkov cell. A sample of 13068 clusters had 1169 clusters with stubs behind them and no Čerenkov signal, giving a 8.9% inefficiency for this cut. A strong correlation of .66 exists for a Čerenkov counter having a good in-time signal and a stub being present. The correlation is found by counting how often the Čerenkov fires when a stub is present and how often it fires when stubs are absent. Tracks are associated with stubs 5% of the time because of track reconstruction using multiple hits in the PDC and splash back from interactions in the barrel shower counter system.

A few events were observed to have continuous banks of Čerenkov cells lit up with many stubs present. This is expected if a gamma converted near the limiting edge of the inner Čerenkov window. There is a probability that a photon in this region will shower in the edge of the Čerenkov counters aluminum envelope or in the top edge of the pole tip shower counter. These are labeled as gamma-splashes and there is a 2% geometric acceptance for this to occur. Any cluster that has an adjacent cell with an in-time signal and no associated track with it is removed. 97.8% of all the clusters in the hadronic data pass this cut. The region where

RUN 4094 CYC 51 EVT 6213  
X - Y PROJ

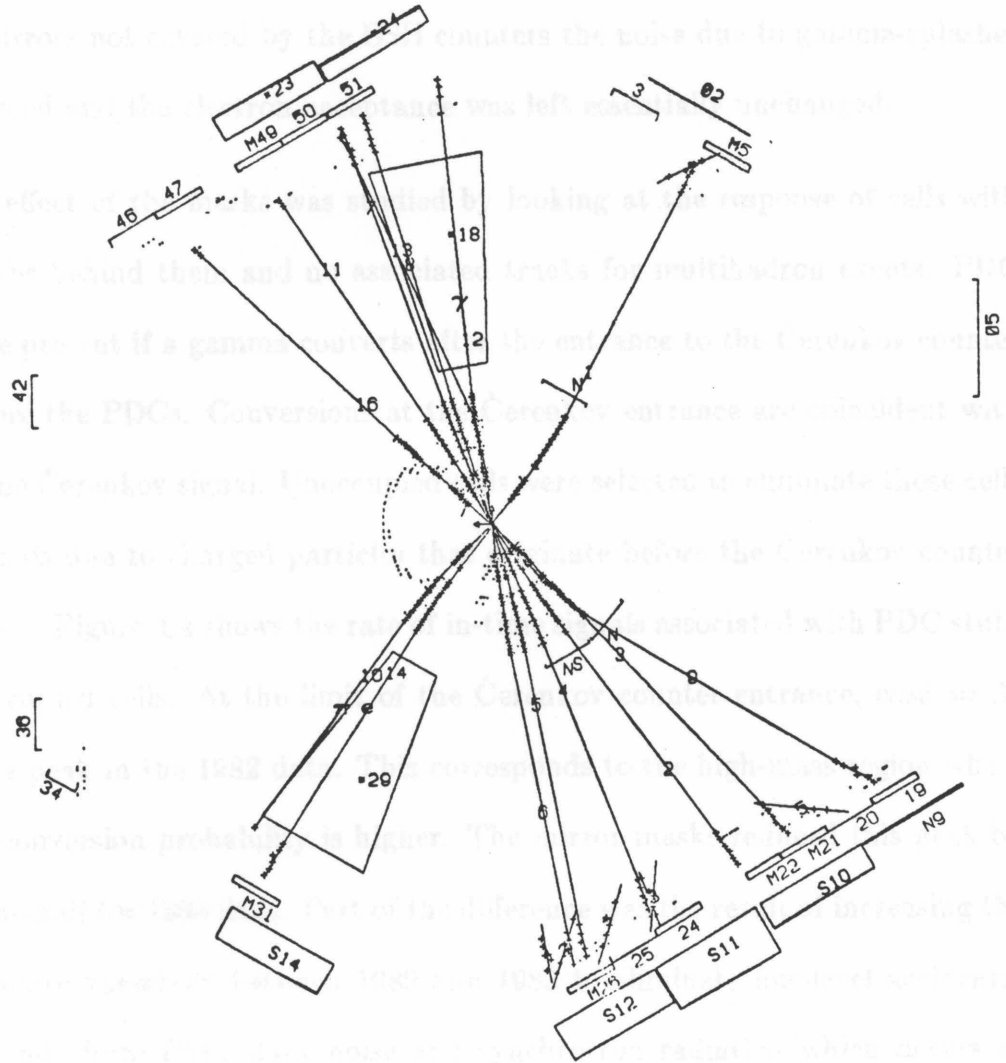


Fig. 4.3 Multihadron event with asymmetric gamma conversion.

the gamma-splashes occur can be seen in figure 3.7. The problem was solved by masking the edges of the outer Čerenkov mirrors during the summer of 1982. The BSH acceptance is less than that of the Čerenkov counter. By masking the region of the mirrors not covered by the BSH counters the noise due to gamma-splashes was reduced and the electron acceptance was left essentially unchanged.

The effect of the masks was studied by looking at the response of cells with PDC stubs behind them and no associated tracks for multihadron events. PDC stubs are present if a gamma converts after the entrance to the Čerenkov counter and before the PDCs. Conversions at the Čerenkov entrance are coincident with an in-time Čerenkov signal. Unoccupied cells were selected to eliminate those cells with signals due to charged particles that originate before the Čerenkov counter entrance. Figure 4.4 shows the rate of in-time signals associated with PDC stubs for unoccupied cells. At the limit of the Čerenkov counter entrance,  $\cos\theta = .7$ , there is a peak in the 1982 data. This corresponds to the high-mass region where gamma conversion probability is higher. The mirror masks reduced this peak by about one-half for 1983 data. Part of the difference was the result of increasing the discriminator threshold between 1982 and 1983 to eliminate low-level accidental backgrounds from PMT dark noise and synchrotron radiation which occurs at the 1 pe level. Above 5 photoelectrons the overall rate was reduced by 1.4. If we assume that the noise rate in empty cells is proportional to the rate in track associated cells, then the overall reduction in noise between 1982 and 1983 was 0.5, and the reduction of noise signals above 5 photoelectrons was about 0.714 .

The tracks in each cluster are checked to see if any has counter responses consistent with its being an electron. Any cluster that has no electron type track is

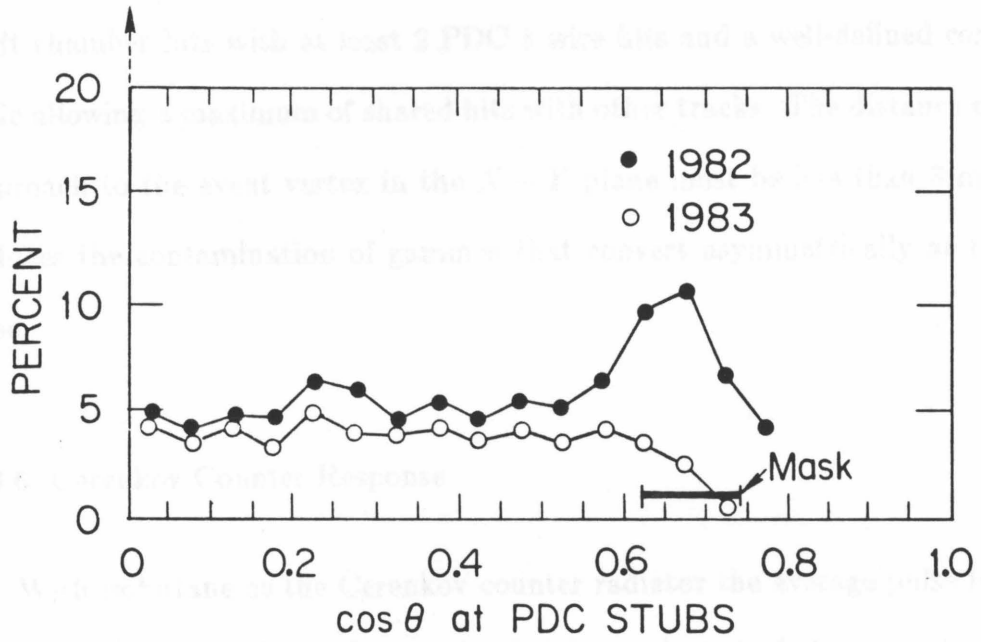


Fig. 4.4 Čerenkov noise rate vs.  $\cos \theta$  of PDC stubs.

rejected. The criteria used for  $e^\pm$  tagging are proper pulse height response in the Čerenkov counter and total barrel shower system after correcting for track parameters such as radiator path length, curvature, momentum, scintillator attenuation length, and response of individual counter segments. Track quality cuts assure that the predicted counter responses are accurate. Tracks must have at least 15 drift chamber hits with at least 2 PDC  $z$  wire hits and a well-defined completion code allowing a maximum of shared hits with other tracks. The distance of closest approach to the event vertex in the  $X - Y$  plane must be less than 3 mm. This reduces the contamination of gammas that convert asymmetrically at the beam pipe.

#### 4.3.6 Čerenkov Counter Response

With isobutane as the Čerenkov counter radiator the average pulse height for electrons is 18 pe. This allows pulse height analysis to help separate electrons from nonelectron backgrounds. Electron consistency is determined by calculating the difference between the measured response for each track and the response that would be expected for an electron with identical track parameters. The expected mean response is found by swimming through the detector an electron with the initial direction and momentum of the candidate track, and simulating the raw photoelectron yield in the particular cell. The deviation is calculated using Poisson statistics. The overall mean pulse height for electrons is 18 photoelectrons, so the average sigma/mean is about 24%, and momentum measurement errors, about 6%, are not considered. A track must have a Čerenkov pulse height within the 90% confidence limit to qualify as an electron candidate.

Using nitrogen as the Čerenkov radiator gives an average response of 5 *pe*. Pulse height analysis is not practical, and the counter is used in a threshold mode. A minimum pulse height of 1.75 *pe* is required for electron candidates. This is the minimum pulse height that still excludes the 1 photoelectron background due to synchrotron radiation, PMT dark noise, and other low-level backgrounds. Figure 4.5 shows the Čerenkov pulse height in nitrogen including low-level noise.

#### 4.3.7 Barrel Shower Counter Response

The expected pulse height is found from a universal shower curve. Corrections are made for track momentum and direction, incident angle, attenuation length of the counter, and response of the PMT which saturates at high pulse heights. Figure 3.5 shows the resultant distribution for single electrons as a function of electron energy. Resolution as a function of pulse height was also determined from the counter response to single electron events. The geometric acceptance of the shower counter is 75% of the Čerenkov counter acceptance, partly because of gaps in the vertical plane parallel to the beam axis and partly because it is shorter. The BSH requirement for electron candidates is set at the 95% confidence limit. This cut has no effect on tracks with associated momenta below 500 Mev/c where there is no distinction between electrons and minimum ionizing particles.

#### 4.3.8 Electron Selection

Figure 4.6 is a scatterplot of Čerenkov counter pulse height vs. shower counter pulse height for electrons in terms of the  $\sigma$  variables for all tracks in multihadron events in isobutane. The scatterplot for nitrogen data is also shown in figure 4.6. The Čerenkov pulse height is in photoelectrons for nitrogen. There is a cluster of

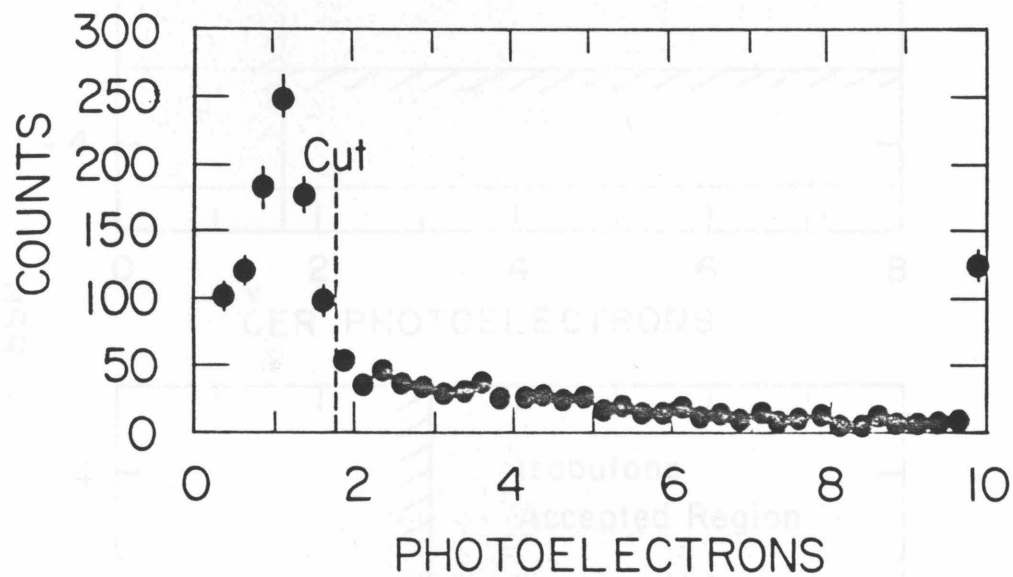


Fig. 4.5 Low level Čerenkov pulse heights

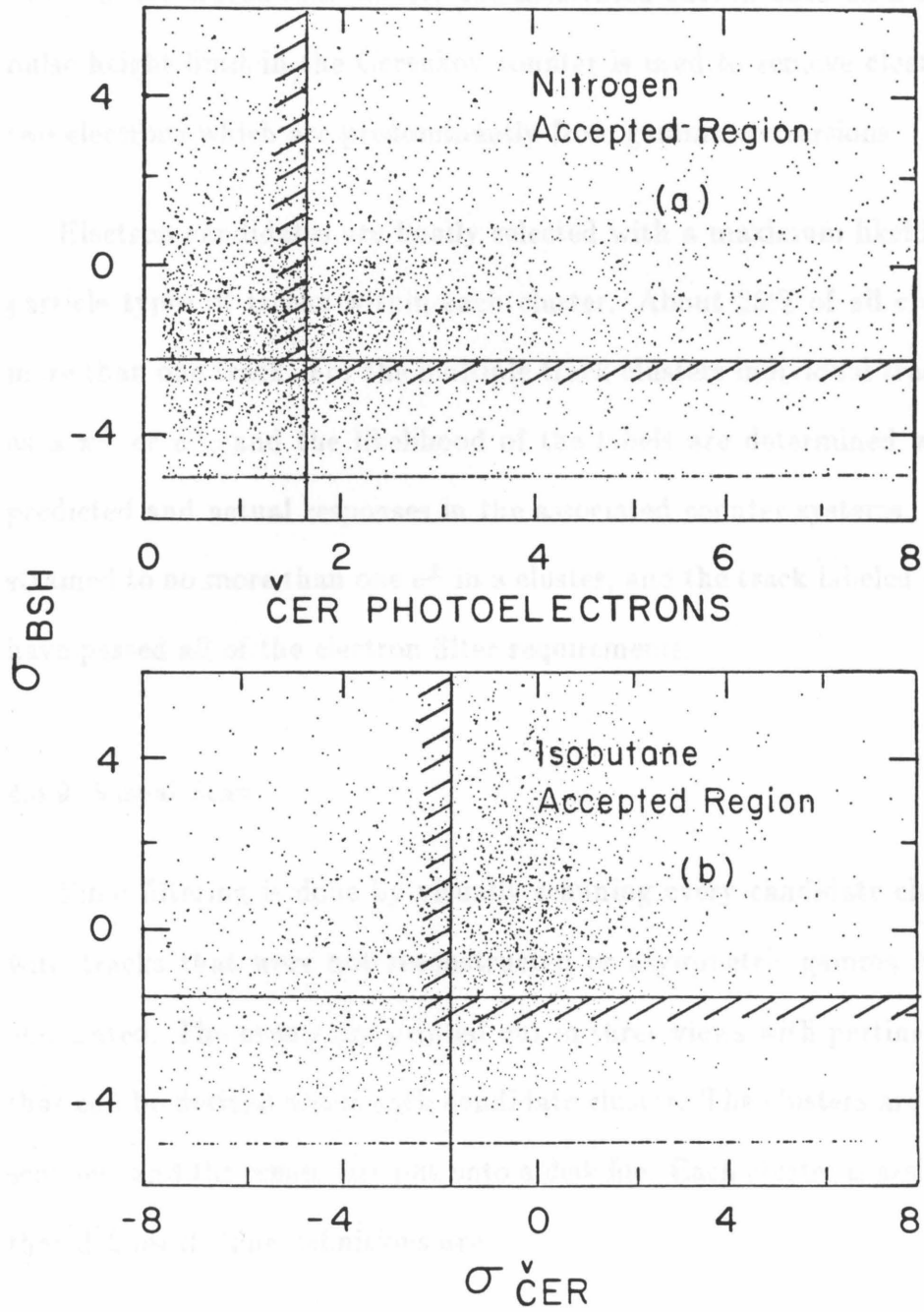


Fig. 4.6 Čerenkov vs. shower counter response for multihadrons.

electron like tracks that survive the illustrated cuts in both data sets. An upper pulse height limit in the Čerenkov counter is used to remove clusters containing two electrons which are predominantly from gamma conversions.

Electron candidates are finally selected with a maximum likelihood fit to the particle types of tracks within each cluster. About 25% of all clusters contains more than one track. For the multiple track clusters individual tracks are labeled as a  $\pi^\pm$  or  $e^\pm$ , and the likelihood of the labels are determined with respect to predicted and actual responses in the associated counter systems. The fit is constrained to no more than one  $e^\pm$  in a cluster, and the track labeled as the  $e^\pm$  must have passed all of the electron filter requirements.

#### 4.3.9 Visual Scan

Final filtering is done by visually scanning every candidate cluster. Clusters with tracks that were not reconstructed or asymmetric gamma conversions are eliminated. The events are printed out in three views with pertinent information that can be derived about each candidate cluster. The clusters are viewed by two scanners and the results are put onto a disk file. Each cluster is assigned a number that defines it. The definitions are:

1. Direct electron.
2. Gamma conversion or dalitz decay.
3. Unrecognized track.
4. Not a hadronic event.

#### § 4.4 PROMPT ELECTRON EFFICIENCY

The efficiency for prompt electrons is determined, as a function of momentum and transverse momentum, from the Monte Carlo and corrected for any differences between the Monte Carlo and the data. The differences are due to small effects of the kinematic cuts and are determined directly by measuring the survival rate for good quality tracks in both the Monte Carlo and in the data. Tracks with the following characteristics are selected:

1. Greater than 15 DC wires hits.
2.  $R_{dca}$ , (event vertex to track), less than 3 mm.
3. At least 2 PDC  $z$  wires hit.
4. Inside geometric acceptance of Čerenkov and shower counters.
5. Not identified as a background.
6. Momentum below pion threshold.

The kinematical cuts are listed in sequential order in table 4.9 with the probability that the track will survive each cut. Results are given for isobutane and nitrogen .

**Table 4.9 Efficiencies of all Kinematic and Topological Cuts.**

Filter stage	Data	MC	$\Delta_{data-mc}$
Čerenkov timing	.982	.999	-.035
$\gamma_e$ removal	.885	.888	-.003
missing IDC hits	.992	.997	-.005
$R_{dca}$ cut	.932	.960	-.030
PDC stub cut	.734	.834	-.120
Adj. empty Čerenkov	.991	.978	.013
$P < 5.5$ Gev/c	.986	.984	.002
$P < 2.5$ Gev/c	.955	.945	.011
Total Nitrogen	.576	.681	.154
Total Isobutane	.559	.653	.144

*The efficiencies for all kinematic cuts, (cuts not dependant on particle type) are given for Monte Carlo events and for the data and the difference between them.*

**Table 4.10 Efficiency for Kinematic Cuts in Isobutane for MC and Data.**

Momentum Gev/c	Transverse Momentum, (Gev)					
	0.0	0.5	1.0	1.5	2.0	
0.0	.77					mc
	.67					data
0.5	.63	.85				mc
	.53	.74				data
1.0	.49	.73	.83			mc
	.40	.61	.71			data
1.5	.44	.61	.79	.75		mc
	.34	.52	.66	.71		data
2.0	.39	.53	.67	.72	.75	mc
	.30	.45	.58	.63	.70	data

**Table 4.11 Efficiency for Kinematic Cuts in Nitrogen for MC and Data.**

Momentum (Gev/c)	Transverse Momentum, (Gev/c)					
	0.0	0.5	1.0	1.5	2.0	
0.0	.78					mc
	.68					data
0.5	.67	.85				mc
	.55	.74				data
1.0	.55	.75	.84			mc
	.44	.63	.71			data
1.5	.53	.65	.81	.76		mc
	.39	.54	.67	.71		data
2.0	.50	.59	.69	.74	.77	mc
	.37	.49	.59	.64	.70	data
2.5	.47	.56	.64	.73	.76	mc
	.38	.43	.51	.54	.66	data
3.0	.48	.55	.63	.68	.61	mc
	.37	.43	.47	.55	.61	data
3.5	.47	.51	.59	.71	.56	mc
	.38	.41	.54	.49	.63	data
4.0	.52	.56	.57	.61	.63	mc
	.40	.44	.49	.37	.60	data
4.5	.54	.54	.67	.43	.58	mc
	.35	.47	.49	.51	.64	data
5.0	.55	.55	.70	.81	.75	mc
	.41	.43	.50	.54	.60	data

**Table 4.12 Efficiency Correction Factors for Kinematic Cuts in MC.**

Data Set	Momentum (Gev/c)	Transverse Momentum, (Gev/c)				
		0.0	0.5	1.0	1.5	2.0
Isobutane	0.0	.88				
	0.5	.83	.87			
	1.0	.82	.86	.85		
	1.5	.79	.85	.85	.89	
	2.0	.77	.85	.86	.87	.91
Nitrogen	0.0	.86				
	0.5	.82	.87			
	1.0	.79	.84	.87		
	1.5	.77	.84	.86	.88	
	2.0	.76	.83	.85	.88	.88
	2.5	.77	.81	.84	.87	.88
	3.0	.79	.80	.84	.86	.88
	3.5	.79	.79	.83	.86	.88
	4.0	.79	.79	.83	.85	.88
	4.5	.78	.79	.82	.85	.88
5.0	.78	.79	.82	.84	.88	

*Ratio of electron efficiency due to kinematic cuts in data to the efficiency in Monte Carlo. Results are smoothed by hand to give reasonable distribution.*

Total efficiencies for all cuts are given in tables 4.10 and 4.11 , for  $P$  and  $P_t$ , in Monte Carlo and data. The correction factors are calculated from the efficiencies in data and Monte Carlo and are given in table 4.12. The differences between Monte Carlo and data are attributed to the cuts on early-times in the Čerenkov counter, and from the removal of clusters associated with PDC stubs. Early-times are from sources such as synchrotron radiation which is not in the Monte Carlo. The real data contain stubs from gammas that shower early in the detector, but the Monte Carlo produces only conversions into  $e^+e^-$  pairs. The conversions do not have as many stubs present as showers do, but the geometric distributions are the same. Since only one stub is sufficient for removing a cluster of tracks, the difference between Monte Carlo and data is easily corrected for. The electron efficiency is found as a function of momentum and transverse momentum by generating the reactions

$$e^+e^- \rightarrow c\bar{c} \rightarrow e^\pm X$$

$$e^+e^- \rightarrow b\bar{b} \rightarrow e^\pm X$$

using the Lund Monte Carlo with initial state radiation for the heavy quarks. The probability that an electron is identified for each  $P - P_\perp$  bin was determined using a generator with the expected relative rates for  $b \rightarrow e^\pm$ ,  $c_{primary} \rightarrow e^\pm$ , and  $c_{cascade} \rightarrow e^\pm$ .

The probability for prompt electrons and backgrounds to pass the scanning requirements is also determined from Monte Carlo.

**Table 4.13 Scanning Efficiency from Monte Carlo.**

Stage	$e(\gamma, \text{dalitz})$	$e(\text{prompt})$	non- $e$
Scanned	94	180	83
Passed	45	159	63
Efficiency	$.48 \pm .07$	$.88 \pm .08$	$.76 \pm .10$

The scanners were given Monte Carlo events to scan and the results were compared to the true answer. No momentum or transverse momentum dependence was seen. Table 4.13 shows the results of the Monte Carlo scan.

**Table 4.14 Final Efficiencies for Prompt Electrons.**

Data Set	Momentum (Gev/c)	Transverse Momentum, (Gev/c)				
		0.0	0.5	1.0	1.5	2.0
Isobutane	0.0	.119				
	0.5	.153	.161			
	1.0	.122	.170	.137		
	1.5	.110	.150	.186	.145	
	2.0	.114	.152	.179	.159	.124
Nitrogen	0.0	.103				
	0.5	.130	.150			
	1.0	.114	.137	.126		
	1.5	.117	.133	.163	.159	
	2.0	.111	.162	.137	.146	.122
	2.5	.111	.147	.150	.144	.089
	3.0	.091	.110	.159	.167	.124
	3.5	.073	.114	.124	.082	.108
	4.0	.106	.159	.124	.108	.172
	4.5	.133	.168	.116	.114	.101
5.0	.102	.092	.137	.153	.124	

*Final efficiencies for prompt electrons produced over  $4\pi$  steradians to pass the electron filter and scanning.*

Table 4.14 gives the final electron detection efficiency as a function of  $P$  and  $P_t$  including all corrections.

#### § 4.5 BACKGROUND NORMALIZATION

The backgrounds can be classified as electron backgrounds, those due to gamma conversion electrons and dalitz decay electrons, and to nonelectron backgrounds where a nonelectron is called a direct electron. Other backgrounds are event backgrounds. They are usually two photon events,  $\tau^+\tau^-$  events, or beam gas events.

The major source of background to the electron candidates is from gamma conversion electrons and from the electrons of dalitz decays. Other smaller sources are from hadrons above momentum threshold in the Čerenkov counter, but reconstructed by the tracking algorithms with momentum below threshold.

##### 4.5.1 Hadron Background

The hadron background normalization is determined from the Monte Carlo. The results, however, depend on how well the Monte Carlo simulates the real process. For Monte Carlo events  $\approx .005$  clusters per event pass the filter with hadrons misidentified as electrons. A hadron below pion threshold can be identified as an electron only if it occupies a Čerenkov cell with a particle which is above threshold.

**Table 4.15 Nonelectron Background Rates per Event.**

Background Type	Data Set	
	Isobutane	Nitrogen
$\gamma$ -electron	.0035	.0062
prompt electron	.0005	.0009
$\pi$ , $P >$ threshold	.0017	.0005
total	.0058	.0076
total after scan	.0043	.0057

*Misidentification rate for electron candidates in Monte Carlo because of occupying a Čerenkov cell with each of the above.*

Table 4.15 lists the different ways a nonelectron is misidentified as a prompt electron and the associated rates in Monte Carlo events.

The background from hadrons occupying a cell with a direct electron is very small and occurs only in multiple track clusters. Pulse height analysis is used to make the electron selection, and  $\pi - e$  confusion is most likely when the  $\pi$  and the  $e$  have similar momentum and direction. This reduces the effect of this background and does not affect the normalization.

Background from gamma conversion electrons occupying a cell with a pion is also small. These are gamma conversions where the track associated with the gamma conversion electron can be seen. Most of these are removed in scanning.

Pions above threshold, 2.5 Gev/c in isobutane and 5.7 Gev/c in nitrogen, are identified as electrons because of momentum resolution which is about 8% at threshold. Careful pulse height analysis can extend  $\pi - e$  separation a few hundred Mev/c above threshold so that selecting tracks below 2.5 Gev/c in isobutane and 5.5 Gev/c in nitrogen virtually eliminates this source of background.

The main source of hadron backgrounds is caused by late gamma conversions occurring in the inner Čerenkov envelope. Most of these are tagged by stubs in the PDC behind the associated Čerenkov cell. This background makes up about 25% of the final electron candidates. The accuracy of the final electron distributions depends on how well this background is known. The misidentification of pions due to this overlap problem is studied by a track-flipping technique and by Monte Carlo methods.

The track-flipping technique is used to measure the overlap of pions and particles above threshold in the same Čerenkov cell. The misidentification probability can be determined as a function of any desired physical quantity such as momentum, transverse momentum, sphericity, multiplicity, triplicity, any-and-all-icities, etc.

The distributions are obtained by reflecting tracks through the origin and adding simulated pion responses to the associated counters. This is illustrated in figure 4.7. The flipped event is sent through electron filter and the results are tabulated to find misidentification probabilities. The technique is very accurate for DELCO since the flipped tracks have low energy and only slightly disturb the opposite jet. There is no need to consider the effect of overlapping responses (such as overlapping showers in the shower counter), but only the shared occupancy of the same counter.

If each track in a multihadron event is flipped, then the normalization and spectrum of the pion background are directly obtained. The results can be checked with Monte Carlo. Tracks are flipped in Monte Carlo and the results can be compared to the true value of the Monte Carlo pion background since the answer

RUN 5410 CYC 263 EVT 19078  
X - Y PROJ

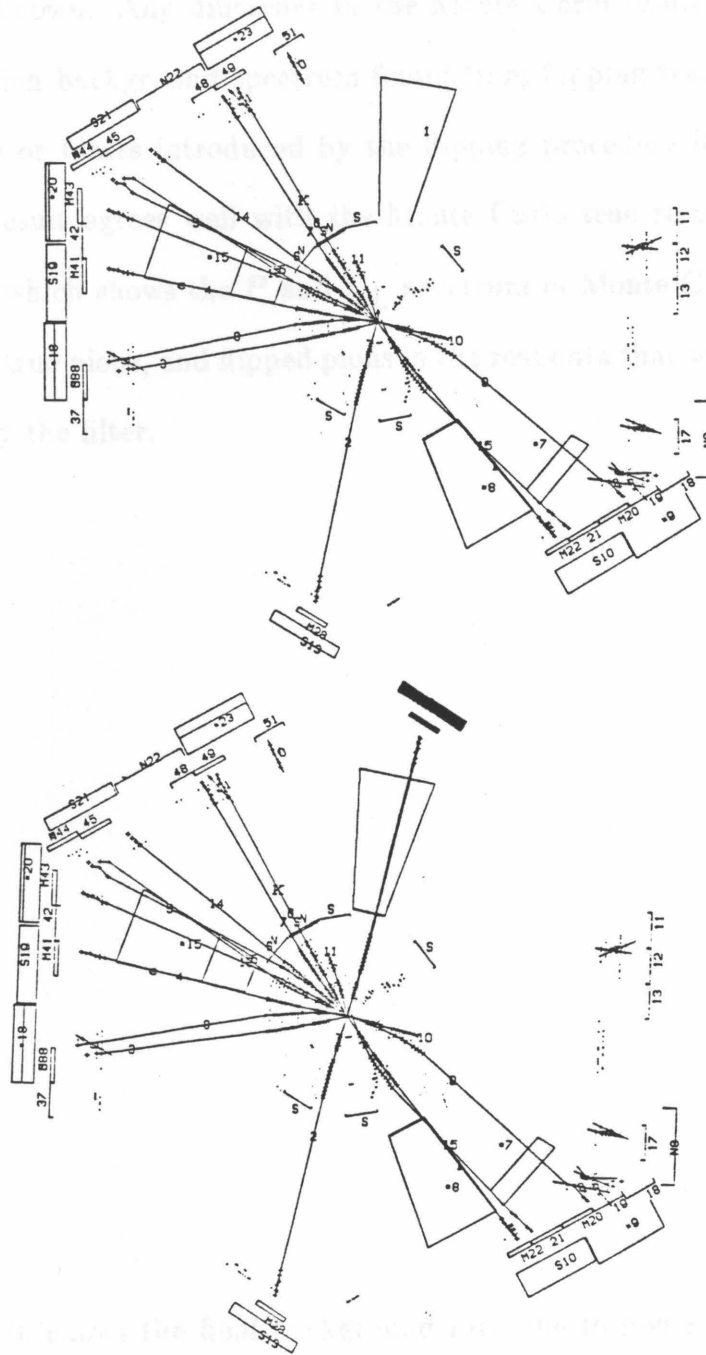


Fig. 4.7 Event with track-flipping. Top, original event. Bottom, event after flipping track 2 and adding MC response for BSH.

is definitely known. Any difference in the Monte Carlo result could be used to correct the pion background spectrum found from flipping tracks in real events. Any artifacts or biases introduced by the flipping procedure itself are removed.

The final result agrees well with the Monte Carlo true result as can be seen in figure 4.8 which shows the  $P$  and  $P_{\perp}$  spectrum of Monte Carlo flipped pions, Monte Carlo true pions, and flipped pions in the real data that were called electron candidates by the filter.



Table 4.16 shows the final background rate due to nonelectrons for all data sets before scanning. The difference between 1982 and 1983 isobutane data is due to the introduction of masks over the mirrors to reduce the rate of Čerenkov cells' firing because of gamma-splashes which were described in section 4.3.5. The masks reduced the rate in 1983 to 73.2% of that in 1982 and the result agrees well with the value of 71.4% in section 4.3.5 .

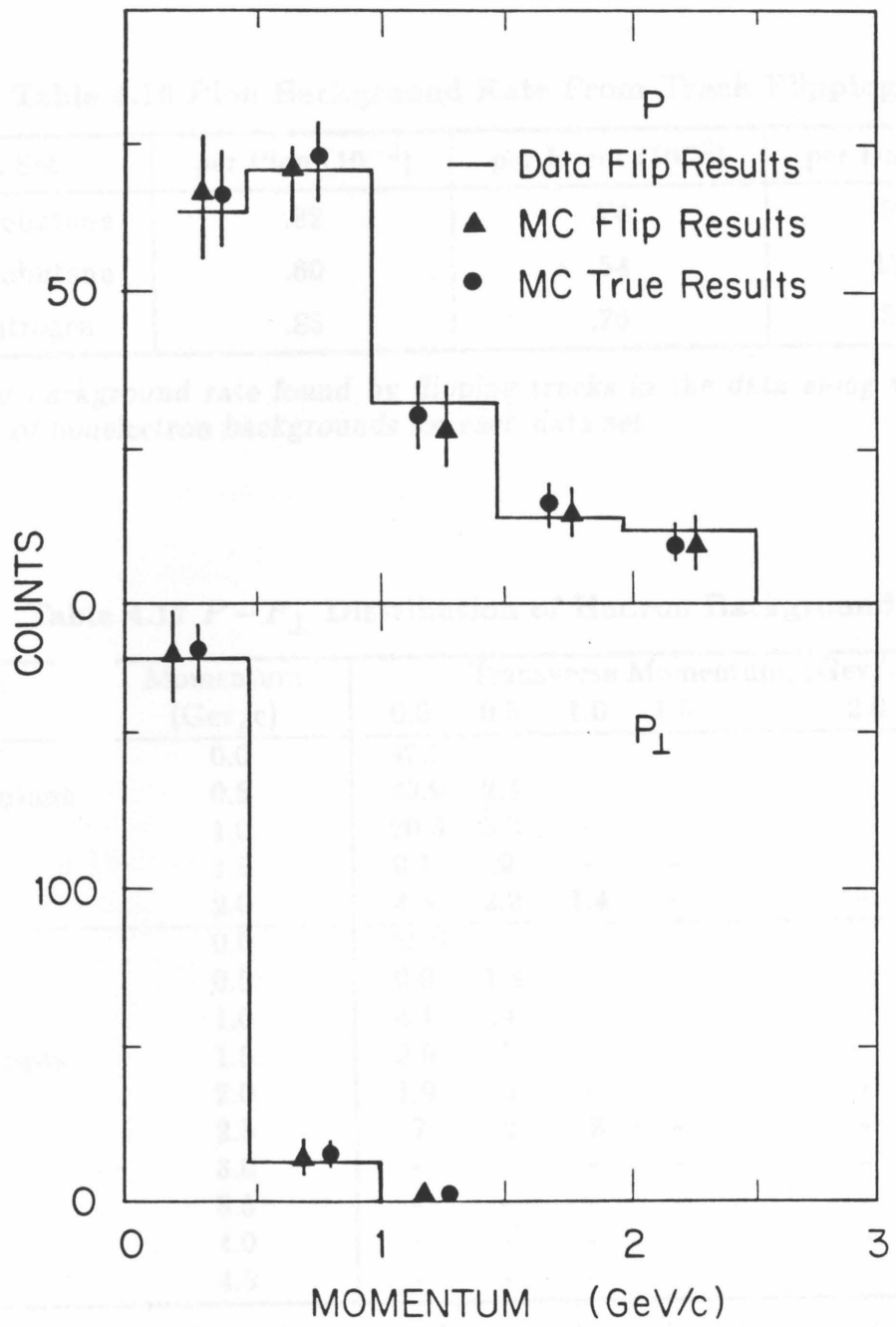


Fig. 4.8 Pion background from track flipping and Monte Carlo.

**Table 4.16 Pion Background Rate From Track Flipping.**

Data Set	per Pion ( $10^{-3}$ )	per Event ( $10^{-2}$ )	per Data Set
82 isobutane	.82	.74	59
83 isobutane	.60	.54	135
83 nitrogen	.85	.76	55

*Pion background rate found by flipping tracks in the data along with total number of nonelectron backgrounds for each data set.*

**Table 4.17  $P - P_{\perp}$  Distribution of Hadron Background.**

Data Set	Momentum (Gev/c)	Transverse Momentum, (Gev/c)				
		0.0	0.5	1.0	1.5	2.0
Isobutane	0.0	47.3				
	0.5	49.9	2.4			
	1.0	20.3	3.3	-		
	1.5	9.1	.9	-	-	
	2.0	4.3	2.2	1.4	-	-
Nitrogen	0.0	22.0				
	0.5	9.0	1.4			
	1.0	4.1	.4	-		
	1.5	2.9	.3	-	-	
	2.0	1.9	.2	-	-	-
	2.5	.7	.2	.2	-	-
	3.0	-	-	-	-	-
	3.5	-	-	-	-	-
	4.0	-	-	-	-	-
	4.5	-	-	-	-	-

*Final normalized nonelectron background determined from track flipping in the data and corrected for scanning efficiency.*

Table 4.17 gives the flipped pion background rates determined from the data as a function of momentum and transverse momentum. The results include corrections for scanning efficiency and are the final normalized background contributions

to the electron candidates.

#### 4.5.2 Gamma Electron Background

The gamma electron background is determined by using the Monte Carlo. This is a direct determination, and the Monte Carlo must accurately simulate the data for this method to be reliable. The proper simulation of  $\gamma$  conversions and Dalitz decays in the Monte Carlo is checked by comparing the characteristic distributions of identified  $\gamma$  conversions in multihadron events of the data with those events in the Monte Carlo. The momentum distribution of gamma electrons is shown in figure 4.9.

**Table 4.18  $P - P_{\perp}$  Distribution of Gamma Electron Background**

Data Set	Momentum (Gev/c)	Transverse Momentum, (Gev/c)				
		0.0	0.5	1.0	1.5	2.0
Isobutane	0.0	46.3				
	0.5	27.9	5.0			
	1.0	2.5	1.2	1.0		
	1.5	1.2	-	-	.6	
	2.0	1.5	-	-	-	-
Nitrogen	0.0	11.4				
	0.5	8.5	1.6			
	1.0	.8	-	-		
	1.5	.7	-	-	-	
	2.0	.7	.8	-	-	-
	2.5	.7	-	-	-	-
	3.0	.7	-	-	-	-
	3.5	-	-	-	-	-
	4.0	-	-	-	-	-
	4.5	-	-	-	-	-

*Final normalized background of electrons from gamma conversions and Dalitz decays found from Monte Carlo including all corrections to Monte Carlo electron efficiency and scanning efficiency.*

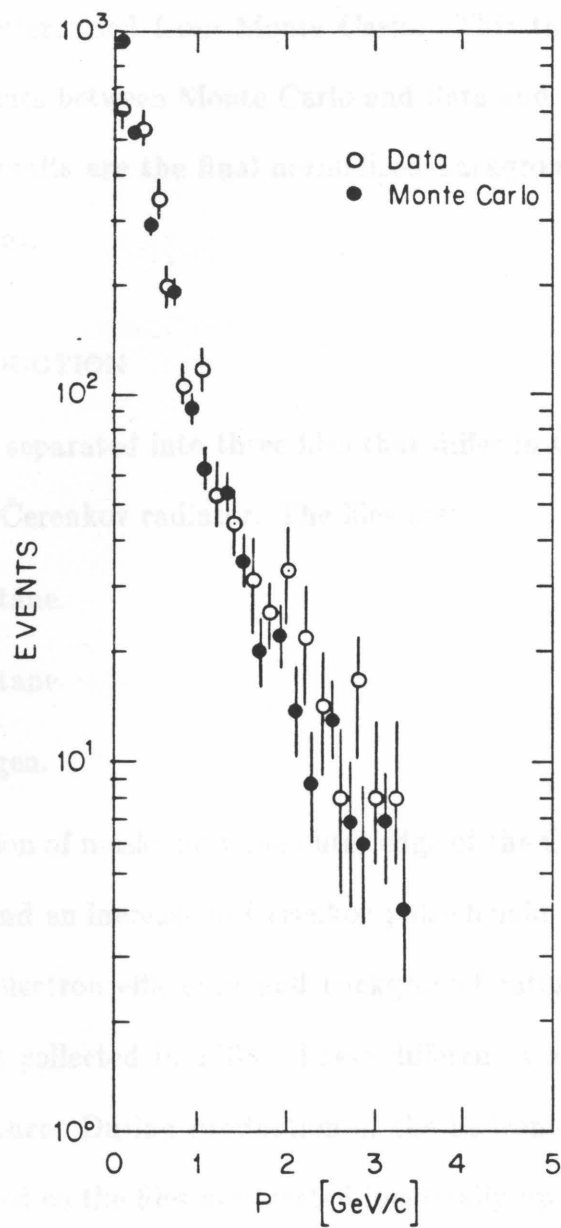


Fig. 4.9 Momenta of gamma electrons in MC and data

The  $P - P_t$  distribution is given in table 4.18 for the expected gamma electron background as determined from Monte Carlo. This table includes corrections for the discrepancies between Monte Carlo and data and corrections for scanning efficiency. The results are the final normalized background contributions to the electron candidates.

#### § 4.6 DATA REDUCTION

The data are separated into three files that differ in Čerenkov counter acceptance and in the Čerenkov radiator. The files are:

1. 1982 isobutane.
2. 1983 isobutane.
3. 1983 nitrogen.

The installation of masks over the outer edge of the Čerenkov counter mirrors ( $\cos \theta > 0.62$ ) and an increase in Čerenkov pulse height discriminator thresholds caused different electron efficiency and background rates between data collected in 1982 and that collected in 1983. These differences affect only the Čerenkov counter performance. During production of the hadronic data sets no Čerenkov information is used so the files are treated identically up to that point.

The data were written on to 6250 bpi tapes from the data acquisition system by a VAX 11/780 computer. The raw data tapes were condensed on to copied tapes, with a more efficient record format, by the SLAC IBM 3081 computer. The copied tapes were run through a PASS 1 production program which did basic pattern recognition and event classification using drift chamber, BSH, pole tip counter, and luminosity counter information. At this stage most of the uninteresting events,

such as cosmic ray events and beam gas interactions, were removed. The PASS 1 tapes are used for final surveys and calibrations and then run through a PASS 2 production program. PASS 2 does a final fit to found tracks and writes out correlated track-counter information. An event classification algorithm is called at the end of the PASS 2 program.

Events classified as multihadrons were skimmed off the PASS 2 tapes and used in the direct electron analysis.

Classified hadron events that passed the electron filter were put onto three disk files, one for each data set.

**Table 4.19 Data Reduction Rates.**

Stage	Data Set	
	Isobutane	Nitrogen
$\int Ldt$	92.5 pb <sup>-1</sup>	26.3 pb <sup>-1</sup>
Triggers	$\sim 8.7 \cdot 10^6$	$\sim 2.5 \cdot 10^6$
Multihadrons	33047	9525
Electron Events	636	241
Prompt Electrons	646	257

Event rates for the different data reduction stages are shown in table 4.19. The final scanned electrons were from 33047 events collected with isobutane in the Čerenkov counter and 9525 events collected with nitrogen. There are 588 final events with electron candidates including 26 events with more than one  $e^\pm$  candidate. A typical prompt electron event is shown in a one-event display picture in figure 4.10.

The SLD prompt electron data set is composed of real or mono electron pairs  
plus backgrounds. Analysis of the results are given in the following chapter

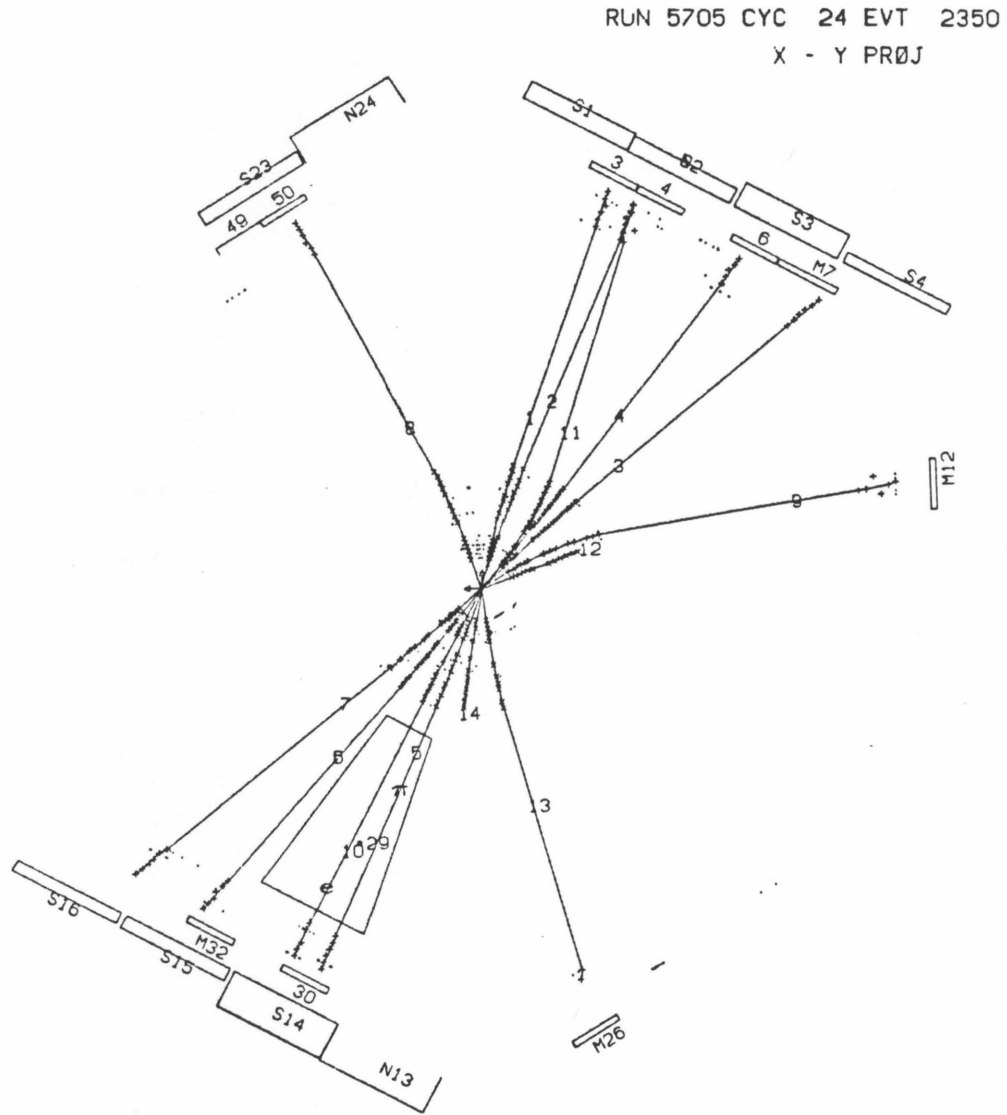


Fig. 4.10 One event display of a prompt electron candidate

The final prompt electron data set is composed of real prompt electrons and electron backgrounds. Analysis of the results are given in the following chapter.

## Analysis and Results

The prompt electron rate and differential cross section are extracted from the electron candidates by statistically subtracting the background and correcting the remainder by the electron detection efficiency. The total prompt electron cross section can be found by integrating the final differential cross section over the momentum range analyzed.

The individual semielectronic branching ratios of the charm and bottom flavored mesons are found by unfolding the momentum and transverse momentum spectra of the prompt electrons. The final rates are found by fitting the  $P - P_{\perp}$  spectrum to a particular shape that extends over the entire kinematic range.

The momentum of an electron produced in the decay of a heavy quark,  $q$ , depends on the momentum of the meson that contained  $q$ . In Monte Carlo models of quark fragmentation, the momentum distribution of the meson that contains  $q$  is given by a fragmentation function,  $D(z)$ . This is the probability that the meson will have a fraction  $z$  of the original momentum that  $q$  had before hadronization. Hence the shape of the  $e^{\pm}$  momentum spectrum can depend on the fragmentation functions of the  $c$  and  $b$  quarks.

The electron momenta transverse to the event thrust axis depends on the mass of the meson that decays and enables the separation of electrons of  $b$  decays from those of  $c$  decays. The fragmentation and the branching fractions of the  $c$  and  $b$  are simultaneously determined by fitting an expected Monte Carlo distribution to the momentum and transverse momentum spectrum of the prompt electron candidates.

### § 5.1 PROMPT ELECTRON DIFFERENTIAL CROSS SECTION

**Table 5.1  $P - P_{\perp}$  Distribution of Prompt Electron Candidates.**

Data Set	Momentum (Gev/c)	Transverse Momentum, (Gev/c)				
		0.0	0.5	1.0	1.5	2.0
Isobutane	0.0	131				
	0.5	170	45			
	1.0	80	45	14		
	1.5	39	25	19	5	
	2.0	34	24	12	3	0
Nitrogen	0.0	58				
	0.5	46	9			
	1.0	20	13	6		
	1.5	13	9	3	3	
	2.0	3	13	1	0	0
	2.5	8	8	2	1	0
	3.0	4	4	2	1	1
	3.5	3	3	1	0	0
	4.0	5	2	3	0	0
	4.5	0	3	0	1	0
5.0	0	2	2	2	1	

*Final distribution of prompt electron candidates after scanning.*

The final  $P - P_{\perp}$  distribution of electron candidates, including the background

contributions from hadrons and gamma electrons, is shown in table 5.1. The normalized background distributions, including the effect of scanning inefficiency, are given in tables 4.17 and 4.18 . The background is limited to the low  $P_{\perp}$  bins, and the signal to noise is given for each bin. The background is subtracted bin by bin, and the result is corrected for the electron detection efficiency given in table 4.14 . The absolute rate of candidates as function of momentum is shown in figure 5.1 for isobutane and nitrogen. The final differential cross section in  $P$  is shown in figure 5.2, with results plotted separately for isobutane and nitrogen data. Results from Mark II are also shown<sup>32</sup>. There is good agreement between the results of all three data sets.

The total cross section for the momentum range covered by isobutane and for nitrogen is found by integrating over the spectrum in figure 5.2 and is given in table 5.2. Only the data above 0.5 Gev/c are used since the data below this are about 75% background.

## § 5.2 FITTING THE $P - P_t$ SPECTRUM

### 5.2.1 Contributions to the Spectrum

Table 5.1 shows the  $P$  vs  $P_{\perp}$  distribution for  $e^{\pm}$  candidates including the expected backgrounds for 92.5  $pb^{-1}$  of isobutane data and 26.3  $pb^{-1}$  of nitrogen

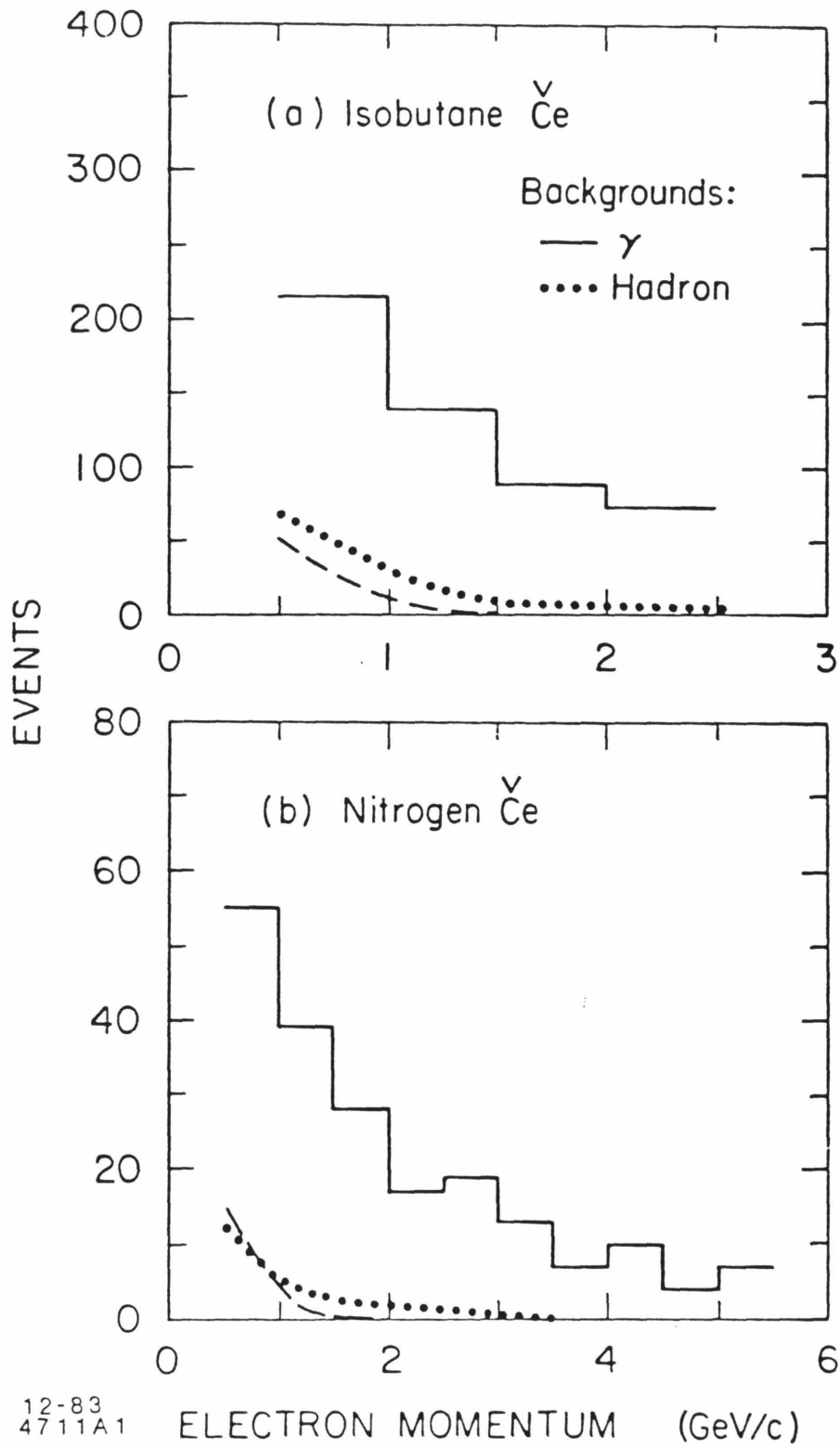


Fig. 5.1 Momentum spectrum of candidates including background

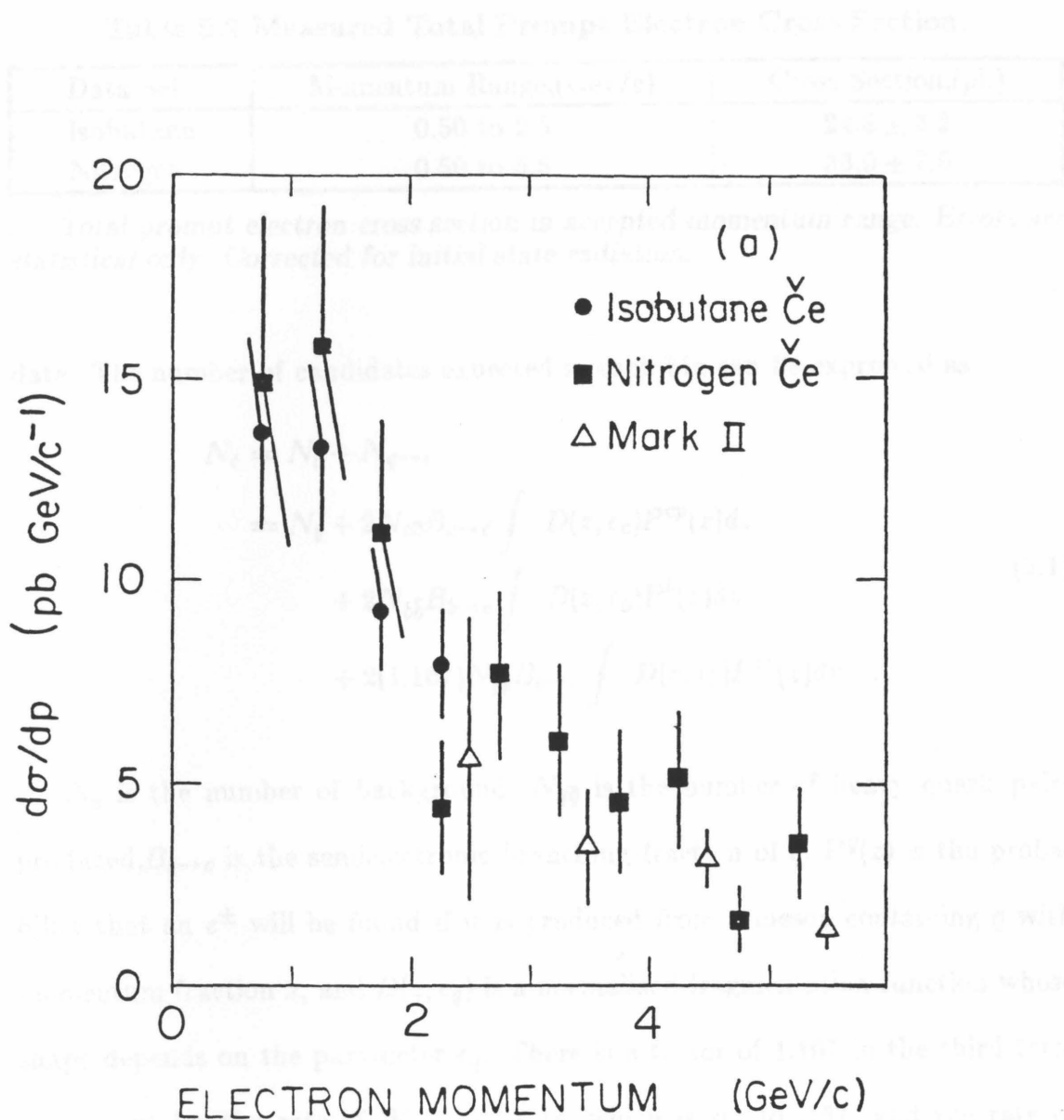


Fig. 5.2 Prompt electron differential cross section vs *P*.Isobutane and nitrogen data plotted separately. Mark II results plotted for comparison.

**Table 5.2 Measured Total Prompt Electron Cross Section.**

Data Set	Momentum Range,(Gev/c)	Cross Section,(pb)
Isobutane	0.50 to 2.5	$24.8 \pm 3.2$
Nitrogen	0.50 to 5.5	$36.9 \pm 7.5$

*Total prompt electron cross section in accepted momentum range. Errors are statistical only. Corrected for initial state radiation.*

data. The number of candidates expected in each bin can be expressed as

$$\begin{aligned}
 N_c &= N_b + N_{q \rightarrow e} \\
 &= N_b + 2N_{c\bar{c}}B_{c \rightarrow e} \int D(z, \epsilon_c)P^{c\bar{p}}(z)dz \\
 &\quad + 2N_{b\bar{b}}B_{b \rightarrow e} \int D(z, \epsilon_b)P^b(z)dz \\
 &\quad + 2(1.167)N_{b\bar{b}}B_{c \rightarrow e} \int D(z, \epsilon_b)P^{c\bar{s}}(z)dz .
 \end{aligned} \tag{5.1}$$

$N_b$  is the number of background,  $N_{q\bar{q}}$  is the number of heavy quark pairs produced,  $B_{q \rightarrow e}$  is the semielectronic branching fraction of  $q$ ,  $P^q(z)$  is the probability that an  $e^\pm$  will be found if it is produced from a meson containing  $q$  with momentum fraction  $z$ , and  $D(z, \epsilon_q)$  is a normalized fragmentation function whose shape depends on the parameter  $\epsilon_q$ . There is a factor of 1.167 in the third term to account for the rate of  $W_{virtual} \rightarrow \bar{c}s$ , which is set to .167, and the rate of  $b \rightarrow cW_{virtual}$  which is set to 1.0 . The initial values for the  $b$  decay rates in the spectator model<sup>43,63</sup> are

Channel	Rate
$b \rightarrow c e\bar{\nu}_e$	.144
$\rightarrow c \mu\bar{\nu}_\mu$	.144
$\rightarrow c \tau\bar{\nu}_\tau$	.033
$\rightarrow c \bar{u}d(s)$	.507
$\rightarrow c \bar{c}s(d)$	.167

The  $b\bar{b}$  and  $c\bar{c}$  events were generated using the Lund Monte Carlo without initial state photon bremsstrahlung and with flat fragmentation functions. The events were divided into four  $z$  regions each for  $c$  and  $b$  flavored mesons. For the  $i^{th}$   $z$ -region the average probability for detecting a prompt electron including all detection efficiencies is  $P_i^q(p, p_t)$  for  $q$  being either  $b$ ,  $c_{primary}$ , or  $b_{secondary}$ . Equation (5.1) then becomes

$$\begin{aligned}
 N_c = N_b + 2N_{c\bar{c}}B_{c\rightarrow e} \sum_{i=1}^4 C_i^{cp}(\epsilon_c)P_i^{cp} \\
 + 2N_{b\bar{b}}B_{b\rightarrow e} \sum_{i=1}^4 C_i^b(\epsilon_b)P_i^b \\
 + 2(1.167)N_{b\bar{b}}B_{c\rightarrow e} \sum_{i=1}^4 C_i^{cs}(\epsilon_b)P_i^{cs} \quad ,
 \end{aligned} \tag{5.2}$$

where

$$C_i^q(\epsilon_q) = \int_{z_i}^{z_{i+1}} D(z, \epsilon_q) dz \quad .$$

The prompt electron distribution of the data is then fit by adding the expected distributions produced by mesons in different  $z$ -bins. The weight of each  $z$ -bin is varied by adjusting the shape of the fragmentation function with  $\epsilon_q$  and the total normalization with  $B_{q\rightarrow e}$ . For three quark contributions and four  $z$ -bins there are twelve  $P_i^q$  tables. These tables are listed in Appendix A.

$D(z, \epsilon)$  is defined before initial state photon bremsstrahlung, and only the final spectrum can be fit so a correction must be applied to the  $C_i^q$  in equation (5.2). The correction is found from Monte Carlo by generating events with and without initial state photons and with the expected shape for  $D(z, \epsilon)$ . The correction,  $\alpha_i^q$ , is defined as the ratio of  $C_i^q$  found with bremsstrahlung to the value found without.

**Table 5.3 Radiative Corrections to Fragmentation Functions.**

Quark	z-bin			
	$\alpha_1^q$	$\alpha_2^q$	$\alpha_3^q$	$\alpha_4^q$
$c_p$	.512	.548	.624	.735
$b$	.557	.587	.645	.743
$c_s$	.564	.589	.647	.745

Corrections to the fragmentation shape.  $\alpha_i^q$  is the correction factor for the number of  $b$ ,  $c_p$ , or  $c_s$  mesons populating the  $i^{\text{th}}$  z-bin.

Table 5.3 gives the correction factors to the fragmentation shape. The correction values were checked for different fragmentation shapes and did not change significantly. The final candidate spectrum in  $P$  and  $P_{\perp}$  becomes

$$\begin{aligned}
 N_c(p, p_t) = & N_b(p, p_t) + 2N_{c\bar{c}}B_{c \rightarrow e} \sum_{i=1}^4 \alpha_i^{cp} C_i^{cp}(\epsilon_c) P_i^{cp}(p, p_t) \\
 & + 2N_{b\bar{b}}B_{b \rightarrow e} \sum_{i=1}^4 \alpha_i^b C_i^b(\epsilon_b) P_i^b(p, p_t) \\
 & + 2(1.167)N_{b\bar{b}}B_{c \rightarrow e} \sum_{i=1}^4 \alpha_i^{cs} C_i^{cs}(\epsilon_b) P_i^{cs}(p, p_t) \\
 = & N_b(p, p_t) + N_e(p, p_t) \quad .
 \end{aligned} \tag{5.3}$$

### 5.2.2 Contributions from $b \rightarrow \tau \rightarrow e$

There is a small contribution of electrons from the decays of  $\tau$  leptons that are produced in  $b\bar{b}$  events. They are included in the fit by adding a term,  $N_{\tau}(p, p_t)$ , to equation (5.3).  $N_{\tau}(p, p_t)$  was found by generating Monte Carlo events with a typical  $b$  fragmentation shape. The spectrum is normalized by assuming 17% for the best branching ratio,  $B_{\tau \rightarrow e}$ , for  $\tau$  decaying to an electron<sup>64</sup>, and fixing the rate for  $b \rightarrow \tau$  to a constant times the rate for  $b \rightarrow e$  during the fitting process.

The value for the ratio of  $B_{b \rightarrow \tau} / B_{b \rightarrow e}$  is based on universality of the semileptonic decays and on phase space<sup>43</sup> and is set to 0.26 . The contribution to (5.3) from tau decays is then

$$N_{\tau}(p, p_t) = 2N_{b\bar{b}}B_{b \rightarrow e}(0.17)(0.26)P^{\tau}(p, p_t) \quad , \quad (5.4)$$

where  $B_{b \rightarrow e}$  is a fit parameter and  $P^{\tau}(p, p_t)$  is from a table of probabilities for detecting an electron if it is produced in the decay  $b \rightarrow \tau \rightarrow e$ . The table includes all efficiencies and is given in Appendix A.

### 5.2.3 Method of Maximum Likelihood

The fit to the candidate spectrum is performed with a standard minimization package called MINUIT<sup>65</sup> . The fit parameters are adjusted to minimize the negative-log-likelihood,  $L$ , of the data given the Monte Carlo distribution for those parameters.  $L$  is defined as

$$\begin{aligned} L &= -\log \prod_i P_i(n_d, n_m) \\ &= -\sum_i \log P_i(n_d, n_m) \quad , \end{aligned}$$

where  $P_i$  is the Poisson probability of observing  $n_d$  candidates if  $n_m$  are expected from the Monte Carlo prediction for the  $i^{th}$  bin. Using the Poisson distribution

$$P_i = \frac{n_m^{n_d} e^{-n_m}}{n_d!} \quad ,$$

and using Stirling's approximation for  $n_d!$

$$L = -\sum_i n_d \log \frac{n_m}{n_d} - n_d + n_m - \frac{1}{2} \log(2\pi n_d) \quad .$$

Minimizing this function gives the fit parameters for which the probability of observing the configuration of the data is the highest. This corresponds to minimizing the  $\chi^2$  for large  $n$  or for distributions which are Gaussian. For the fit,  $n_m$  is found from equation (5.3) including (5.4), and  $n_d$  for the  $i^{th}$   $P - P_{\perp}$  bin is found from table 5.1.

#### 5.2.4 Error Analysis

The parameter errors are found in MINUIT by calculating the inverse of the second derivative matrix, (the error matrix). The errors are in terms of a desired confidence limit which is set to be equivalent to one standard deviation or 68%. For  $L$  this corresponds to a change of +0.5 from the value of  $L$  at the minimum,  $L_{min}$ , and is based on the relationship of  $\chi^2$  to  $L$

$$\chi^2 = 2 \cdot (L - L_{min}) \quad . \quad (5.5)$$

MINUIT fixes a parameter at a value where  $L = L_{min} + 0.5$  on the basis of the known error matrix, minimizes  $L$  with respect to the remaining parameters, and calculates a new reduced error matrix with the fixed parameter. A new value for the parameter is determined and the procedure is iterated until  $L$  is within a specified tolerance of  $L_{min} + 0.5$ . Errors for each parameter are determined. The errors determined by the MINUIT minimization routines include all statistical errors, assuming that the probability distributions used for calculating  $L$  are accurate. Poisson statistics are used to predict the expected populations of observed candidates.

Systematic errors also contribute to uncertainties in  $n_m$ . The sources of these

errors can be found by analyzing equation (5.3) and are due to uncertainties in  $N_b$ ,  $N_{q\bar{q}}$ ,  $P_i^q(p, p_t)$ ,  $\alpha_i^q$ , and  $C_i^q$ . Equation (5.3) can be rewritten as

$$N_c(p, p_t) = N_\pi(p, p_t) + N_\gamma(p, p_t) + N_e(p, p_t) \quad , \quad (5.6)$$

where  $N_b$  is divided among the nonelectron background,  $N_\pi$ , and the gamma conversion electron background,  $N_\gamma$ . The contributions to the errors in fitting the parameters are then easily divided into three categories corresponding to the uncertainties in the normalization of the terms in equation (5.6). The fitting procedure is adapted to accommodate the uncertainties by introducing three parameters as

$$N_c(p, p_t) = G_\pi \cdot N_\pi(p, p_t) + G_\gamma \cdot N_\gamma(p, p_t) + G_e \cdot N_e(p, p_t) \quad . \quad (5.7)$$

The factors,  $(G_x)$ , are allowed to vary in the fit and are constrained to the uncertainties of the normalizations by introducing them into the likelihood function as

$$L = - \sum_i \log P_i(n_d, n_m) - \frac{(1 - G_\pi)^2}{2\sigma_\pi^2} - \frac{(1 - G_\gamma)^2}{2\sigma_\gamma^2} - \frac{(1 - G_e)^2}{2\sigma_e^2} \quad ,$$

where the  $\sigma$  are the standard deviation errors in the normalizations. The method makes use of the relationship in equation (5.5). This procedure allows a better fit to the data by allowing the background normalization to vary within the uncertainty limits, and it also includes the systematic errors in the confidence limits of the final fit parameters.

The uncertainty in  $N_\pi$  is due to errors from the track-flipping procedure and from the scanning efficiency. The track-flipping accuracy is determined by applying the procedure to Monte Carlo events where the actual background is definitely

known. Figure 4.8 shows that the  $N_\pi$  spectrum is accurately reproduced and is correctly normalized to well within the statistical limits. The uncertainty in scanning efficiency is the largest source of error and is 13% from table 4.13 . The uncertainty in  $N_\gamma$  has a contribution of 15% from scanning uncertainties and 20% from the discrepancy between Monte Carlo and data seen in figure 4.9.

$N_{q\bar{q}}$  is the number of  $q\bar{q}$  events that survive the multihadron selection criteria. The error in the normalization was found in section 4.2 to be 5.5% and is dominated by the uncertainty in the luminosity measurements (5.1%), with smaller errors due to the uncertainty of the amount of  $2-\gamma$  background events and from the Monte Carlo calculations. The results are listed as  $N_{q\bar{q}}/\epsilon_{q\bar{q}}$  in section 4.2 since the efficiencies are factored into the tables of  $P_i^q(p, p_t)$  in Appendix A.

The  $P_i^q$  tables include the efficiencies for multihadron selection, electron selection, and scanning requirements. There are three sources for errors: acceptance and kinematic cuts; BSH and Čerenkov counter requirements; and scanning requirements. There is a 3.3% discrepancy between Monte Carlo and data, for the kinematic cuts listed in section 4.4, for unexplained reasons. The uncertainty in the counter requirement efficiency is derived from the discrepancy in the counter responses between Monte Carlo and data. The run-by-run variations in the data are within 5% of the mean calibration values and the Monte Carlo does not have these variations. The error in the scanning efficiency is 8% from section 4.4 .

**Table 5.4 Sources of Systematic Errors.**

Error	Contribution	Source	Error (%)	Total (%)
$\sigma_\pi$	$N_\pi$	track flipping	$\sim 3$	10.5
		scanning	10	
$\sigma_\gamma$	$N_\gamma$	Monte Carlo	20	21.0
		scanning	7	
$\sigma_e$	$N_{q\bar{q}}$	luminosity	5	11.4
		Monte Carlo	.8	
	$P_i^q$	Monte Carlo	6	
		BSH, Čer	6	
		scanning	5	

Contributions to the systematic errors are listed in table 5.4 .

### § 5.3 RESULTS OF FIT

Three forms of the fragmentation function were used in the fitting procedure,

$$D(z) = \frac{1}{z(1 - \frac{1}{z} - \frac{\epsilon}{1-z})^2} \quad \text{Peterson et al.}$$

$$D(z) = 1 - \epsilon + 3\epsilon(1 - z)^2 \quad \text{Field-Feynman}$$

$$D(z) = 1 \quad \text{flat .}$$

The detailed shape of the fragmentation function can not be resolved since it is smeared by the decay spectrum of the prompt electrons, by the initial state bremsstrahlung spectrum, and by measurement resolution. Because of the smearing effects and statistical limitations, a particular form must be chosen and fit to the data. The fit procedure is equivalent to an unfold method that derives the fragmentation form averaged over all primary mesons containing the heavy quarks

**Table 5.5 Results of Fits to the  $P - P_{\perp}$  Distribution of Electrons.**

Parameter	Peterson et al.	Field-Feynman	flat
$\epsilon_c$	$.053^{+.061}_{-.029}$	$-1.4^{+0.5}_{-1.8}$	-
$\epsilon_b$	$.018^{+.024}_{-.011}$	$-4.0^{+3.6}_{-15.}$	-
$B_{c \rightarrow e}$	$.089 \pm .014$	$.091 \pm .014$	$.089 \pm .013$
$B_{b \rightarrow e}$	$.150 \pm .029$	$.144 \pm .027$	$.119 \pm .021$
$\langle z_c \rangle$	$.68 \pm .06$	$.72 \pm .03$	.52
$\langle z_b \rangle$	$.77 \pm .05$	$.76 \pm .05$	.67
$\chi^2/\text{DoF}$	55/57	54/57	79/60

*Results of fits to the  $P - P_{\perp}$  distribution of electrons. Errors include systematic and statistical uncertainties.*

and generated at 29 Gev with no initial state bremsstrahlung . Once the form is chosen, the contributions to the electron spectrum from mesons at different  $z$  can be adjusted by varying the fit parameter,  $\epsilon$ .

For the fit, there are 7 free parameters including 3 parameters corresponding to the normalization uncertainties. Results of the fit for these parameters and three fragmentation forms are shown in table 5.5 . For the Peterson et al. function, the contributions to the prompt electron signal from background,  $b_{c,primary}$ , and  $b_{secondary}$  are given as functions of  $P$  and  $P_{\perp}$  in Table 5.14. In the following sections all results refer to the fit with the Peterson et al. form of the fragmentation function unless otherwise specified.

### 5.3.1 Semielectronic Rates

The branching ratios are insensitive to the form of the fragmentation function chosen, but may be correlated to the fragmentation parameters if varying the

**Table 5.6 Correlation Coefficients for Fit Parameters.**

Momenta	Parameter	$z_0^c$	$B_{c \rightarrow e}$	$z_0^b$	$B_{b \rightarrow e}$
0.5-5.5 Gev	$z_0^c$	1.000			
	$B_{c \rightarrow e}$	.104	1.000		
	$z_0^b$	-.107	.101	1.000	
	$B_{b \rightarrow e}$	.347	-.067	.346	1.000
2.0-5.5 Gev	$z_0^c$	1.000			
	$B_{c \rightarrow e}$	.593	1.000		
	$z_0^b$	.166	-.261	1.000	
	$B_{b \rightarrow e}$	.425	-.169	.623	1.000

parameter will cause the expected number of electrons in the accepted momentum range to vary.

The correlation matrix, excluding the normalization parameters, is shown in table 5.6 for fits with the Peterson et al. function using the entire data sample and using only the candidates with momenta  $> 2$  Gev. The fragmentation parameters are in terms of the peak of the function,  $z_0$ , where

$$\epsilon = z_0 + \frac{1}{z_0} - 2 \quad .$$

The change of variables is made because  $z_0$  is a better behaved fitting parameter and has more symmetric errors than  $\epsilon$ .

For the data that are restricted to the momenta range above 2 Gev there is a significant correlation between  $z_0$  and the branching ratio of the corresponding quark. The correlation is significantly reduced for the unrestricted data.

The branching ratios agree well with the low energy measurements obtained

**Table 5.7 Low Energy Semileptonic Rates, (%) .**

Experiment	W, Gev	$B_{c \rightarrow e}$	$B_{b \rightarrow e}$	$B_{b \rightarrow \mu}$	Ref.
DELCO	29	$8.9 \pm 1.3$	$15.0 \pm 2.8$		*
DELCO	3.77	$8.0 \pm 1.5$	-	-	16
SLAC-LBL	3.77	$8.2 \pm 2.8$	-	-	15
CLEO	10.5	-	$12.7 \pm 2.1$	$12.2 \pm 3.5$	37
CUSB	10.5	-	$13.2 \pm 1.6$	-	38

*Systematic errors are included. (\* This experiment).*

in the  $b\bar{b}$  and  $c\bar{c}$  resonance regions.<sup>12,15,16,12,37,38</sup>

The present measurements are listed in table 5.7 along with the low energy measurements.

### 5.3.2 Fragmentation Functions

The data are well fitted by the Peterson and the Field-Feynman forms of the fragmentation function with the above parameters. Although the detailed shape of the fragmentation function cannot be measured, a hard spectrum for both the  $b$  and  $c$  mesons is established with the mean values,  $\langle z_b \rangle = 0.77 \pm 0.05$  and  $\langle z_c \rangle = 0.68 \pm 0.06$ . Figure 5.3 shows the shape of the heavy meson fragmentation functions for the parameters found in the fit to the data. These observations are consistent with earlier measurements of  $b$  semileptonic rates and fragmentation in electron<sup>32,33</sup> and muon<sup>33-36,66</sup> experiments.

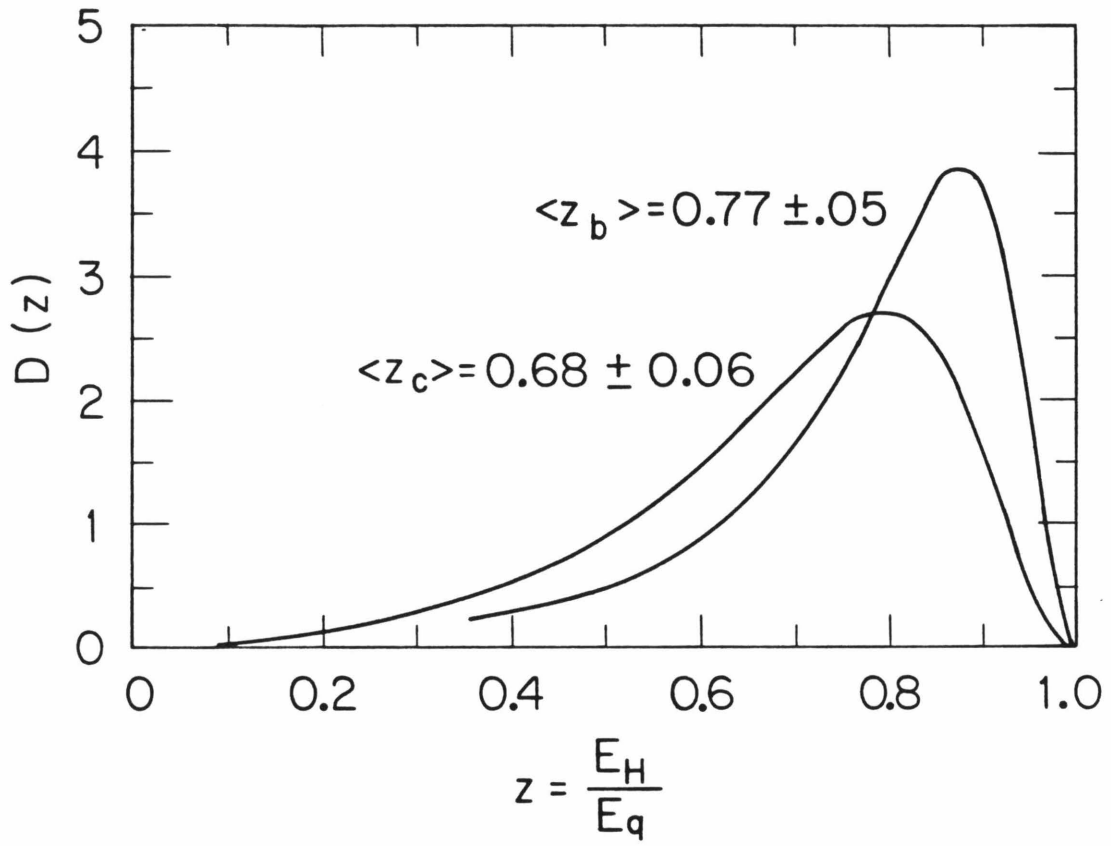


Fig. 5.3 Fragmentation Function for  $b$  and  $c$  Mesons. Results for Peterson et al. function.

**Table 5.8 Fragmentation Functions and Semileptonic Branching Ratios.**

$e^+e^- \rightarrow e^\pm + X$	W, Gev	$B_{b \rightarrow e}$	$\langle z_b \rangle$	$B_{c \rightarrow e}$	$\langle z_c \rangle$	Ref.
DELCO	29	$.150 \pm .028$	$.77 \pm .05$	$.089 \pm .014$	$.68 \pm .06$	*
Mark II	29	$.129 \pm .031$	$.79 \pm .08$	$.064 \pm .031$	-	33
CELLO	14,22,34	$.141 \pm .065$	-	-	-	66
$e^+e^- \rightarrow \mu^\pm + X$	W, Gev	$B_{b \rightarrow \mu}$	$\langle z_b \rangle$	$B_{c \rightarrow \mu}$	$\langle z_c \rangle$	Ref.
MAC	29	$.155^{+.054}_{-.029}$	$.8 \pm .1$	$.076^{+.097}_{-.027}$	$.17-.67$	34
Mark J	33-38	$.105 \pm .020$	$.75 \pm .07$	$.115 \pm .020$	$.46 \pm .05$	35
CELLO	14,22,34	$.088 \pm .045$	-	$.123 \pm .049$	-	66
Mark II	29	$.122 \pm .058$	$.73 \pm .18$	$.081 \pm .024$	-	33
TASSO	34.5	$.117 \pm .030$	$.85^{+.10}_{-.21}$	$.082^{+.023}_{-.016}$	$.77^{+.06}_{-.13}$	36

*Experimental results of heavy quark fragmentation functions and semileptonic branching ratios. Errors include systematic uncertainties. ( \* This experiment).*

The results are shown in table 5.8 . There are two measurements, other than DELCO, of  $\langle z_c \rangle$  in lepton experiments; one measurement, (TASSO)  $\langle z_c \rangle = 0.77^{+0.05+0.03}_{-0.07-0.11}$ , is consistent, and the other measurement, (Mark J)  $\langle z_c \rangle = 0.46 \pm 0.02 \pm 0.05$ , is definitely not consistent.

The DELCO measurement of  $\langle z_c \rangle$  is also consistent with previous measurements in  $e^+e^-$  annihilation which have involved direct fits to the  $D^*$  spectrum.<sup>26-30</sup> Recent results at the PEP and PETRA storage rings have shown that the production of primary charmed mesons occurs primarily via the channel

$$e^+e^- \rightarrow c\bar{c} \rightarrow D^*\bar{D}^* ,$$

so that the  $D^*$  momentum spectrum can be compared to the prompt electron

result, which is the average over all  $c$  mesons. In order to compare the  $D^*$  measurements with the electron data, a variable  $x$  is defined as

$$x = \frac{E_{hadron}}{E_{beam}} = \frac{E_h}{14.5} ,$$

which is the momentum spectrum averaged over all primary mesons. The corresponding values in the Peterson et al. fit for electrons are  $\langle x_b \rangle = 0.76 \pm 0.06$  and  $\langle x_c \rangle = 0.66 \pm 0.06$ . The effect of initial state radiation is to reduce  $\langle z \rangle$  by approximately 2-4% .

**Table 5.9 Charm Fragmentation From  $D^*$  Experiments.**

Experiment	W, Gev	$\langle x_c \rangle$ , lepton	Ref.	$\langle x_c \rangle$ , $D^*$	Ref.
Mark II	29	-		$0.58 \pm 0.06$	26
HRS	29	-		$0.51 \pm 0.04$	29
CLEO	10.5	-		$0.63 \pm 0.02$	27
TASSO	34.5	$0.71^{+.06}_{-.13}$	36	$0.58 \pm 0.04$	28
DELCO	29	$0.66 \pm 0.06$	*	$0.6 \pm 0.1$	30

(\* This experiment.)

The  $D^*$  measurements of various experiments are listed in table 5.9 for comparison with the electron result.

### 5.3.3 Total Cross Section for Prompt Electrons

The results of Section 4.3 are used to calculate the differential cross section for prompt electrons from  $b\bar{b}$  and  $c\bar{c}$  production throughout the allowed kinematic

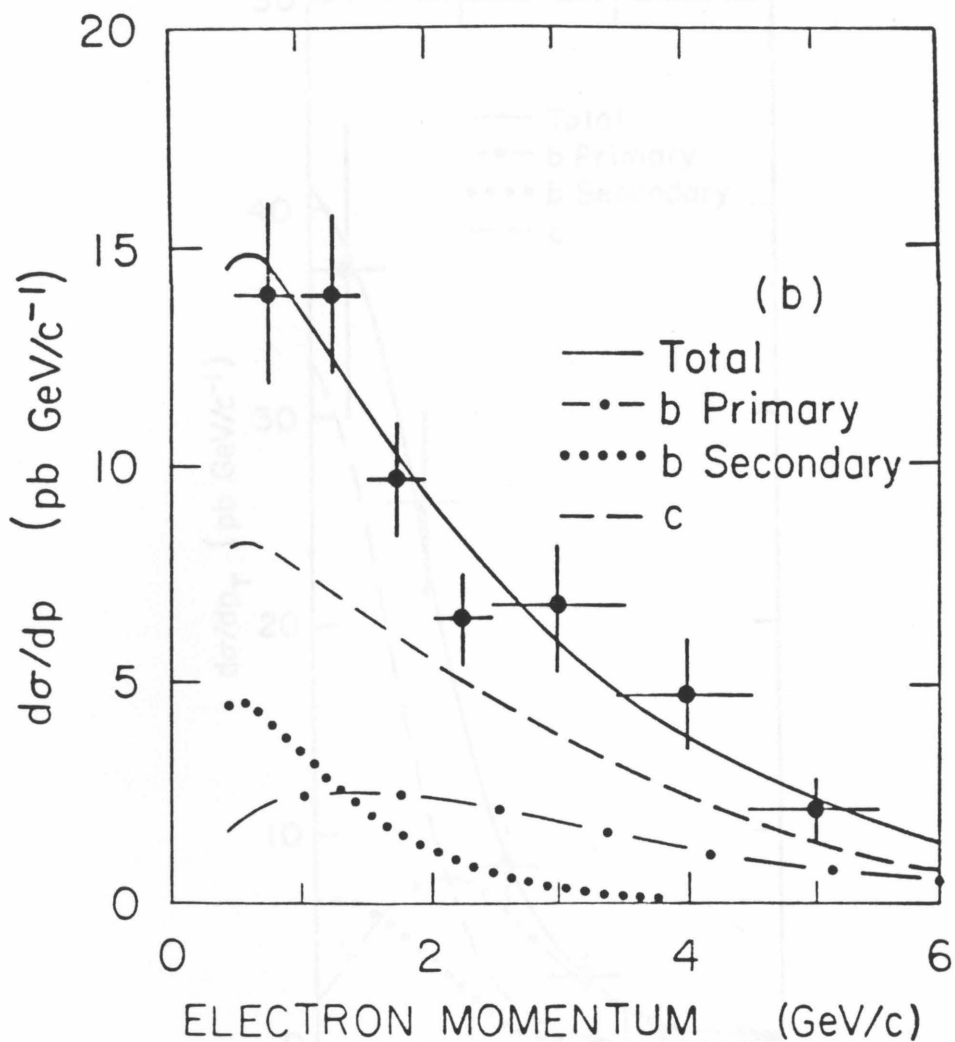


Fig. 5.4 Fit to Electron Differential Cross Section vs  $P$ .

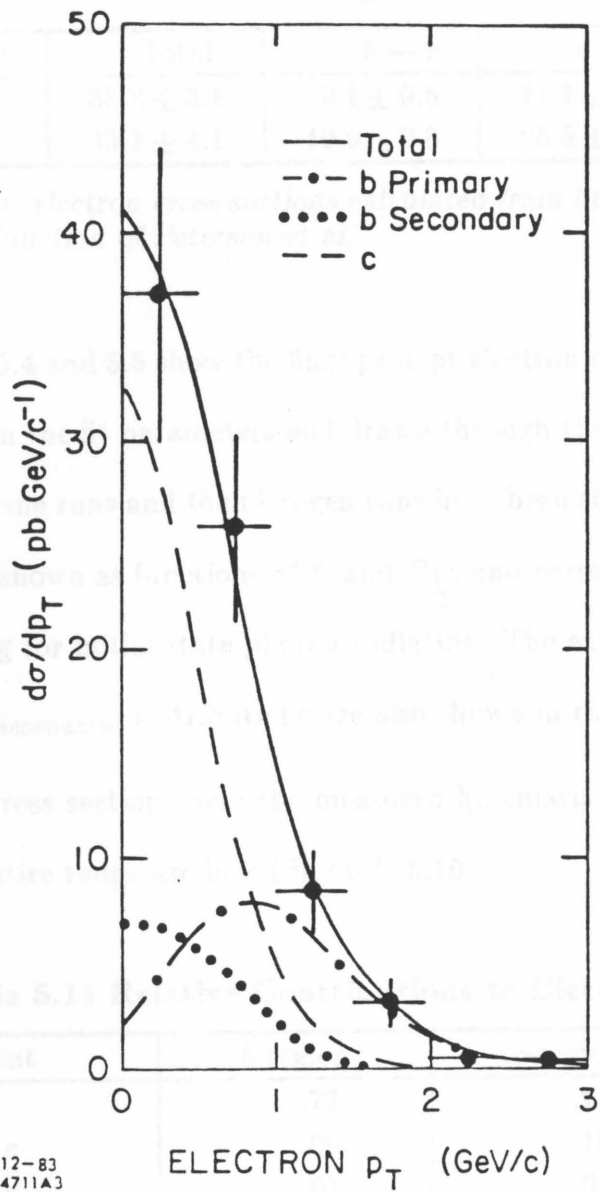


Fig. 5.5 Fit to Electron Differential Cross Section vs  $P_{\perp}$ .

**Table 5.10 Cross Section of Prompt Electron Contributions, (pb).**

Range, (Gev)	Total	$b \rightarrow e$	$c \rightarrow e$	$b \rightarrow c \rightarrow e$
0.5-5.5	$35.8 \pm 3.1$	$9.1 \pm 0.5$	$21.1 \pm 1.7$	$5.5 \pm 0.8$
0.0-14.5	$45.1 \pm 4.1$	$10.9 \pm 0.6$	$26.5 \pm 2.1$	$7.1 \pm 1.1$

Total prompt electron cross sections calculated from fit to the signal using the fragmentation function of Peterson et al.

range. Figures 5.4 and 5.5 show the final prompt electron differential cross section determined from the fit parameters and drawn through the data points. The data from the isobutane runs and the nitrogen runs have been statistically added in the plot. They are shown as functions of  $P$  and  $P_{\perp}$ , and correspond to  $\sqrt{s} = 29$  Gev after accounting for initial state photon radiation. The expected spectra of the  $b$ ,  $c_{primary}$ , and  $b_{secondary}$  contributions are also shown in the figures.

The total cross sections over the measured kinematic range and those calculated for the entire range are listed in table 5.10 .

**Table 5.11 Relative Contributions to Electron Signal.**

Component	$b$ -region	$c$ -region	all
$b \rightarrow e$	.77	.21	.22
$b \rightarrow c \rightarrow e$	.06	.10	.15
$b \rightarrow \tau \rightarrow e$	.01	.01	.01
$c \rightarrow e$	.11	.56	.39
nonelectron	.05	.12	.23
$e^+e^- \rightarrow b\bar{b}$	.84	.33	.40
$e^+e^- \rightarrow c\bar{c}$	.14	.62	.51
# electrons	84	116	550
# background	4	16	164

Relative rates of prompt electron signals in  $b$ -enhanced ( $P_{\perp} > 1$  Gev/c) and  $c$ -enhanced ( $P_{\perp} < 1$  Gev/c,  $P > 2$  Gev/c) regions, and in the total sample.

The tables in Appendix B show that the relative contributions to the signal from  $b\bar{b}$  and  $c\bar{c}$  events depend on  $P_{\perp}$ . By placing cuts on the allowed  $P_{\perp}$  of the prompt electron signal, the relative rate of one or the other of these event types can be enhanced. Table 5.11 gives the relative contributions to the signal of events with candidates that have  $P_{\perp} > 1$  Gev and those that have both  $P_{\perp} < 1$  Gev and  $P > 2$  Gev corresponding to  $b$ -enhanced and  $c$ -enhanced portions of the data. This provides a method of selecting mostly  $b\bar{b}$  events ( $\sim 84\%$  pure) for further analysis.

#### 5.3.4 Sensitivity to $b \rightarrow u$

Models of quark mixing<sup>67-68</sup> suggest that the semielectronic decays of the  $b$  quark can proceed via the following two channels

$$b \rightarrow c e^{-} \bar{\nu}_e$$

$$b \rightarrow u e^{-} \bar{\nu}_e .$$

The relative rates of these two reactions depend on the elements of the quark mixing matrix<sup>8,63</sup>. Results of recent measurements<sup>38</sup> at the CESR  $e^+e^-$  storage ring of  $\Upsilon'''$  decays have set a limit of  $B_{b \rightarrow u} < 0.05$  at a .90 confidence limit.

The sensitivity of the present analysis to the rate of  $b \rightarrow u$  was checked by introducing a free parameter, corresponding to the cascade electron rate, into the fitting analysis. The factor of 1.167 in equation (4.1) was replaced by the factor of  $(B_{b \rightarrow c} + 0.167)$ . There are no cascade electrons for this decay channel since the  $u$  does not decay into electrons. The parameter was allowed to vary between 0 and 2; the fragmentation parameters were fixed at the previous best fit values;

and the semielectronic rates were left free to vary. The result of this fit gives  $B_{b \rightarrow c} = 0.85_{-.54}^{+.77}$ , showing low sensitivity for this measurement. The rate was set to 1.0 for this analysis to be consistent with the results from CESR.

### 5.3.5 Limits on Anomalous Electron Production

The copious production of prompt electrons, at PEP, from sources other than  $b$  and  $c$  decays would be reflected in semielectronic rates significantly larger than the rates measured at lower energies. We have investigated the presence of anomalous electrons by fixing the semielectronic rates to the values listed in table 5.7, and calculating the prompt electron cross section over the measured momentum range. The expected cross section for these rates is  $30.8 \pm 2.8$  pb. The errors include uncertainties in fragmentation found by allowing  $\langle z \rangle$  to vary from .55 to .95 for both  $b$  and  $c$ . The difference between this and the measured cross section of  $35.8 \pm 3.1$  pb is  $5.0 \pm 4.1$  pb, giving an upper limit for anomalous electron production in the momentum range of 0.5 Gev to 5.5 Gev of 11.6 pb at the 90% confidence level.

## § 5.4 MULTI-ELECTRON EVENTS

Several events with two prompt electron candidates were seen in the data. A typical two electron event is shown in figure 5.6. These events are produced by the semielectronic decay of two or more quarks (antiquarks) in the same event. The rate for detecting the events is very low because the efficiency and low production rate are approximately squared. The lower momentum limit for this study is .25 Gev/c in order to increase the kinematical acceptance for these events.

Table 5.32 Dielectron Event Rates

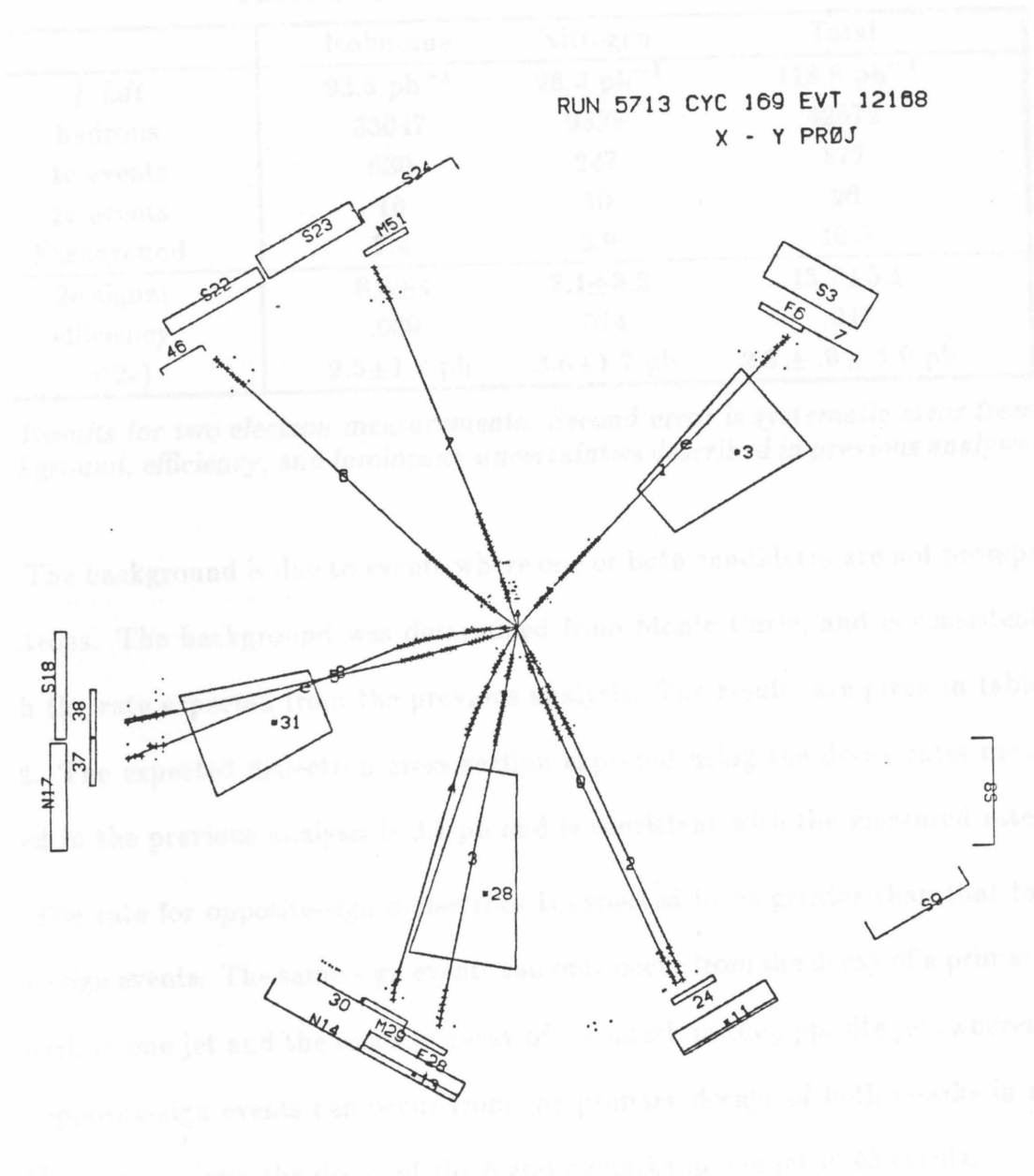


Fig. 5.6 Dielectron event.

**Table 5.12 Dielectron Event Rates.**

	Isobutane	Nitrogen	Total
$\int Ldt$	92.5 pb <sup>-1</sup>	26.3 pb <sup>-1</sup>	118.8 pb <sup>-1</sup>
hadrons	33047	9525	42572
1e events	630	247	877
2e events	16	10	26
background	7.4	2.9	10.3
2e signal	8.6±4	7.1±3.2	15.7±5.1
efficiency	.039	.074	.047
$\sigma(2e)$	2.5±1.0 pb	3.6±1.7 pb	2.8 ± .9 ± 1.0 pb

*Results for two electron measurements. Second error is systematic error from background, efficiency, and luminosity uncertainties described in previous analysis.*

The background is due to events where one or both candidates are not prompt electrons. The background was determined from Monte Carlo, and is consistent with the rate expected from the previous analysis. The results are given in table 5.12. The expected dielectron cross section expected using the decay rates measured in the previous analysis is 3.1 pb and is consistent with the measured rate.

The rate for opposite-sign dielectrons is expected to be greater than that for same-sign events. The same-sign events can only occur from the decay of a primary  $b$  quark in one jet and the cascade decay of a  $c$  quark in the opposite jet, whereas the opposite-sign events can occur from the primary decays of both quarks in  $c\bar{c}$  or  $b\bar{b}$  events or from the decay of the  $b$  and  $c$  quarks in one jet in  $b\bar{b}$  events.

**Table 5.13 Dielectron Charge Correlations.**

	++, --	+-, -+
expected	7	19
measured	4	21

The expected and measured rates are given in table 5.13 and include background.

For  $B^0 - \bar{B}^0$  mixing, there would be more same-sign dielectrons than expected for the case of no mixing. At this time there are too few data to make any measurements of mixing.

Table 5.14 Fit Contributions to Electron Signal.

Isobutane Data									
Momentum (Gev/c)	Transverse Momentum,(Gev/c)								
	0.0		0.5		1.0		1.5		2.0
0.0	35.0	5.2						$e_C$	$e_B$
	18.6	46.5						$e_b$	$b$
0.5	65.3	6.1	7.4	20.1					
	26.0	49.0	13.4	2.4					
1.0	38.6	2.8	13.3	14.3	1.1	10.2			
	12.2	19.9	10.9	3.3	0.6				
1.5	20.5	2.1	11.4	9.5	0.9	12.5	0.3	3.3	
	6.5	9.0	4.7	0.9	1.4		0.1		
2.0	18.4	3.2	12.1	8.5	2.3	9.2	0.1	5.1	0.4 0.6
	3.9	4.2	3.9	2.2	1.1	1.3	0.3		

Nitrogen Data									
Momentum (Gev/c)	Transverse Momentum,(Gev/c)								
	0.0		0.5		1.0		1.5		2.0
0.0	8.5	1.3						$e_C$	$e_B$
	4.4	21.6						$e_b$	$b$
0.5	16.1	1.3	2.2	5.3					
	7.2	8.8	3.3	1.3					
1.0	10.4	1.0	2.6	3.3	0.3	2.7			
	2.8	4.0	2.1	0.4	0.1				
1.5	8.3	0.5	3.6	2.4	0.4	3.1	0.2	0.8	
	1.8	2.8	1.9	0.3	0.3				
2.0	5.7	0.9	5.2	1.7	0.3	1.9		1.3	0.1 0.2
	0.6	1.9	1.2	0.2	0.3		0.1		
2.5	4.6	0.8	2.6	1.9	0.4	2.1	0.1	1.5	0.1
	0.6	0.7	0.5	0.2		0.2	0.1		
3.0	2.9	0.4	1.9	1.3	0.8	1.5	0.2	1.0	0.2 0.1
	0.3	0.7	0.1		0.1				
3.5	2.0	0.6	1.2	1.1		1.4	0.2	0.2	0.1
			0.2		0.1				
4.0	1.3	0.5	2.5	1.3		1.0	0.1	0.4	0.2
	0.1		0.1		0.1				
4.5	1.8	0.4	1.4	1.3	0.4	0.6	0.1	0.3	0.1
					0.1				
5.0	1.2	0.3	0.2	0.7	0.1	0.7		0.4	
			0.2						

$e_B = b$  primary,  $e_b = b$  cascade,  $e_C = c$  primary,  $b =$  background.

## Summary and Conclusion

In this thesis we have measured the production of prompt electrons in  $e^+e^-$  annihilations at 29 GeV/c. We found 646 events, with electron candidates having momentum between 0.5 and 5.5 GeV/c, including about 25% background. The electron identification relied heavily on the DELCO Čerenkov counter which has high efficiency for electrons with momentum above .25 GeV/c.

The background was primarily composed of gamma conversion electrons and misidentified pions. The gamma conversion contribution was determined with a Monte Carlo calculation after checking that the Monte Carlo gamma electron spectrum correctly reproduced that of the data (figure 4.9). The pion contribution was determined by a track-flipping technique in the data and was checked by using the technique in the Monte Carlo (figure 4.8). The momentum spectrum of the final signal is shown in figure 5.1 including the background contributions. The detection efficiency was determined using the Monte Carlo, and by measuring the electron efficiency in  $2-\gamma$  events. The differential cross section is shown in figure 5.2 after subtracting the background and correcting for electron detection efficiency.

The spectra were fit in the  $P - P_{\perp}$  plane with the results of the Lund Monte

Carlo using the standard model for the weak decays of the heavy quarks. The following three contributions for electrons plus background were used in the fit:

$$b \rightarrow e$$

$$b \rightarrow c \rightarrow e$$

$$c \rightarrow e$$

The momentum spectrum for Monte Carlo electrons was determined by using a variable fragmentation function for the primary heavy hadrons. The function of Peterson et al.,

$$D(z) = \frac{N}{z(1 - \frac{1}{z} - \frac{\epsilon}{1-z})^2} ,$$

was used with an adjustable parameter,  $\epsilon$ . The function is the probability distribution for heavy hadrons containing a fraction of the original quark energy,  $z = E_H/E_q$ . By varying  $\epsilon$  the shape of the function can be varied resulting in a change in the Monte Carlo electron momentum spectrum.

By varying the  $b$  and  $c$  semielectronic rates, the transverse momentum spectrum of the Monte Carlo electrons can be changed because of the mass difference of the  $b$  and the  $c$ . By varying the two branching ratios and the two fragmentation variables the Monte Carlo signal was fit to that of the data in the  $P - P_{\perp}$  plane using the method of maximum likelihood.

The final fit spectra are shown in figures 5.4 and 5.5 with the contributions of the various prompt electron sources. The fit gives:

$$B(c \rightarrow e) = 0.089 \pm 0.014$$

$$B(b \rightarrow e) = 0.150 \pm 0.029$$

$$\langle z_c \rangle = 0.68 \pm 0.06$$

$$\langle z_b \rangle = 0.77 \pm 0.05$$

The semielectronic rates are consistent with a model where non-spectator diagrams (figure 2.7) play a role in the  $b$  and  $c$  weak decays. The spectator model predicts:

$$B(c \rightarrow e) \approx 0.20$$

$$B(b \rightarrow e) \approx 0.14$$

The model including non-spectator diagrams would give:

$$B(c \rightarrow e) \approx 0.06 - 0.20$$

$$B(b \rightarrow e) \approx 0.11 - 0.15$$

The charm rate depends on the ratio of  $D^0$  to  $D^\pm$  produced since the non-spectator diagrams for these decays contribute differently to the electron rates. At PEP (29 Gev) the ratio is  $D^0/D^\pm \approx 7/8$  so that  $B(c \rightarrow e) \approx 0.08$  is expected.

The rates measured in this experiment agree well with the direct measurements of the  $b$  and  $c$  rates at the  $b\bar{b}$  and  $c\bar{c}$  resonance regions. No new sources of electrons were observed with momentum between 0.5 and 5.5 Gev/c. The final measured cross section for this momentum range is

$$\sigma(e^+e^- \rightarrow eX) = 35.8 \pm 3.1 \text{ pb}$$

The upper limit for new electron sources is 11.6 pb (90% CL) based on the calculated cross section expected with the semielectronic rates measured at the  $b\bar{b}$  and  $c\bar{c}$  resonances.

The heavy hadrons were seen to fragment with most of the energy of the original quarks. This agrees well with the earlier predictions of hard fragmentation

of heavy quarks by Bjorken where  $\langle z \rangle \approx 1 - 1/m_q$ . The fragmentation function suggested by Peterson et al. fits the data well; however, the fit is not very sensitive to the exact shape of the function, and other functions such as Field-Feynman fragmentation function also fit the data. The fragmentation measurements agree favorably with results of other prompt lepton experiments (table 5.8) and with experiments measuring  $D^*$  production (table 5.9).

By selecting events with electrons in restricted kinematical regions, purified samples of  $b\bar{b}$  and  $c\bar{c}$  events can be obtained (table 5.11). Events with electrons having  $P_{\perp} > 1 \text{ GeV}/c$  contain mostly  $b\bar{b}$  events with a signal to noise of about 6 to 1. This is an important technique which can be used to isolate  $b\bar{b}$  events for experiments designed to measure the  $b$  lifetime and properties of  $b$  quark jets.

The results of this experiment are not sensitive to the rate for  $B(b \rightarrow u)/B(b \rightarrow c)$  and we obtain

$$B(b \rightarrow c) = 0.85^{+0.77}_{-0.54}$$

so we must rely on the measurements from CESR for this result.

We observe 26 events with more than one electron candidate giving a total cross section for this process of

$$\sigma(e^+e^- \rightarrow 2eX) = 2.8 \pm 0.9 \pm 1.0 \text{ pb}$$

consistent with the rate expected from the previous analysis of the prompt electron  $P - P_{\perp}$  spectrum. The dielectron rate also shows no evidence for new electron sources. Most suggestions of new electron sources lead to enhanced multi-electron event production. For example charged Higgs production

$$e^+e^- \rightarrow H^+H^- \rightarrow c\bar{b} \quad \bar{c}b$$

can have up to 6 electrons in the final state and about 15% of these events would have 2 or more electrons.

The study of multi-electron events will enable experiments at PEP and PETRA to obtain important new measurements. Within another year there should be enough events to set limits on new electron sources. Limits on  $B^0\bar{B}^0$  mixing could be made by measuring the ratio of events having electrons of the same charge to those with electrons of opposite charge (table 5.13). The present data are consistent with no mixing, but one more year of data collection is needed to make a definite measurement.

APPENDIX A

# Electron Probability Tables

The following tables give the prompt electron probability rates. Contributions are given for  $b_{primary}$ ,  $b_{secondary}$ , and  $c_{primary}$  decay electrons. An entry in the table is the probability that an electron will be detected in a specific  $P - P_{\perp}$  bin if it comes from the decay of the heavy meson with a  $z$  value specified for that table. The primary hadrons are binned as shown in the following table.

**Binning for Primary Heavy Mesons.**

Source	$z_1$	$z_2$	$z_3$	$z_4$
$b$ mesons	0.35-0.50	0.50-0.65	0.65-0.80	0.80-1.00
$c$ mesons	0.10-0.30	0.30-0.55	0.55-0.80	0.80-1.00

$b \rightarrow e, .35 < z_b < .50$

Data Set	Momentum Gev/c	Transverse Momentum, (Gev/c)				
		.0	0.5	1.0	1.5	2.0
Iso	0.0	.0060				
	0.5	.0116	.0258			
	1.0	.0090	.0288	.0306		
	1.5	.0064	.0149	.0276	.0183	
	2.0	.0045	.0120	.0101	.0093	.0022
Nit	0.0	.0049				
	0.5	.0082	.0206			
	1.0	.0062	.0269	.0252		
	1.5	.0039	.0131	.0226	.0216	
	2.0	.0033	.0069	.0121	.0105	.0023
	2.5	.0020	.0046	.0033	.0029	.0007
	3.0	.0010	.0020	.0016	.0007	.0003
	3.5	.0007	.0016	.0007		.0003
	4.0	.0003	.0007			
	4.5				.0003	
5.0						

$b \rightarrow e, .50 < z_b < .65$

Data Set	Momentum Gev/c	Transverse Momentum, (Gev/c)				
		.0	0.5	1.0	1.5	2.0
Iso	0.0	.0047				
	0.5	.0117	.0271			
	1.0	.0051	.0149	.0159		
	1.5	.0019	.0112	.0168	.0070	
	2.0	.0033	.0089	.0145	.0112	.0014
Nit	0.0	.0029				
	0.5	.0084	.0252			
	1.0	.0034	.0109	.0160		
	1.5	.0025	.0109	.0172	.0067	
	2.0	.0038	.0088	.0093	.0067	.0008
	2.5	.0025	.0080	.0088	.0067	.0021
	3.0	.0017	.0042	.0042	.0025	
	3.5	.0008	.0059	.0055	.0025	.0008
	4.0	.0021	.0046	.0038	.0017	.0004
	4.5	.0013	.0008	.0017	.0004	
5.0	.0004	.0025	.0013	.0004		

$b \rightarrow e, .65 < z_b < .80$

Data Set	Momentum Gev/c	Transverse Momentum, (Gev/c)				
		.0	0.5	1.0	1.5	2.0
Iso	0.0	.0081				
	0.5	.0069	.0236			
	1.0	.0029	.0121	.0104		
	1.5	.0035	.0115	.0150	.0029	
	2.0	.0046	.0121	.0121	.0046	.0012
Nit	0.0	.0089				
	0.5	.0057	.0167			
	1.0	.0047	.0104	.0073		
	1.5	.0031	.0083	.0110	.0016	
	2.0	.0021	.0073	.0073	.0042	.0016
	2.5	.0037	.0047	.0063	.0052	
	3.0	.0016	.0042	.0042	.0057	.0005
	3.5	.0026	.0021	.0052	.0005	
	4.0	.0016	.0057	.0021	.0021	.0005
	4.5	.0016	.0078	.0016	.0005	.0010
5.0	.0021	.0021	.0026	.0026	.0005	

$b \rightarrow e, .80 < z_b < 1.00$

Data Set	Momentum Gev/c	Transverse Momentum, (Gev/c)				
		.0	0.5	1.0	1.5	2.0
Iso	0.0	.0078				
	0.5	.0042	.0174			
	1.0	.0018	.0162	.0078		
	1.5	.0012	.0090	.0102	.0012	
	2.0	.0030	.0072	.0078	.0042	
Nit	0.0	.0064				
	0.5	.0037	.0196			
	1.0	.0032	.0127	.0080		
	1.5	.0011	.0085	.0090	.0005	
	2.0	.0048	.0053	.0058	.0042	
	2.5	.0037	.0095	.0095	.0064	
	3.0	.0021	.0069	.0080	.0032	.0005
	3.5	.0027	.0058	.0058	.0005	.0005
	4.0	.0027	.0058	.0053	.0016	.0011
	4.5	.0021	.0053	.0037	.0021	.0005
5.0	.0011	.0037	.0032	.0016		

$b \rightarrow c \rightarrow e, .35 < z_b < .50$

Data Set	Momentum Gev/c	Transverse Momentum, (Gev/c)				
		.0	0.5	1.0	1.5	2.0
Iso	0.0	.0810				
	0.5	.0467	.0543			
	1.0	.0067	.0119	.0010		
	1.5	.0010	.0024	.0010	.0010	
	2.0		.0010			
Nit	0.0	.0634				
	0.5	.0417	.0413			
	1.0	.0039	.0087	.0035		
	1.5	.0009	.0030	.0009	.0004	
	2.0		.0009			
	2.5		.0004		.0004	
	3.0		.0004	.0009		
	3.5					
	4.0					
	4.5					
	5.0					

$b \rightarrow c \rightarrow e, .50 < z_b < .65$

Data Set	Momentum Gev/c	Transverse Momentum, (Gev/c)				
		.0	0.5	1.0	1.5	2.0
Iso	0.0	.0593				
	0.5	.0414	.0284			
	1.0	.0198	.0179	.0031		
	1.5	.0049	.0031	.0025	.0012	
	2.0	.0019	.0019	.0006	.0012	
Nit	0.0	.0414				
	0.5	.0338	.0245			
	1.0	.0125	.0169	.0016		
	1.5	.0076	.0049	.0016	.0005	
	2.0	.0033	.0033	.0005	.0011	
	2.5		.0005	.0005	.0005	
	3.0		.0011	.0005		.0011
	3.5					
	4.0		.0005			
	4.5					
	5.0					

$b \rightarrow c \rightarrow e, .65 < z_b < .80$

Data Set	Momentum Gev/c	Transverse Momentum, (Gev/c)				
		.0	0.5	1.0	1.5	2.0
Iso	0.0	.0398				
	0.5	.0398	.0191			
	1.0	.0191	.0168			
	1.5	.0123	.0069	.0046		
	2.0	.0031	.0061	.0015		
Nit	0.0	.0272				
	0.5	.0460	.0251			
	1.0	.0126	.0160			
	1.5	.0098	.0119	.0042		
	2.0	.0021	.0084	.0035	.0007	
	2.5	.0014	.0028		.0007	
	3.0	.0014		.0007		
	3.5			.0007		
	4.0					
	4.5		.0007			
	5.0					

$b \rightarrow c \rightarrow e, .80 < z_b < 1.00$

Data Set	Momentum Gev/c	Transverse Momentum, (Gev/c)				
		.0	0.5	1.0	1.5	2.0
Iso	0.0	.0243				
	0.5	.0405	.0146			
	1.0	.0211	.0178	.0008		
	1.5	.0122	.0097	.0008		
	2.0	.0105	.0081	.0024	.0008	
Nit	0.0	.0285				
	0.5	.0391	.0078			
	1.0	.0214	.0071			
	1.5	.0135	.0121			
	2.0	.0057	.0078	.0007		
	2.5	.0064	.0043			
	3.0	.0028	.0007	.0007		
	3.5		.0021	.0007		
	4.0	.0014	.0014	.0014		
	4.5			.0007		
	5.0		.0021			

$c \rightarrow e, .10 < z_c < .30$

Data Set	Momentum Gev/c	Transverse Momentum, (Gev/c)				
		.0	0.5	1.0	1.5	2.0
Iso	0.0	.0546				
	0.5	.0443	.0278			
	1.0	.0115	.0136	.0017		
	1.5	.0049	.0045	.0002	.0002	
	2.0	.0007	.0002	.0003	.0005	
Nit	0.0	.0491				
	0.5	.0378	.0273			
	1.0	.0143	.0116	.0008		
	1.5	.0047	.0025	.0003	.0003	
	2.0	.0014	.0008	.0003		.0003
	2.5	.0015	.0008	.0003		
	3.0	.0014	.0008	.0003		
	3.5	.0011	.0007	.0003		
	4.0	.0010	.0006	.0003		
	4.5	.0008	.0005	.0003		
5.0	.0007	.0005	.0003			

$c \rightarrow e, .30 < z_c < .55$

Data Set	Momentum Gev/c	Transverse Momentum, (Gev/c)				
		.0	0.5	1.0	1.5	2.0
Iso	0.0	.0206				
	0.5	.0400	.0066			
	1.0	.0165	.0101	.0009		
	1.5	.0106	.0108	.0019		
	2.0	.0054	.0057	.0021		.0003
Nit	0.0	.0204				
	0.5	.0327	.0068			
	1.0	.0181	.0080	.0005		
	1.5	.0116	.0063	.0018	.0008	
	2.0	.0050	.0083	.0015		.0005
	2.5	.0040	.0025	.0005		
	3.0	.0023	.0018	.0010	.0005	
	3.5	.0010	.0008			
	4.0	.0008	.0005	.0003		
	4.5	.0007	.0005	.0003		
5.0	.0007	.0005	.0003			

$c \rightarrow e, .55 < z_c < .80$

Data Set	Momentum Gev/c	Transverse Momentum, (Gev/c)				
		.0	0.5	1.0	1.5	2.0
Iso	0.0	.0192				
	0.5	.0212	.0009			
	1.0	.0190	.0050	.0004		
	1.5	.0105	.0044		.0002	
	2.0	.0098	.0061	.0011		.0002
Nit	0.0	.0150				
	0.5	.0205	.0010			
	1.0	.0171	.0031	.0007		
	1.5	.0157	.0065	.0003	.0003	
	2.0	.0113	.0099	.0003		
	2.5	.0075	.0055	.0010	.0003	
	3.0	.0034	.0048	.0014	.0003	
	3.5	.0031	.0017		.0007	
	4.0	.0010	.0044		.0003	
	4.5	.0038	.0024		.0003	
5.0	.0021	.0003	.0003			

$c \rightarrow e, .80 < z_c < 1.00$

Data Set	Momentum Gev/c	Transverse Momentum, (Gev/c)				
		.0	0.5	1.0	1.5	2.0
Iso	0.0	.0110				
	0.5	.0274				
	1.0	.0122	.0018			
	1.5	.0049	.0012			
	2.0	.0079	.0037			
Nit	0.0	.0103				
	0.5	.0234				
	1.0	.0140	.0009			
	1.5	.0122	.0028			
	2.0	.0103	.0047			
	2.5	.0112	.0028			
	3.0	.0094	.0009	.0009		.0009
	3.5	.0056	.0037			
	4.0	.0056	.0066			
	4.5	.0037	.0037	.0019		
5.0	.0037	.0009				

REFERENCES

1. J. J. Aubert et al., Phys. Rev. Lett. 33, 1404 (1974).
2. J.-E. Augustin et al., Phys. Rev. Lett. 33, 1406 (1974).
3. W. Braunschweig et al., Phys. Lett. 63B, 417 (1976).
4. G. Goldhaber et al., Phys. Rev. Lett. 37, 255 (1976); I. Peruzzi et al., Phys. Rev. Lett. 37, 569 (1976).
5. S. L. Glashow, J. Illiopoulos, and L. Maiani, Phys. Rev. D2, 1283 (1970).
6. M. Perl et al., Phys. Rev. Lett. 35, 1489 (1975).
7. S. W. Herb et al., Phys. Rev. Lett. 39, 252 (1977).
8. M. Kobayashi and K. Maskawa, Prog. Theor. Phys. 49, 652 (1973).
9. C. Berger et al., Phys. Lett. 76B, 243 (1978); C. W. Darden et al., Phys. Lett. 76B, 246 (1978) and 76B, 364 (1978); J. Beinlein et al., Phys. Lett. 78B, 360 (1978); D. Andrews et al., Phys. Rev. Lett. 44, 1108 (1980); T. Bohringer et al., Phys. Rev. Lett. 44, 1111 (1980).
10. D. Andrews et al., Phys. Rev. Lett. 45, 219 (1980); G. Finocchiaro et al., Phys. Rev. Lett. 45, 222 (1980).
11. C. Bebek et al., Phys. Rev. Lett. 46, 84 (1981); K. Chadwick et al., Phys. Rev. Lett. 46, 88 (1981);
12. L. J. Spencer et al., Phys. Rev. Lett. 47, 771 (1981).
13. G. Arnison et al., Phys. Lett. 122B, 103 (1983) and 126B, 398 (1983); M. Banner et al., Phys. Lett. 122B, 476 (1983).
14. R. Brandelik et al., Phys. Lett. 70B, 387 (1977).
15. J. M. Feller et al., Phys. Rev. Lett. 40, 1677 (1978).
16. W. Bacino et al. (DELCO), Phys. Rev. Lett. 43, 1073 (1979).
17. W. Bacino et al., Phys. Rev. Lett. 45, 329 (1980).
18. R. H. Schindler et al., Phys. Rev. D24, 78 (1981).
19. E. Fernandez et al., Phys. Rev. Lett. 51, 1022 (1983).
20. J. D. Bjorken, Phys. Rev. D17, 171 (1978); M. Suzuki, Phys. Lett. 71B, 139 (1977).
21. G. Wolf, Proceedings of the 21st International Conference on High Energy Physics, Journal de Physique, 43 C3-527 (1982).
22. R. D. Field and R. P. Feynman, Nucl. Phys. B136, 1 (1978); B. Anderson et al., Z. Phys. C1, 105 (1979); B. Anderson et al., Phys. Lett. B94, 211 (1980).
23. C. Peterson et al., Phys. Rev. D27, 105 (1983).

24. H. Abramovicz et al., Z. Phys. C15, 19 (1982).
25. N. Ushida et al., Phys. Rev. Lett. 45, 1049 (1980).
26. J. M. Yelton et al. (Mark II), Phys. Rev. Lett. 49, 430 (1982).
27. P. Avery et al. (CLEO), Phys. Rev. Lett. 51, 1139 (1983).
28. M. Altoff et al. (TASSO), Phys. Lett. 126B, 493 (1983).
29. S. Ahlen et al. (HRS), Phys. Rev. Lett. 51, 1147 (1983).
30. J. Kirkby, Proceedings of the 21st International Conference on High Energy Physics, Journal de Physique, 43 C3-45 (1982); W. B. Atwood et al. (DELCO), SLAC Preprint, SLAC-PUB-2980 (1982).
31. D. E. Koop et al. (DELCO), Phys. Rev. Lett. 52, 370 (1983).
32. M. E. Nelson et al. (Mark II), Phys. Rev. Lett. 50, 1542 (1983).
33. M. E. Nelson, Ph.D. Thesis, University of California at Berkeley (1983).
34. E. Fernandez et al. (MAC), Phys. Rev. Lett. 50, 2054 (1983).
35. B. Adeva et al. (Mark J), Phys. Rev. Lett. 51, 443 (1983).
36. M. Altoff et al. (TASSO), Desy Preprint, DESY 83-121 (1983).
37. C. Klopfenstein et al. (CUSB), Phys. Lett. 130B, 444 (1983).
38. K. Chadwick et al. (CLEO), Phys. Rev. D27, 475 (1983).
39. L. Maiani, Proceedings of the 21st International Conference on High Energy Physics, Journal de Physique, 43 C3-645 (1982).
40. G. Kalmus, Proceedings of the 21st International Conference on High Energy Physics, Journal de Physique, 43 C3-449 (1982).
41. H. Fritzsche and P. Minkowski, Phys. Lett. 90B, 455 (1980).
42. M. Bander, D. Silverman, and A. Soni, Phys. Rev. Lett. 44, 7 (1980); V. Barger, J. P. Leveille, and P. M. Stevenson, Phys. Rev. D22 (1980); H. Fritzsche and P. Minkowski, Phys. Lett. 90B, 455 (1980).
43. J. P. Leveille, Proceedings of the 17th Rencontre de Moriond, La Plagne, Savoie, France (1982).
44. W. Bacino et al., Phys. Rev. Lett. 70B, 387 (1977).
45. G. Gidal et al., Berkeley Particle Data Group, LBL-91, supplement UC-37 (1983).
46. G. Abshire et al., Nucl. Instr. Meth. 164, 67 (1979).
47. D. Muller, Phys. Rev., Vol 5, No 11, 2677 (1972).
48. W. E. Slater, Nucl. Instr. and Meth. 154, 233 (1978).
49. Acton Research Corporation, 525 Main Street, Acton, Mass. 01720, Vacuum UV mirror coating no.1600.

50. H. Hinterberger and R. Winston, *Rev. Sci. Instr.* **37**, 1094 (1966).
51. P. Baillon et al., *Nucl. Instr. Meth.* **126**, 13 (1975); E. L. Garwin et al., *Nucl. Instr. Meth.* **107**, 365 (1973).
52. J. Heintze et al., *Nucl. Instr. Meth.* **138**, 641 (1976).
53. E. L. Garwin et al., *Nucl. Instr. Meth.* **107**, 365 (1973); H. Okabe and D. A. Becker, *J. Chem. Phys.* **39**, 2549 (1963); E. L. Garwin, *Nucl. Instr. Meth.* **93**, 593 (1971).
54. J. V. Jelly, *Čerenkov Radiation and its Applications* (Pergamon Press, London, 1958); V. P. Zrelov, *Vavilov-Čerenkov Radiation and its Applications in High Energy Physics*, vol.2.(Atomisdat, Moscow, 1968).
55. F. A. Berends and R. Kleiss, *Nucl. Phys.* **B177**, 239 (1981).
56. D. Ouimette, D. Porat, A. Tilghman and C. C. Young, SLAC Preprint SLAC-PUB-2987 (1982), presented at the Nuclear Science Symposium, Washington, D. C. (1982).
57. B. Anderson, G. Gustafson, C. Peterson, *Z. Physik* **C1**, 105 (1979); B. Anderson, G. Gustafson, *Z. Physik* **C3**, 233 (1980); B. Anderson, G. Gustafson, T. Sjöstrand, *Z. Physik* **C6**, 235 (1980); *Phys. Lett.* **94B**, 211 (1980), *Nucl. Phys.* **B197**, 45 (1982).
58. T. Sjöstrand, Lund Preprints, LU TP 82-3, March 1982, and LU TP 82-7, June 1982.
59. S. Glashow, *Nucl. Phys.* **22**, 579 (1961); S. Wienberg, *Phys. Rev. Lett.* **19**, 1264 (1967); A. Salam, in *Elementary Particle Theory*, Proceedings of the Eighth Nobel Symposium, edited by N. Svartholm (Almqvist and Wiksells, Stockholm, 1968), p. 367.
60. W. Bartel et al., DESY Preprint 83-063 (1983); R. Brandelik et al., *Phys. Lett.* **117B**, 135 (1982); J. Dorfan, Invited talk presented at the International Symposium on Lepton and Photon Interactions at High Energy, Ithaca, New York (1983).
61. F. A. Berends and R. Kleiss, *Nuclear Physics* **B178**, 141 (1978).

62. G. B. Chadwick, Invited Talk at the Europhysics Study Conference on Electroweak Effects at High Energies, Erice, Italy, 1983, (SLAC-PUB-3118, May, 1983); W. Bartel, et al., Phys. Lett. 129B, 145 (1983).
63. N. Cabibbo and L. Maiani, Phys. Lett. 87B, 366 (1979).
64. Particle Data Group, *Review of Particle Properties*, LBL-100 Revised, UC-34d, April 1984.
65. F. James and M. Roos, Comp. Phys. Comm. 10, 343 (1975).
66. H. J. Behrend et al. (CELLO), Z. Phys. C19, 291 (1983).
67. M. K. Gaillard, B.W. Lee, and J. L. Rosner, Rev. Mod. Phys. 47, 277 (1975).
68. J. Ellis, M. K. Gaillard, D. V. Nanopoulos, and S. Rudaz, Nucl. Phys. B131, 285 (1977).